# ULTRASOUND BEAM SIMULATION FOR MAGNETIC RESONANCE-GUIDED FOCUSED ULTRASOUND SURGERY

by

Urvi Vyas

A dissertation submitted to the faculty of
The University of Utah
in partial fulfillment of the requirements for the degree of

Doctor of Philosophy

Department of Bioengineering

The University of Utah

December 2011

**STATEMENT OF DISSERTATION APPROVAL**

The dissertation of **Urvi Vyas**

has been approved by the following supervisory committee members:

| | | |
|---|---|---|
| **Douglas A. Christensen** | , Chair | **8/19/2011** Date Approved |
| **Robert B. Roemer** | , Member | **8/30/2011** Date Approved |
| **Dennis L. Parker** | , Member | **8/19/2011** Date Approved |
| **Elena Cherkeav** | , Member | **8/30/2011** Date Approved |
| **Natalya Rapoport** | , Member | **8/30/2011** Date Approved |

and by **Patrick Tresco** , Chair of

the Department of **Bioengineering**

and by Charles A. Wight, Dean of The Graduate School.

## ABSTRACT

Magnetic resonance-guided focused ultrasound surgery (MRgFUS) is a noninvasive means of causing selective tissue necrosis using high-power ultrasound and MR temperature imaging. Inhomogeneities in the medium of propagation can cause significant distortion of the ultrasound beam, resulting in changes in focal-zone amplitude, location and shape. Current ultrasound beam simulation techniques are either only applicable to homogeneous media or are relatively slow in calculating power deposition patterns in inhomogeneous media. Further, these techniques use table-value estimates of the acoustic parameters for predicting ultrasound beam propagation in inhomogeneous media, resulting in at best an approximate power deposition pattern. This work improves numerical analysis of ultrasound beam propagation by developing techniques for: 1) fast, accurate predictions of ultrasound beam propagation in inhomogeneous media, 2) noninvasive estimation of acoustic parameters (speed of sound and attenuation coefficient) of tissue types present in inhomogeneous media, 3) noninvasive determination of changes in tissue acoustic properties due to treatment. These beam simulation techniques utilizing subject-specific tissue parameters will rapidly predict power deposition patterns in real patient geometries and estimate changes in tissue acoustic parameters during treatment, leading to treatment-responsive patient-specific treatment plans that will improve the safety, efficacy and effectiveness of MRgFUS.

To Munnu, Anant, and Gautam

CONTENTS

LIST OF TABLES

Table

LIST OF FIGURES

Figure

# LIST OF ABBREVIATIONS

| | |
|---|---|
| 3D | Three Dimensional |
| AS | Angular Spectrum |
| EPI | Echo Planar Imaging |
| ERFA | Element Response Function Array |
| FDTD | Finite-Difference Time-Domain |
| FFT | Fast Fourier Transform |
| HAS | Hybrid Angular Spectrum |
| HIFU | High Intensity Focused Ultrasound |
| IFFT | Inverse Fast Fourier Transform |
| KZK | Khokhlov–Zabolotskaya–Kuznetsov |
| MRgFUS | Magnetic Resonance-guided Focused Ultrasound Surgery |
| MRgHIFU | Magnetic Resonance-guided High Intensity Focused Ultrasound |
| MRI | Magnetic Resonance Imaging |
| MRTI | Magnetic Resonance Temperature Imaging |
| PRF | Proton Resonance Frequency |
| R-B | Ring-Bessel |
| R-S | Rayleigh-Sommerfeld |
| SAR | Specific Absorption Rate |
| SNR | Signal-to-Noise Ratio |

| | |
|---|---|
| TE | Echo Time |
| TR | Repetition Time |
| WBU | Whole Breast Ultrasound |

# ACKNOWLEDGMENTS

It is a great pleasure to thank everyone who made this work possible. My advisor, Dr. Douglas Christensen gave me enthusiastic and unwavering support throughout this work and was a superb mentor. The path to a PhD is long, confusing and daunting, but Dr. Christensen made it achievable and even fun for me. I must also thank Drs. Dennis Parker and Robert Roemer for their support, numerous technical discussions and advice. I would like to thank all the research associates and graduate students at the high intensity focused ultrasound group for their support, both technical and nontechnical. Finally, I would like to thank my parents for being more proud of me than they should be. This work was supported by NIH 1R01 CA134599 and the Ben B. and Iris M. Margolis Foundation.

# CHAPTER 1

# INTRODUCTION

Magnetic resonance-guided focused ultrasound surgery (MRgFUS) is a noninvasive means of causing selective tissue necrosis using an ultrasound transducer run at high power together with MR temperature monitoring. Using a transducer with a large aperture and focusing the beam to a small volume causes tissue ablation at the region of interest while sparing the surrounding normal tissue. MRgFUS has applications in the brain [1] uterine fibroids [2], breast [3], [4], liver [5], and prostate [6]. Reflection, refraction and absorption of the ultrasound beam due to inhomogeneities in the medium of propagation can cause significant aberrations in the location and spatial extent of the beam's focus and may result in power deposition in undesirable and unsafe regions [7-11]. Current numerical techniques for ultrasound beam simulation are either only applicable to homogeneous media [12], or are relatively slow in calculating beam propagation in inhomogeneous media [13]. The accuracy of beam propagation techniques depends largely on the accuracy of the acoustic parameters specified in the tissue model. Published tissue speeds of sound and attenuation coefficient values vary significantly [14], with a three-fold variation in reported values of ultrasound absorption coefficient of

liver at 1 MHz [15]. Beyond the innate inhomogeneities of tissue, it has been shown that attenuation coefficient values of tissue increase significantly (two-fold or more) and irreversibly at high temperatures, common in MRgFUS treatments [16-18]. The goal of this project is to develop advanced numerical techniques for modeling ultrasound beam propagation in complex inhomogeneous tissue geometries utilizing subject-specific tissue acoustic properties that will improve the safety, efficacy and effectiveness of MRgFUS. To achieve this goal, this work will focus of developing techniques for: 1) accurate and fast prediction of beam propagation in complex inhomogeneous media, 2) noninvasive estimation of subject-specific tissue acoustic properties, and 3) noninvasive measurement of changes in tissue attenuation coefficient with MRgFUS treatment.

### 1.1. Beam simulation techniques for MRgFUS

The Rayleigh-Sommerfeld diffraction integral [19], [20], used extensively to model wave propagation in homogeneous media, calculates the pressure pattern at an output plane by calculating the effect of each point on the source plane on each point on the output plane. The number of calculations required for accurate results makes this is a relatively slow technique. For fast calculation of pressure patterns from rectangular [21], circular [22], triangular and irregular multisided polygon shaped sources [23], extensions of the Rayleigh-Sommerfeld technique have been developed. Although these methods result in fast calculation of the pressure patterns from specific shapes of transducers, they still assume that the medium of propagation is homogeneous, non-dissipative, and isotropic. Methods that convolve the spatial impulse response of the source and the source velocity function [24] are fast when calculating the transient pressure pattern at a

point. However, these techniques result in long computation times when used for calculating pressure pattern on a plane, since a separate calculation of the impulse response equation is required for each point in space (each point on-axis and off-axis has a unique impulse response). Although powerful, this method is restricted to cases where the impulse response can be easily calculated and is not tailored to calculate the pressure pattern at a plane or a volume [25].

The angular spectrum (AS) [26-28] method has been used for fast prediction of wave propagation in homogeneous media for MRgFUS. It uses the fast Fourier transform (FFT) algorithm to translate from the space domain to the spatial-frequency domain and propagates the waves in the spatial-frequency domain. The numerical implementation and parameter selection for the AS method have been discussed extensively in the literature [26], [29-31] and the method has been shown to be fast and accurate for homogeneous tissue.

The angular spectrum method and the Rayleigh-Sommerfeld technique have both been modified and extended to calculate pressure patterns in simple inhomogeneous models with layered media (layers of different homogeneous tissue) [32-34]. For inhomogeneous media with complex geometries similar to those found in the human body, the Khokhlov–Zabolotskaya–Kuznetsov (KZK) equation and the finite-difference time-domain techniques (FDTD) have been used. Marching scheme approaches [35], [36] using the KZK equation to evaluate the effects of diffraction, absorption and nonlinearity in successive steps have been developed; these methods are slow, with a full wave 3D calculation having a calculation time of the order of weeks. The FDTD technique has been used to model ultrasound beam propagation in inhomogeneous media [37], [38];

although a powerful technique, the limits placed on voxel sizes and difficult boundary conditions make this a slow technique.

#### 1.1.1. Current limitations

1) Traditional techniques (like the Rayleigh-Sommerfeld and the angular spectrum technique) can only model beam propagation in homogenous isotropic media, or layers of homogeneous media. The complex inhomogeneous geometries of the human body cannot be modeled using these techniques. 2) Although the KZK and FDTD techniques can be applied to calculate beam propagation in complex inhomogeneous tissue geometries, the limits placed on voxel sizes and difficult boundary conditions make these techniques computationally intensive and lead to long calculation times.

### 1.2. Need for subject-specific acoustic tissue parameters in MRgFUS

The latest compilation of tissue acoustic properties [14] cautions readers about the large variations in reported data due to different measurement techniques, tissue types and tissue preparations used by different investigators, and also tissue diversity due to age, abnormality and normal biological variation from subject-to-subject. Only 11% of the experiments reported in review [39] were *in-vivo*, and some values for tissue properties were reported using only one sample. Tissue ultrasound properties for clinically significant tissue types like pancreas, prostate and placenta were missing, while those for fat, breast, uterus and heart were not adequately investigated. Animal formalin-fixed tissue samples with significantly different ultrasound properties than fresh tissues

[15] and with invasive thermocouples that cause errors due to viscous heating at the interface of the medium and the thermocouple [40-42] were frequently used.

### 1.2.1. Current limitations

1) Tissue acoustic property data available are sparse, use invasive temperature measurement techniques, use *ex-vivo* tissue samples extensively, and are at best an estimate of the average tissue acoustic properties. 2) A noninvasive technique that accurately measures tissue acoustic properties *in-vivo* is not currently available.

## 1.3. Changing tissue acoustic properties with treatment in MRgFUS

The power density deposited at the beam's focus depends on the value of the tissue absorption coefficient, with absorption being a large component of the tissue's attenuation property. Several published studies [17], [43] have shown that attenuation coefficient values in tissue change significantly and irreversibly at the high temperatures that are common in MRgFUS, with a reported 1.8-fold increase in attenuation coefficient values at exposure of 70℃ [16], [44]. Changes in attenuation values reported in *ex-vivo* bovine liver [18], canine liver [45], and porcine kidney [46] have all shown similar increases (two-fold or more increase in attenuation coefficients) with high temperature. These irreversible changes in attenuation coefficient values are dependent on a complex set of treatment parameters: tissue type, heating time and maximum temperature achieved. There has been much interest in quantifying these relationships, with different investigators treating tissues to different temperatures or for different times [47], [48], [44] and measuring the resulting changes in attenuation. Due to the lack of a noninvasive

technique to measure attenuation change *in-vivo*, most studies have used the through-transmission substitution technique to measure tissue attenuation values before and after heating. The through-transmission technique can only be used to measure the average attenuation coefficient over the thickness of the tissue and hence most studies have used thin strips of *ex-vivo* tissue. Additionally, the presence of a transmitting and receiving transducer on either side of the tissue sample is required for these measurements, and hence they cannot be made noninvasively during treatment.

### 1.3.1. Current limitations

1) All studies rely on invasive thermocouple measurements or through-transmission substitution measurements to measure the changes in attenuation coefficient with treatment. 2) Dynamic changes during treatment (without removing the sample from the MRgFUS setup) cannot be measured using any technique.

## 1.4. Overview of this work

The work presented in this dissertation is aimed at addressing many of the limitations listed above. In particular, Chapter 2 describes a new technique called the hybrid angular spectrum (HAS) method for calculating pressure (and power deposition) patterns in complex inhomogeneous tissue geometries. It is an extension of the traditional angular spectrum method, and is a plane-by-plane propagation technique that utilizes the pressure pattern from the spherically curved transducer as specified on an intermediate plane before propagating further. Chapters 3 and 4 describe two techniques for calculating the pressure pattern from a curved transducer surface on an intermediate plane

in the homogenous propagating medium that usually occupies the region between the transducer and the treated object (e.g., water). Chapter 3 describes a technique for fast calculation of beam patterns at the intermediate plane using a Rayleigh-Sommerfeld-based precalculation technique (called the element response function array technique, or ERFA). Chapter 4 describes an extension of the angular spectrum method to curved surfaces for calculation of pressure patterns at an intermediate plane without requiring any precalculation. Using the intermediate pressure patterns from either of these techniques, the HAS method results in rapid (~2 s) prediction of ultrasound power deposition patterns inside inhomogeneous tissue models (1-mm isotropic resolution) in the tissue volume of interest (10x10x10 $cm^3$) typical for MRgFUS treatment.

Chapter 5 combines these rapid numerical beam propagation techniques with thermal simulations to compare the effect of frequently used treatment paths, transducer geometries and steering protocols on prefocal heating in MRgFUS treatments. Chapter 6 uses the fast beam simulation techniques in an optimization routine to estimate tissue acoustic properties noninvasively and uses this inverse parameter estimation technique to estimate changes in tissue attenuation with MRgFUS treatment in *in-vivo* rabbit thigh.

# CHAPTER 2

# ULTRASOUND BASICS

Ultrasound waves are acoustic waves above the frequency 20 kHz. The general principles of a wave travelling through a medium are shown in Figure 1. The wave propagates in a medium due to cyclical motion (compression and rarefaction) of the particles of the medium. The wavelength ($\lambda$) of the acoustic waves is related to the frequency of operation $f$ of the transducer,

$$\lambda = \frac{c}{f}, \tag{1}$$

where $c$ is the speed of sound of the wave in the medium. The higher the frequency of operation of the transducer, the smaller is the wavelength of the wave in the medium. In magnetic resonance-guided focused ultrasound surgery (MRgFUS), a high intensity focused ultrasound beam is used to selectively necrose tissue. The focused nature of the beam allows for absorption of the beam preferentially at the focal zone, while the tissue surrounding it remains relatively unaffected. A large range of frequencies is used for different clinical applications in MRgFUS, from low frequencies around 500 kHz for

brain applications to high-frequency transducers around 5 MHz for head and neck tumors.

In beam simulation studies intended for treatment planning for MRgFUS, only compressional waves are considered (particle motion in the direction of wave propagation) since shear waves attenuate rapidly in the body. The one-dimensional acoustic wave equation (in the $z$ direction) for pressure $p$ can be derived by using the Newton's law of motion and the conservation of mass principle as

$$\frac{\partial^2 p}{\partial z^2} - \rho_0 K \frac{\partial^2 p}{\partial t^2} = 0, \tag{2}$$

where $\rho_0$ is the average density and $K$ is the adiabatic compressibility of the material. All functions of the general form $p = p_{\mp} f(wt \pm kz)$, with $w = 2\pi f$ and $k = 2\pi/\lambda$, which satisfy the dispersion relationship $k^2 = \rho_0 K w$ are valid solutions of the wave equation.

The material properties of a medium, the compressibility and density, can be used to derive the acoustic properties of the medium. The speed of sound of an acoustic wave can be calculated using the relationship

$$c = \frac{1}{\sqrt{\rho_0 K}}. \tag{3}$$

The relationship between particle velocity $u$ and pressure $p$, called the acoustic impedance, is denoted by $Z$ and is

$$Z = \frac{p}{u} = \sqrt{\frac{\rho_0}{K}}. \tag{4}$$

The variation in acoustic properties encountered as the acoustic wave travels the body results in reflection, refraction and attenuation of the wave, as is described next.

These effects can lead to changes in the location and shape of the beam's focus and may result in undesirable heating at critical locations in the body.

## 2.1. Reflection and refraction

When an acoustic wave travels through the boundary between two regions with different acoustic impedances, a part of the wave striking the boundary gets reflected and some part gets transmitted (the refracted wave). Snells law (similar to optics) governs the angle of transmission, as shown in Figure 2.

$$\frac{\sin\theta_i}{\sin\theta_t} = \frac{\lambda_1}{\lambda_2} = \frac{c_1}{c_2}. \tag{5}$$

The ratio of the reflected pressure and the incident pressure is given by the reflection ratio $R$,

$$R = \frac{p_r}{p_t} = \frac{\left(Z_2 \big/ \cos\theta_t\right) - \left(Z_1 \big/ \cos\theta_i\right)}{\left(Z_2 \big/ \cos\theta_t\right) + \left(Z_1 \big/ \cos\theta_i\right)} \tag{6}$$

For normal incidence (frequently used to estimate power loss due to reflection) this equation reduces to

$$R = \frac{Z_2 - Z_1}{Z_2 + Z_1}. \tag{7}$$

## 2.2. Attenuation

As the acoustic wave travels in the body, power loss takes place due to two main mechanisms- scattering and absorption. Scattering includes reflections due to impedance mismatch at various interfaces and also partial beam redirection due to small impedance

variations in homogenous tissue regions. The majority of power loss as the wave travels in a medium is due to absorption of the wave. This absorption results in a temperature rise that can cause ablation in MRgFUS. The absorption coefficient $\alpha$ of the medium is frequency dependent, as follows:

$$\alpha = \alpha_0 f^b, \tag{8}$$

where $\alpha_0$ is the absorption coefficient at 1 MHz, $f$ is the frequency of operation of the transducer, and $b$ is the coefficient of frequency dependence of attenuation, which is 1 for most biological tissues. The mechanism resulting in absorption of ultrasound waves in a medium is related to its viscosity. Muscle has more absorbance than fat, and water has negligible absorption. As the wave travels in a medium, the particles in the medium oscillate around the center position; due to the viscosity of the medium, some of the wave's energy is lost to overcome the viscous drag due to the surrounding medium. Since the absorbance of a tissue depends on viscosity, the absorbance of muscle along the fibers and perpendicular to the fibers is different.

Quantifying scattering loss is difficult due to the fact that scattering results in a distribution of the wave in all directions and requires measurements in all directions. Therefore the attenuation coefficient, which includes effects of both absorption and scattering, is reported for most tissues. For biological media (except lung), scattering comprises about 20% of the attenuation coefficient. Since only the absorption coefficient of tissue results in temperature increase, separating the scattering coefficient from the absorption coefficient is very important for MRgFUS.

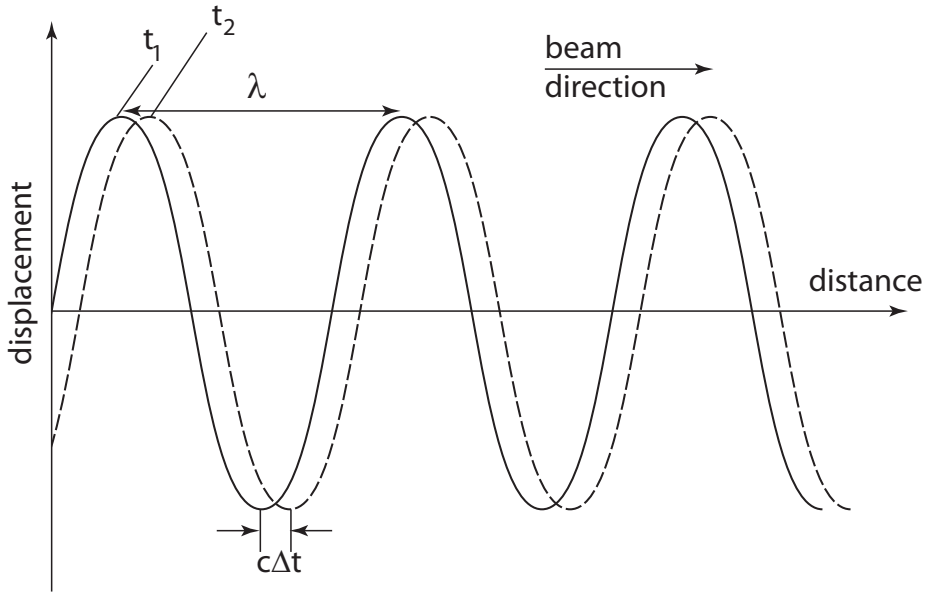


Figure 1. Schematic of a one-dimensional sinusoidal wave traveling through a medium at two instances of time, $t_1$ and $t_2$ ($\Delta t=t_2-t_1$), with wavelength $\lambda$ and speed of sound $c$.

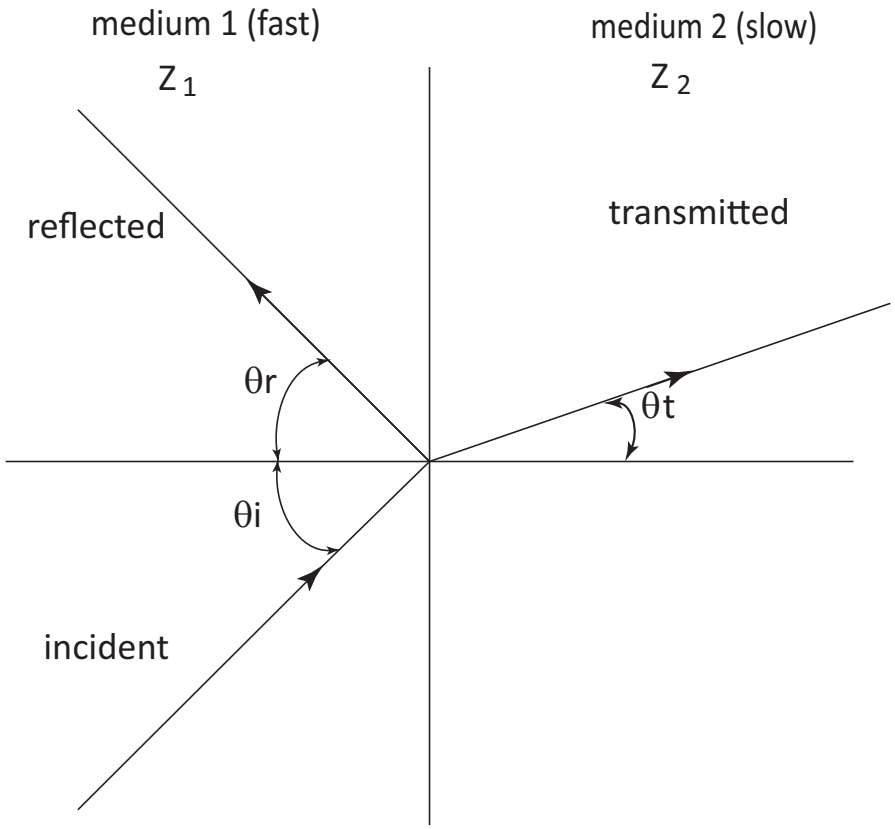


Figure 2. The angles of incidence, reflection and transmission as a wave strikes a boundary with an acoustic speed of sound mismatch. In this example, medium 2 has a slower speed of sound than medium 1, thus $\theta_t$ is less than $\theta_i$.

# CHAPTER 3

# ULTRASOUND BEAM SIMULATIONS IN INHOMOGENEOUS TISSUE GEOMETRIES USING THE HYBRID ANGULAR SPECTRUM METHOD

## 3.1. Introduction

Magnetic resonance-guided focused ultrasound surgery (MRgFUS) has received a great deal of attention in recent years because of its noninvasive nature, localized tissue effects and temperature feedback. For safe, effective and efficient treatment, controlling the energy deposited by the ultrasound beam is imperative. Refraction, reflection and particularly absorption of the ultrasound beam in inhomogeneous tissue geometries of the human body determine the specific power deposition pattern. Fast and accurate prediction of this pattern will help in control and guidance of the MRgFUS treatment.

Ultrasound beam simulation has been previously investigated using the Rayleigh-Sommerfeld integral [19]. This approach divides the source into points and finds the acoustic field from each point source at each point in the output plane, making this a flexible but relatively slow technique for calculating pressure fields from any type

of transducer geometry. Specializations of the Rayleigh-Sommerfeld method to calculate pressure fields from rectangular [21], circular [22], triangular and irregular multisided polygon shaped sources [23], have been proposed. Although these methods make it easier to calculate pressure fields from specific shapes of transducers, they still assume homogeneous, nondissipative and isotropic medium. The Rayleigh-Sommerfeld method has also been extended to calculate pressure fields through layered media (composed of homogeneous layers, each layer with different properties) .

Convolution methods that use convolution of the spatial impulse response of the source and the piston velocity function have also been employed [24]. The impulse response scheme requires that the source impulse response be separable, which is only possible for limited cases [20].

The Khokhlov–Zabolotskaya–Kuznetsov (KZK) equation can model nonlinear wave propagation, diffraction and absorption. The absorption term in the KZK equation is proportional to the square of frequency, which is often not appropriate for biological tissues that usually have a linear dependence on frequency [49], [50]. Also parabolic approximations in the KZK equation assume that the wave is very close to a plane wave, which is not strictly applicable for focused beams and for wave propagation in an inhomogeneous medium [20], [49], [51]. Marching-scheme approaches [36], [52], [53] using the KZK equation to evaluate the effects of diffraction, absorption and nonlinearity in successive steps have been developed; these methods are relatively slow and can be used only for the same cases for which the parabolic approximation is valid. In another approach, a parabolic wave equation can be derived from the Helmholtz wave equation using infinitesimal (linear) approximations, leading to a parabolic marching method [54].

The finite-difference time-domain (FDTD) approach that uses numerical approximations of the spatial and temporal partial derivatives about each node of a grid has been implemented to model wave propagation in inhomogeneous media [38]. Although a powerful technique, limits on the maximum size of the voxels and time steps that can be used lead to long computation times.

The Fourier split-step technique is used for modeling wave propagation in underwater acoustics [55] and seismic migration [56]. The technique calculates the effect of a varying velocity in the medium by alternating back and forth between the frequency-wavenumber and frequency-space domains. The average value of velocity is calculated in the frequency-wavenumber domain and the difference from average is calculated in the frequency-space domain. The technique handles slowly changing values of velocity without taking into account changes due to attenuation.

To increase the speed of beam simulations, the angular spectrum method has been used extensively [26], [27], [57]. This approach assumes linear propagation and steady-state conditions. The numerical implementation and parameter selection for the angular spectrum method have been discussed in the literature [58], [26], [29], [57], [59] and the method has been shown to be fast and accurate for homogeneous tissue. The method has also been extended to model wave propagation in layers of homogeneous media [32], [33].

The hybrid angular spectrum (HAS) technique [60] presented here can model inhomogeneous tissue properties, including varying attenuation, and the irregular geometries of the human body. It is an extension of the traditional angular spectrum

method to account not only for layers of homogenous tissue but also within-layer differences in tissue properties.

### 3.2. Traditional angular spectrum method

Figure 3 shows the traditional angular spectrum method, which assumes that the tissue between the initial and final pressure planes has homogeneous acoustic properties. Using the fast Fourier transform (FFT) algorithm, the pressure pattern on the initial plane $p'(x,y,0)$ is encoded into a spectrum $A'(\alpha/\lambda, \beta/\lambda; 0)$ of traveling plane waves in the spatial-frequency domain [22]. These waves travel at different angles that depend on their spatial frequencies $f_x$ and $f_y$ according to direction cosines $\alpha = \lambda f_x$ and $\beta = \lambda f_y$. Propagation of the waves is then calculated in the spatial-frequency domain by multiplying the initial spectrum by a propagation transfer function

$$e^{j\frac{2\pi}{\lambda}\sqrt{1-\alpha^2-\beta^2}\,\Delta z} \tag{9}$$

to account for the longitudinal path length $\Delta z$ between the two planes. An inverse fast Fourier transform (IFFT) of the angular spectrum of the propagated wave gives the pressure pattern $p(x,y,\Delta z)$ at the final plane in the space domain. The use of FFT and IFFT makes this technique very fast.

### 3.3. Hybrid angular spectrum (HAS) method

In the hybrid angular spectrum method, the 3D inhomogeneous tissue geometry is segmented into rectangular voxels, each voxel having its own speed of sound, absorption coefficient and density, as shown in Figure 4a. The pressure pattern in the

model is calculated sequentially, plane-by-plane, using transverse planes of voxels progressing in the direction of propagation away from the transducer. Within each plane of voxels, the acoustic properties are allowed to change in the *x*- and *y*-directions; within each voxel the properties are considered constant. The calculation sequence alternates back-and-forth between the space domain and the spatial-frequency domain for each plane of voxels. Pressure is therefore calculated in two steps within each plane, one in the space domain and one in the spatial-frequency domain, as described shortly.

The transmission of one of the plane-wave components (in the angular spectrum) of the pressure pattern through plane $n$ can be described in the space domain by the transmission function

$$t_n(x, y) = e^{jb_n(x,y)r' - a_n(x,y)r}, \tag{10}$$

where the first term in the exponent represents phase change and the second term represents attenuation as functions of $x$ and $y$. Here $b_n(x,y)$ is the propagation constant at various voxel locations (found from the specific speed of sound $c(x,y)$ and temporal frequency $f$ as $2\pi f/c$), $a_n(x,y)$ is the attenuation constant of the various voxels, $r'$ is the perpendicular distance between parallel wave fronts of the tilted plane wave, and $r$ is the oblique distance across the plane at the angle of the plane wave, as shown in Figure 4b.

To facilitate the two-step process, the phase change across the plane of voxels is divided into two parts, the average phase shift $b'_n r'$ calculated for that plane, and the difference $\Delta b_n(x,y)r'$ from the average phase shift for the various voxels inside the plane. Thus the transmission function becomes

$$t_n(x, y) = e^{j(b'_n + \Delta b_n(x,y))r'} e^{-a_n(x,y)r}$$

$$= e^{jb'_n r'} e^{j\Delta b_n(x,y) r'} e^{-a_n(x,y) r}. \quad (11)$$

In determining the $x$-$y$-averaged propagation constant $b'_n$, the averaging is weighted according to the magnitude of the pressure spatial pattern (that is, weighted according to where the beam is estimated to be).

Then the two-step process proceeds as follows: propagation changes due to the term $e^{j\Delta b_n(x,y) r'} e^{-a_n(x,y) r}$ are calculated in the space domain, while changes due to term $e^{jb'_n r'}$ are calculated in the spatial-frequency domain. This may be best visualized conceptually by considering the $x$-$y$-varying portions of the plane's voxels (i.e., the phase shift difference and attenuation) to be collapsed into a thin layer at the front of each plane (still maintaining the values of $r$ and $r'$) through which the pressure pattern is transmitted in the space domain, after which the pattern is propagated to the next plane in the spatial-frequency domain. This concept is illustrated in Figure 4b.

In the space domain step, if $p_{n-1}(x,y)$ is the pressure at the entrance to plane $n$, then the pressure $p'_n(x,y)$ after passing through the thin layer in the space domain is

$$p'_n(x,y) = p_{n-1}(x,y) e^{j\Delta b_n(x,y) r'} e^{-a_n(x,y) r}. \quad (12)$$

As shown in Figure 4b, $r$ and $r'$ will vary depending on the angles of the various plane-wave components of the angular spectrum. In order to account for this variation, the values of $r$ and $r'$, which are constants in Eqn. (12) for a given plane, are calculated with a weighting factor based on the magnitude of the angular spectrum at this plane.

In the spatial-frequency domain step, the resulting pressure pattern $p'_n(x,y)$ is then Fourier transformed to obtain the angular spectrum $A'_n(\alpha/\lambda, \beta/\lambda; z)$ for propagation across the plane:

$$A'_n(\frac{\alpha}{\lambda},\frac{\beta}{\lambda};z) = \Im\{p'_n(x,y)\}. \tag{13}$$

Propagation is accomplished in the spatial-frequency domain using the propagation transfer function incorporating the average propagation constant $b'_n$:

$$A_n(\frac{\alpha}{\lambda},\frac{\beta}{\lambda};z+\Delta z) = A'_n(\frac{\alpha}{\lambda},\frac{\beta}{\lambda};z)e^{jb'_n\sqrt{1-\alpha^2-\beta^2}\Delta z}, \tag{14}$$

where $r'$ has been replaced with an equivalent geometric expression involving direction cosines $\alpha$ and $\beta$, effectively implementing the propagation transfer function of Eqn. (9).

The pressure $p_n(x,y)$ at the entrance to the next plane of voxels in the space domain is found from an inverse Fourier transform:

$$p_n(x,y) = \Im^{-1}\{A_n(\frac{\alpha}{\lambda},\frac{\beta}{\lambda};z+\Delta z)\}. \tag{15}$$

This sequence is repeated for each subsequent plane of voxels to obtain the forward propagating pressure pattern in the 3D model.

First-order reflections in the model are calculated in the space domain using the reflection coefficient at each interface Eqn. (7) (found from the acoustic impedances of the respective voxel pairs at the interface [61]), then propagating the reflected wave in the backward direction using the same back-and-forth approach between the space domain and the spatial-frequency domain. At each interface, the backward propagating pressure pattern composed of reflections from deeper interfaces is added to the reflection from that interface. Finally the forward and the backward propagating waves are added together in complex notation to give the final pressure pattern for the 3D inhomogeneous model.

## 3.4. Implementation details

The effects of sampling in the space domain and the spatial-frequency domain in the traditional angular spectrum method have been described previously [62], [63]. Because of the use of the FFT and IFFT algorithms in the HAS technique, the sampling interval and extent of the spatial-frequency domain are linked to the sampling interval and extent of the space domain.

### 3.4.1. Size of voxels

The size of the voxels in the space domain ($\Delta x$ and $\Delta y$) sets the overall size of the spatial-frequency domain, for example, $F_{xmax} = 1/\Delta x$, a consequence of the FFT algorithm. The maximum size of the voxels in the space domain, therefore, is limited by the highest spatial-frequency content of the beam's features. To eliminate aliasing due to under-sampling in the space domain, the sampling frequency in the space domain should be at least as high as the Nyquist criterion ($1/\Delta x \geq$ twice the highest desired frequency). The highest spatial-frequency components of the angular spectrum can be restricted using ray theory truncation [26] or angular restriction techniques [30]. (Frequencies higher than $1/\lambda$ are effectively non-propagating since they are evanescent.) Smaller voxels result in longer calculation times but produce smoother beam patterns. Smaller voxels also reduce the stair-stepping effect at oblique interfaces that results from segmenting the model into rectangular voxels. For our application, which uses the beam simulation software to guide MRgFUS, the size of the voxels is normally set equal to the resolution of the MRI temperature images, usually on the order of 1-mm isotropic resolution.

3.4.2. Size of the space domain

The overall extent of the space domain (*Lx* and *Ly*) is at least as large as the model itself, but may need to be increased due to consideration of wraparound errors, a consequence of using too large a sampling interval $\Delta fx$ in the frequency domain. Wraparound errors, which are due to under-sampling in the frequency domain as explained in the Discussion section, can be eliminated by increasing the overall size of the space domain by zero padding, since $\Delta fx = 1/Lx$.

3.4.3. Number of voxels

The number of voxels in the model is set by the size of the voxels ($\Delta x$ and $\Delta y$) and the overall size of the space domain ($L_x$ and $L_y$). The larger the numberof voxels the longer the calculation times (for e.g., computation times for model of size 201x201x201 is 15 s while that for a model of size 101x101x101 is 5 s). In order to avoid the half-sample phase-shift error [32] the number of the voxels in the model in the x- and y-directions should be kept odd.

3.4.4. Pressure on the initial plane

One of the requirements for both the angular spectrum method and the HAS technique is that the initial pressure pattern must be specified on a plane. When using curved transducers with either technique, a separate beam simulation method is required to calculate the pressure pattern from the curved transducer surface to the initial plane of the inhomogeneous model. A homogeneous beam propagation technique, such as the Rayleigh-Sommerfeld integral, can be used to calculate this initial pressure since the

space between the transducer and the front plane of the model in almost all simulations is comprised of water (or a similar homogeneous coupling liquid).

To keep the overall calculation time of our simulation short we have developed a faster method to calculate the initial pressure field from a curved phased-array transducer using precalculated Rayleigh-Sommerfeld patterns, called the element response function array (ERFA) technique [28]. The response of each element of the phased array (normalized by assuming zero phase and unit amplitude) is precalculated and stored as one page in the ERFA. During run time, each page is multiplied by the appropriate element phase and amplitude (to account for electronic steering and an arbitrary excitation pattern) and all pages are summed in complex notation (a fast calculation) to get the resulting pressure pattern at the initial plane of the inhomogeneous model. This reduces the run-time calculation time by three orders of magnitude compared to a full Rayleigh-Sommerfeld calculation at run time.

### 3.5. Results

To illustrate the technique in a clinically relevant situation, we chose an inhomogeneous model constructed from a segmented MRI image of a patient with breast cancer. The model was segmented by hand into three tissue types: breast fat, fibro-glandular tissue and breast cancer. The ultrasound properties for these tissue types were set using values from [14], [61], given in Table 1. A 256-element, 1-MHz, spherically curved, 14.5-cm outer diameter phased-array transducer with its geometric focus at 13 cm was assumed for this model. The transducer was located 11 cm away from the initial plane of the breast model, which was divided into 85x85x45 voxels with 1.5-mm

isotropic resolution. The pressure pattern on the initial plane was calculated using the ERFA method, described above. First-order reflections were included for all results. All numerical simulations were done on a 2-GB Windows laptop using MATLAB version 7.8.

Longitudinal slices of the pressure calculated by the HAS method through the beam's focal center are given in Figure 5a shows the magnitude of the pressure calculated at the geometric focal zone of the transducer with no electronic steering. Figure 5b shows the magnitude of the calculated pressure pattern through the focus when the phased-array transducer is electronically steered 10 mm away from the geometric focus in both the *y* and *z* directions. Figure 5c shows the calculated pressure pattern through the center of the focal zone when the phased-array transducer is electronically steered 15 mm away from the geometric focus in all three directions. The 3D calculation time for each of these cases was approximately 5 s.

For validation, the HAS technique was additionally compared to an FDTD simulation [15] using a finer three-medium inhomogeneous 3D model purposely configured to exhibit reflection, refraction and absorption. The validation model contained 141x141x121 voxels with 0.15-mm isotropic resolution, as shown in Figure 6, with the acoustic properties given in Table 2. Both techniques assumed a single-element, 1.5-MHz transducer with an outer diameter of 10 cm and a geometric focus of 18 cm. The initial model plane was located 17 cm away from the transducer; the pressure at the initial plane was calculated using the Rayleigh-Sommerfeld integral.

Longitudinal slices through the center of focus of the magnitude of the calculated pressure using the HAS and FDTD methods are shown in Figures 7a and 7b respectively.

(The FDTD pressure pattern was actually calculated for a model 25% longer in the direction of propagation than shown in Figure 7b, then truncated in order to avoid displaying reflections from the far boundary of the model, which did not employ radiating boundary conditions; the HAS technique inherently incorporates effective radiating boundary conditions at the far model boundary.) There was a significant difference in the calculation times for each method: the HAS technique took 9.5 s for the full 3D simulation, while the FDTD technique took 67 minutes.

In order to quantify the comparison between the two methods, the normalized-root-mean-square (nrms) difference between the two pressure patterns was calculated according to

$$\Delta_{nrms} = \sqrt{\frac{\sum_{i=1}^{n} (p_{HAS}(i) - p_{FDTD}(i))^2}{n}}, \tag{16}$$

where $p_{HAS}(i)$ and $p_{FDTD}(i)$ are the normalized pressures calculated using the HAS technique and the FDTD technique respectively, at each voxel $i$ in the calculated 3D volume of $n$ voxels. Each beam pattern was normalized to the highest pressure found in the 3D volume (i.e., at the beam focus). The root-mean-square error for the results shown in Figure 7 was found to be $\Delta_{nrms} = 0.013$.

### 3.6. Discussion

The traditional angular spectrum technique and hence the HAS approach are both plane-to-plane propagation techniques; a prerequisite for these methods is that the initial pressure pattern be calculated on the model's first plane using a homogeneous beam

propagation technique, such as the Rayleigh-Sommerfeld integral or the ERFA precalculation technique (discussed in Chapter 4) used in this paper, to account for propagation from the curved transducer to the first plane. The ERFA method has proven to be fast and can handle changing electronic beam-steering conditions at run time.

The HAS technique does not require the user to explicitly set any boundary conditions, but the implicit boundary conditions for the model are: 1) a radiating boundary at the model's back face normal to the axis of propagation, since no reflections are implemented there; and 2) totally reflecting boundaries at the model's edges parallel to the axis of propagation, a consequence of spatial wraparound. Wraparound can be explained as follows: Due to the discrete frequency domain sampling employed in the HAS technique, (for example at intervals $\Delta f_x$ in the $f_x$-direction), the effective space domain pattern can be regarded as an infinitely large patchwork made up of repeating source planes at repeat distances equal to, in this example, $L_x = 1/\Delta f_x$ in the $x$-direction. As the plane waves of the angular spectrum propagate at various angles deeper into the model, high-angle (high-frequency) waves from adjacent source planes can enter the propagating space of the central volume. This results in wraparound in the space domain as the waves propagate deeper into the model, and is equivalent to total reflecting boundary conditions at the model edges parallel to the axis of propagation.

Figure 5 shows that the HAS technique is able to calculate pressure patterns for an inhomogeneous 3D model by accounting for refraction, absorption, reflection and electronic steering of the ultrasound beam. It correctly predicts the location of the steered focus, and simulates details such as grating lobe clutter and power drop-off when the

phased-array transducer is electronically steered away from the geometric focus, as seen in Figures 5b and 5c.

Figure 7 displays the similarity between the pressure patterns calculated using the HAS and the FDTD techniques for the model of Figure 6. Because of the impedance mismatch at the wedge-water interface, reflections and a partial standing wave pattern can be seen in front of the oblique wedge interface in both the patterns. The angle of beam refraction due to the tilted wedge-water interface is essentially equal for both techniques. A high-pressure region can be seen just beyond the wedge in both patterns, due mainly to focusing of the beam, but attenuation by the highly absorbing cylinder significantly reduces the intensity in the beam propagating through and past the cylinder. The two techniques yielded effectively the same pressure patterns: the nrms difference in the magnitudes of the normalized pressures was only 1.3% over the entire 3D patterns.

## 3.7. Conclusions

The HAS technique calculates the complex pressure pattern in an inhomogeneous 3D model assuming steady state and linear propagation conditions. The technique is rapid, resulting in a decrease in calculation time of more than two orders of magnitude compared to the FDTD technique, while giving essentially the same pressure pattern.

Table 1. Ultrasound tissue properties used in breast model

| | speed of sound m/s | absorption Np/(cm•MHz) | density $kg/m^3$ |
|---|---|---|---|
| water | 1500 | 0 | 1000 |
| breast cancer | 1560 | 0.133 | 1064 |
| fibro-glandular tissue | 1480 | 0.091 | 937 |
| breast fat | 1480 | 0.086 | 937 |

Table 2. Ultrasound tissue properties used in validation model

| | speed of sound m/s | absorption Np/(cm•MHz) | density $kg/m^3$ |
|---|---|---|---|
| wedge | 2000 | 0 | 600 |
| cylinder | 1500 | 2.0 | 1000 |
| water | 1500 | 0 | 1000 |

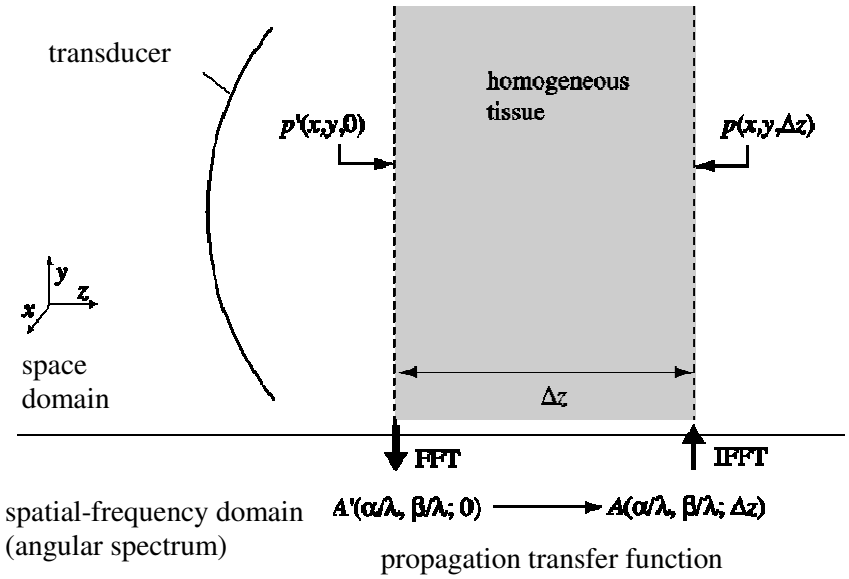


Figure 3. Traditional angular spectrum method with the angular spectrum expressed in terms of direction cosines $\alpha = \lambda f_x$ and $\beta = \lambda f_y$, where $f_x$ and $f_y$ are spatial frequencies.

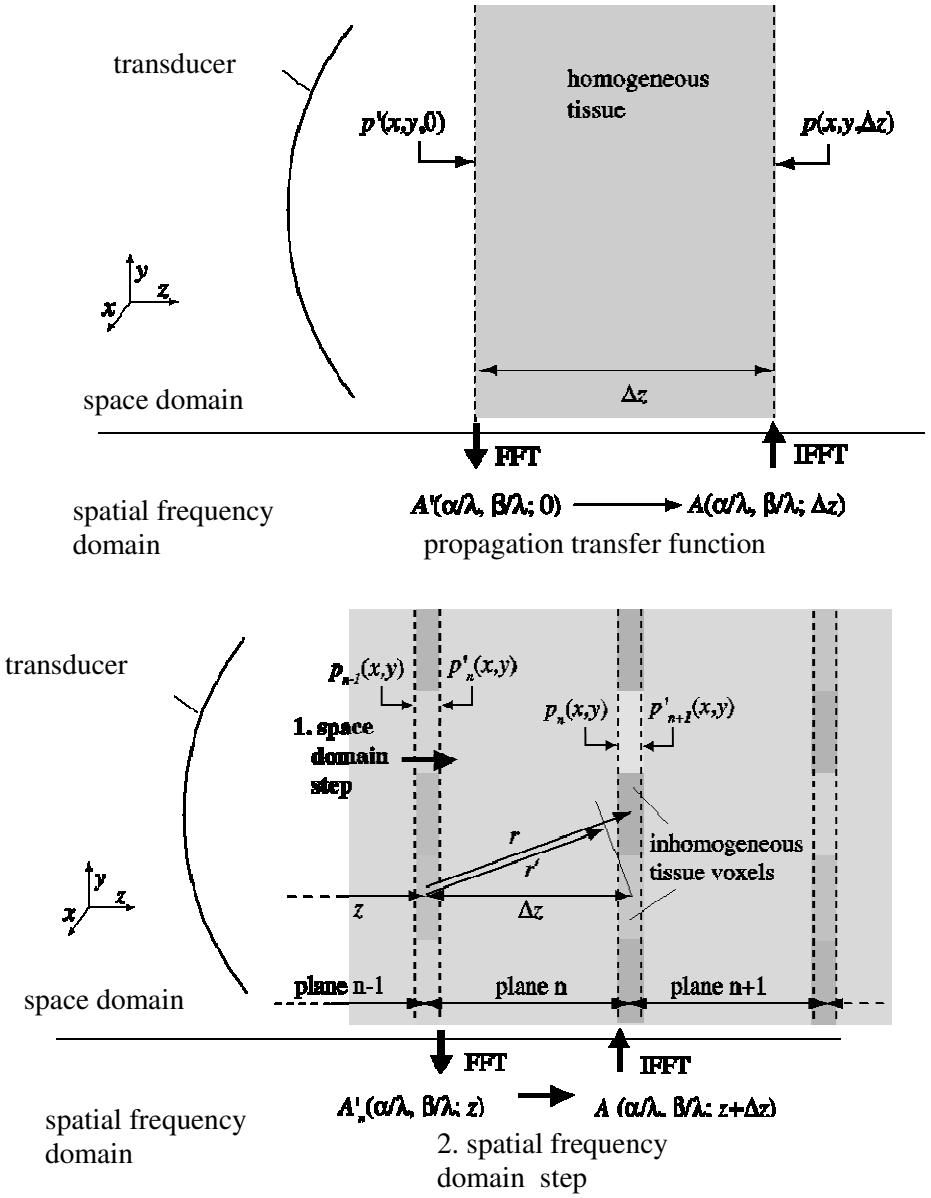


Figure 4. Hybrid angular spectrum method a) The inhomogeneous model is divided into rectangular voxels and calculations are done plane-by-plane in the propagation direction, first in the space domain then in the spatial-frequency domain; r and r' are usually tilted out-of-plane. b) To help conceptualize the two-step process at each plane, the variations in the voxels' acoustic properties from the planar average are collapsed into a thin layer through which the beam first travels in the space domain, then is propagated to the next plane by an average transfer function in the frequency domain.

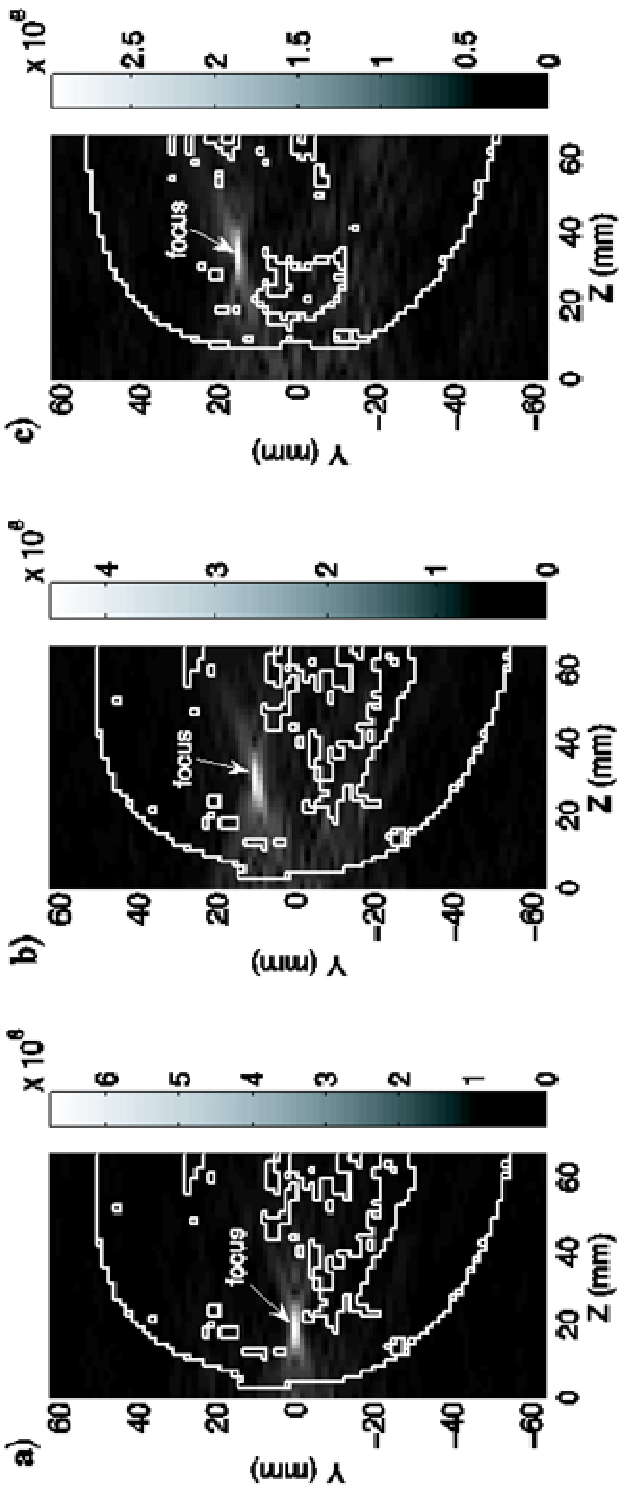


Figure 5. Longitudinal slices of the magnitude (in Pa) of the calculated pressure pattern in the breast model a) through the geometric focus of an unsteered beam, b) through the focus of a beam electronically steered 10 mm away from the geometric focus in the transverse (y) and longitudinal (z) directions, and c) through the focus when electronically steered 15 mm in all directions. The transducer radiates 100 acoustic watts and is located 11 cm to the left of each figure.

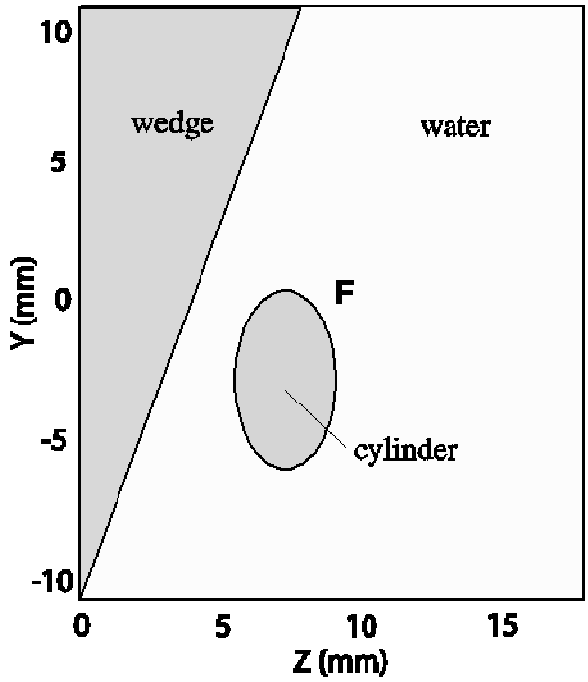


Figure 6. Longitudinal slice of the 3D model used for comparing the results of the HAS technique with the FDTD technique. The acoustic properties of the three features are given in Table II. The model has 141x141x121 voxels with 0.15 mm isotropic resolution. The solid transducer is located 17 cm to the left of the figure with its focus located at F.

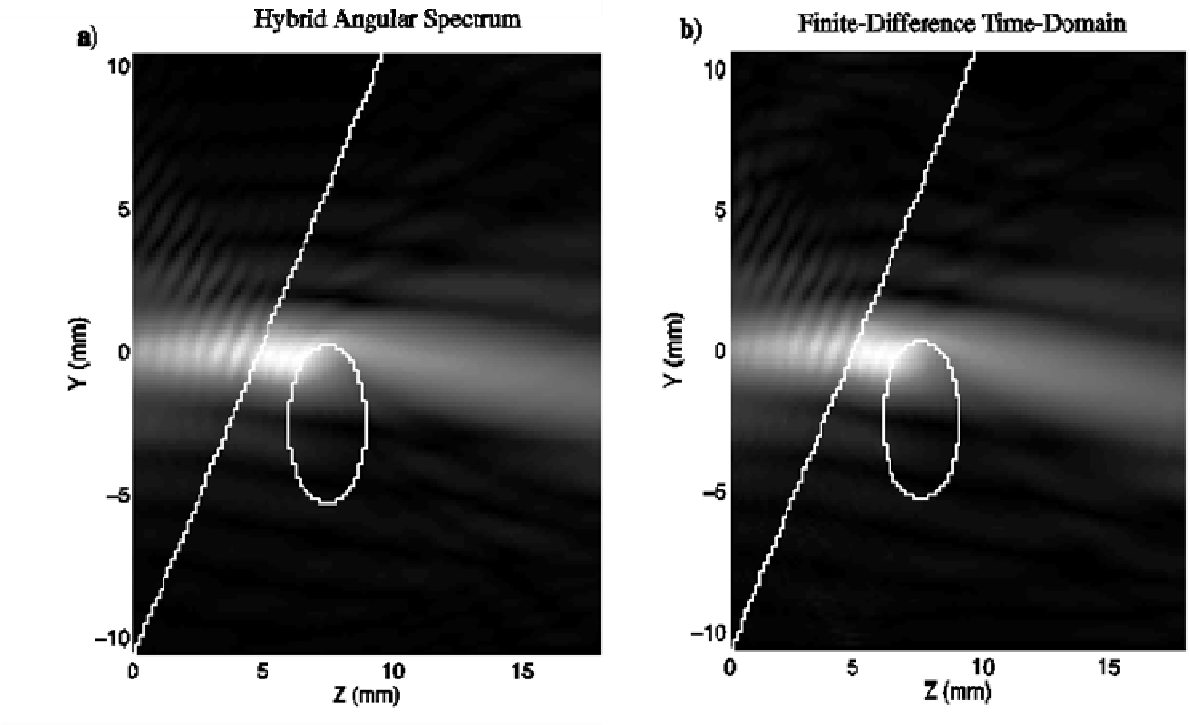


Figure 7. Longitudinal slices of the magnitude of the pressure pattern through the focus of the model shown in Figure 6, using a) the hybrid angular spectrum method, and b) the finite-difference time-domain method. Both patterns are normalized to the highest pressure calculated in each individual 3D volume.

# CHAPTER 4

# FAST BEAM SIMULATIONS FOR PHASED-ARRAY TRANSDUCERS USING A PRECALCULATION-BASED ELEMENT RESPONSE FUNCTION ARRAY (ERFA) TECHNIQUE

## 4.1. Introduction

Magnetic resonance-guided focused ultrasound surgery (MRgFUS) is a noninvasive means of causing selective tissue necrosis using an ultrasound transducer operated at high power in conjunction with MR temperature monitoring. MRgFUS has applications in the brain [64], uterine fibroids [2], breast [3], [4], liver [5], and prostate [6]. Numerical beam simulation techniques are used to predict the location, shape and size of the beam's focal zone for transducer design studies [65] and for optimization of patient treatment plans [35] where the focal zone is repeatedly positioned inside the pathologic tissue while minimizing treatment time and keeping normal tissue temperature within safe levels. The use of phased-array transducers with multiple elements, each capable of operating at a unique phase and amplitude, allows the focal zone of the transducer to be steered electronically and enhances the flexibility of MRgFUS treatments. In this technical note we present a new technique employing a precalculated

element response function array (ERFA) for faster run-time calculation of pressure patterns from phased-array transducers. The Rayleigh-Sommerfeld integral [19] is often used for beam simulations, and various techniques to speed up calculation times of this integral have divided the source into equally spaced arcs [66] or into rectangular elements [67] or have used the fast Fourier transform algorithm [57]. Here we demonstrate the ERFA technique, also based on the Rayleigh-Sommerfeld integral; however this concept can be easily applied to other numerical beam simulation methods used to model a phased-array transducer.

## 4.2. Theory

The Rayleigh-Sommerfeld integral giving the pressure pattern $p$ from a source is

$$p(r) = j\rho ck \int_S \frac{u(r')e^{-jk|r-r'|}}{2\pi|r-r'|} dS \tag{17}$$

where $\rho$ is the density, $c$ is the speed of sound and $k$ is the wavenumber in the medium between the transducer and the secondary ERFA plane (the plane where the pressure pattern is desired). $S$ is the area over the transducer aperture, $u(r')$ is the face velocity of the transducer and $|r-r'|$ is the distance between the coordinates of points $r'$ on the source plane and the points $r$ on the ERFA plane. In the traditional Rayleigh-Sommerfeld calculation, the integral in Eqn. (17) is calculated for each point $r'$ on the source plane and each point $r$ on the final plane; due to the large number of points required by the Nyquist criterion [68], the run-time calculation time is relatively long. In the ERFA technique, each element's response on the entire final plane is separately precalculated

and stored as a page in a 3D array. Thus, for element *n* of the phased-array transducer, the element response is calculated as

$$p_n(r) = j\rho ck \int_{S_n} \frac{u_n(r'_n)e^{-jk|r-r'_n|}}{2\pi|r-r'_n|}dS \tag{18}$$

where $S_n$ is the surface over element *n*, $r'_n$ denotes the coordinates of various points within the transducer element *n*, and *r* denotes the coordinates of a point on the ERFA plane. The pressure $p_n(r)$ is stored as page *n* of the ERFA array, as shown in Figure 8. During this precalculation each element is assumed to be driven at zero phase and unit amplitude. The resulting ERFA array has *N* pages for an *N*-element phased-array transducer. During run-time the phase and amplitude to be applied to each element for the desired focal location is calculated, each page is multiplied with its respective phase $e^{j\phi_n}$ and amplitude $A_n$, and the array is collapsed (all the pages added together) to get the complex pressure pattern on the secondary plane $p(r)$,

$$p(r) = \sum_{n=1}^{N} p_n(r) A_n e^{j\phi_n}. \tag{19}$$

Thus the ERFA technique reduces the run-time calculation of the pressure patterns for changing phased-array steering conditions to a matrix multiplication and a summation, significantly reducing run-time computation time.

## 4.3. Implementation details

The precalculation step for the ERFA technique is fixed for a set of ERFA parameters (transducer specifications, sampling interval on the source plane, and size and sampling interval on the secondary pressure plane); any change in these parameters

requires calculation of a new ERFA for the transducer. This section states some guidelines for efficient implementation of the ERFA technique that we have determined empirically.

The sampling interval on the source plane, or equivalently the number of sample points within each element, is set by the Nyquist criterion.

The dimensions of the secondary ERFA plane are determined by the extent of the region of interest of the beam pattern.

The smaller the size of the pixels in the ERFA plane, the better the spatial resolution; the larger the size of each ERFA page, the longer the precalculation time. The final pressure pattern calculated using the ERFA technique is on a transverse plane parallel to the transducer. For calculating pressure patterns in a 3D homogenous or inhomogeneous model, the transverse pressure plane can be propagated further using other techniques such as finite-difference time-domain or angular-spectrum method. Before using the ERFA-calculated pressure pattern in models with different pixel sizes, interpolation of the pressure pattern calculated by the ERFA technique may be needed. In order to reduce errors caused by interpolation, the size of the ERFA pixels should ideally be less than the smallest pixel size to be used in all models.

The pressure pattern on the ERFA plane is calculated at a fixed distance from the transducer. If this distance is changed, the angular spectrum method [13] can be used to forward or backward propagate the pressure pattern from the ERFA plane to the desired plane.

## 4.4. Results

The pressure pattern at a plane 8-cm away from a spherical 256-element 1-MHz phased-array transducer with its geometric focus at 13 cm was calculated using 1) the traditional calculation of the Rayleigh-Sommerfeld integral during run-time, and 2) the ERFA technique using a precalculated Rayleigh-Sommerfeld pages. Each approach used the same sampling intervals in the source and the secondary plane; the diameter of the transducer was 14.5 cm and the size of the secondary plane 11 cm x 11 cm, with either 101x101 points or 201x201 points in either surface as shown in Table 3. Since the pressure patterns were calculated using the same Rayleigh-Sommerfeld integral formula in the two techniques, no difference between the two patterns was expected or found. However, a significant difference was noticed in the run-time calculation times for the two techniques. Precalculation of the ERFA technique is required only once for a particular transducer and sampling interval in the source and final plane, and once computed can be used to repeatedly calculate pressure patterns on the secondary plane plane for various beam steering conditions. The run-time calculations were between 8 and 136 times faster than direct calculation of the Rayleigh-Sommerfeld integral. A higher reduction in computation time can be expected in an array with greater a number of elements.

## 4.5. Conclusions

A new technique to rapidly calculate the pressure pattern on a plane from a phased-array transducer is presented. The ERFA technique is a general technique and can

be used with any numerical beam simulation technique that can separately precalculate the pressure pattern from each element of a phased-array transducer.

Table 3. Computation time for the ERFA technique and the traditional Rayleigh-Sommerfeld technique

| Number of transducer elements | Points on source surface | Points on secondary plane | ERFA precalculation time (sec) | Run-time calculation using ERFA (sec) | Run-time calculation using traditional Rayleigh-Sommerfeld (sec) |
|---|---|---|---|---|---|
| 256 | 101x101 | 101x101 | 22 | 2 | 16.8 |
| 256 | 101x101 | 201x201 | 77 | 2 | 66 |
| 256 | 201x201 | 201x201 | 352 | 2 | 272 |

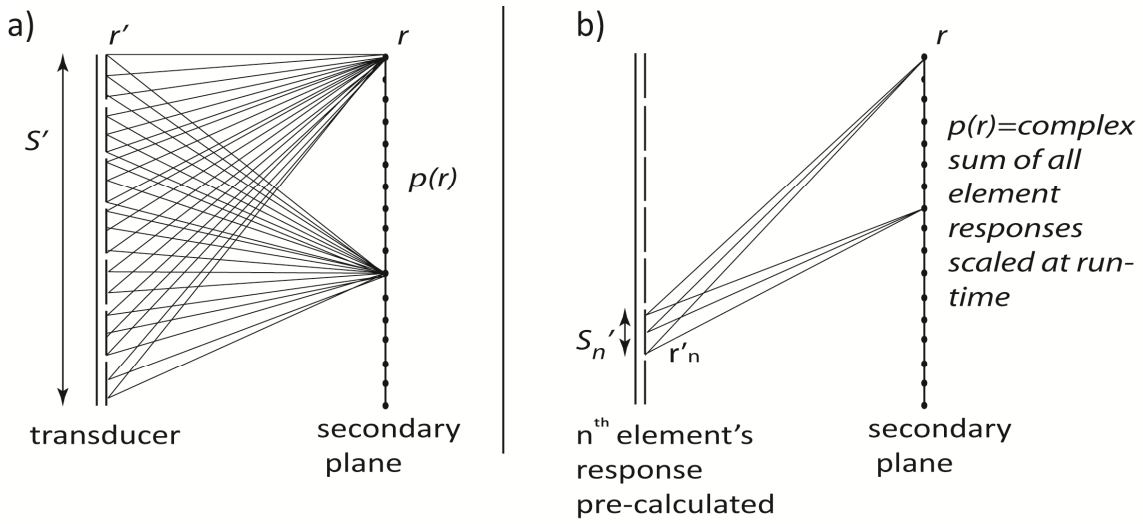


Figure 8.The steps of calculation required for a) the traditional Rayleigh-Sommerfeld integral, and, b) the element response function array technique.

# CHAPTER 5

# EXTENSION OF THE ANGULAR SPECTRUM METHOD TO CALCULATE PRESSURE FROM A SPHERICALLY CURVED ACOUSTIC SOURCE

## 5.1. Introduction

Magnetic resonance-guided focused ultrasound surgery (MRgFUS) is a technique for noninvasively producing selective tissue necrosis using a high-intensity focused ultrasound beam [64]. Numerical beam propagation techniques are needed to predict the location and spatial extent of the beam's focus to determine optimal treatment parameters for safe, efficient and accurate treatment. Since repeated simulations are required with different treatment parameters (transducer power, transducer locations, treatment paths, and electronic focusing of the transducer), it is highly desirable that the beam predictions be fast. In this paper we present a technique to rapidly calculate ultrasound beam propagation from a curved source to a given plane using purely frequency-domain concepts.

The angular spectrum (AS) method [27], [28] has been applied to a variety of problems for modeling wave propagation in the field of optics [28], electromagnetics [69] and acoustics [26]. The technique describes the spatial-frequency components of a

complex field distribution on a source plane in the form of plane waves travelling at different angles; the cosine of the angle of each plane wave is proportional to its spatial frequency. The field spectrum at a distant parallel plane is calculated by implementing wave propagation using a propagation transfer function (spectral propagator) in the spatial-frequency domain; the final field pattern is found from an inverse Fourier transform. In acoustics, the numerical implementation and parameter selection for the AS method has been discussed extensively [58], [26], [29], [60] and the method has been used for modeling wave propagation for MRgFUS applications in homogeneous tissue [12] as well as in layered [33] and inhomogeneous [60] media. The use of the 2D fast Fourier transform (FFT) makes this a fast technique and requires that the source field amplitude be specified on a plane [28]. In MRgFUS applications where curved transducers are extensively used, different techniques have been employed by authors to calculate the pressure pattern from the source to an intermediate plane before the angular spectrum method can be used with the FFT algorithm.

The Rayleigh-Sommerfeld integral [19] is a space-domain technique that is frequently used to calculate the pressure field from transducers of different geometries. Each point on the transducer is considered an elementary source and the contribution of each point source to the pressure at every point on the intermediate plane is calculated in the space domain. The large number of calculations required to calculate detailed pressure on a plane makes the implementation of this technique relatively slow.

The transient pressure pattern from a curved source can be obtained using the impulse response method [70], [71] such as employed in the Field II [23], [72] technique and the Fast Near Field method [73]. Each point in space (on-axis and off-axis) has a

unique impulse response and to calculate the pressure pattern on a plane, every point requires a separate calculation of the impulse response equation. The angular spectrum method, on the other hand, calculates the complex pressure pattern on the complete plane. The impulse response method is better suited to calculate the time-dependent pressure field at a point, whereas the angular spectrum method is better suited to calculate the steady-state complex pressure field on a plane [25].

Guyomar and Powers [74] studied the extension of the angular spectrum to curved transducers by dividing the curved surface into planar transducers, each having a time delay. The technique assumes x-y source separability and calculates the time delay using the thin lens approximation. In the case of phased arrays with different phases on each element, a time delay under these approximations is not easily calculated.

Wu and Stepinski [59] applied two approaches to extend the AS method to cylindrically curved radiators. The first approach uses numerical integration and does not employ the FFT technique. The second approach, called the indirect angular spectrum approach, calculates the pressure field on an intermediate plane in front of the curved source by dividing the source into planar rectangular sub-elements using the rectangular radiator approach [67] and then applies the AS method to propagate beyond this plane.

In this paper we extend the angular spectrum method by introducing a new Ring-Bessel technique that implements frequency-domain concepts directly from the curved source to an intermediate plane perpendicular to the propagation axis, from where the fields can then be propagated by conventional AS methods. Using a frequency-domain approach allows fast and efficient computer implementation with the FFT algorithm.

## 5.2. Approach

Consider a spherically curved solid source with radius of curvature $R_c$, where the furthest point on the source is at a distance $d$ from an intermediate plane, as shown in Figure 9. Using numerous planes parallel to the intermediate plane, the source is divided into a set of circular rings, where each ring has a small arc width $\Delta R$ that is the same for all rings. The ring width is small enough that the source surface within the ring can be considered to lie in a plane (parallel to the intermediate plane) that intercepts the center of each ring. For the $i^{th}$ ring this plane is at a distance $z_i$ from the intermediate plane. In this plane, the ring has an inner radius $r_i^-$ and an outer ring radius $r_i^+$, with the radius of the ring at its center being $R_i$, as shown in Figure 10. The Fourier transform in spatial-frequency polar coordinates $V_i(\rho,\phi)$ of the source velocity $v_i(r,\theta)$ within each ring is found according to a generalization of Eq. 2-29 in Goodman [28]:

$$V_i(\rho,\phi) = \int_0^{2\pi} \int_{r_i^-}^{r_i^+} v_i(r,\theta) e^{-j2\pi r\rho\cos(\theta-\phi)} r dr d\theta. \tag{20}$$

Since the width of each ring is small, the source velocity within each ring is approximately uniform as a function of r across the ring width and may therefore be represented by a function $v_i(\theta)$ of angle only and attributed to a radius $R$ at the center of the ring; Eqn. (20) then becomes

$$V_i(\rho,\phi) = R_i \Delta R \int_0^{2\pi} v_i(\theta) e^{-j2\pi R_i\rho\cos(\theta-\phi)} d\theta. \tag{21}$$

Here $v_i(\theta)$ denotes the complex normal velocity of points on the ring and hence is a periodic (circular) function with a period of 2π. $v_i(\theta)$ can be expressed as a 1D Fourier series:

$$v_i(\theta) = \frac{1}{2\pi} \sum_{n=-\infty}^{n=\infty} C_{n,i} e^{jn\theta}, \tag{22}$$

where

$$C_{n,i} = \int_0^{2\pi} v_i(\theta) e^{-jn\theta} d\theta. \tag{23}$$

Substituting Eqn. (22) into Eqn. (21),

$$V_i(\rho,\phi) = \frac{R_i \Delta R}{2\pi} \sum C_{n,i} \int_0^{2\pi} e^{-j2\pi R_i \rho \cos(\theta-\phi)} e^{jn\theta} d\theta. \tag{24}$$

Changing variables by letting $\eta = \theta - \phi$ and $d\theta = d\eta$ in the integral, Eqn. (24) becomes

$$V_i(\rho,\phi) = \frac{R_i \Delta R}{2\pi} \sum C_{n,i} \int_{-\phi}^{2\pi-\phi} e^{-j2\pi R_i \rho \cos(\eta)} e^{jn\eta} e^{jn\phi} d\eta. \tag{25}$$

Since terms inside the integral are periodic over 2π, the sign of the first exponential can be reversed and the limits changed to (0 to 2π), resulting in

$$V_i(\rho,\phi) = \frac{R_i \Delta R}{2\pi} \sum C_{n,i} e^{jn\phi} \int_0^{2\pi} e^{j2\pi R_i \rho \cos(\eta)} e^{jn\eta} d\eta. \tag{26}$$

Using one form of a Bessel identity (Eqn. 9.1.21 in Abramowitz and Stegun [75])

$$J_n(z) = \frac{1}{2\pi j^n} \int_0^{2\pi} e^{jz\cos(\eta)} e^{jn\eta} d\eta,$$

it can be easily seen that

$$\int_0^{2\pi} e^{j2\pi R_i \rho \cos(\eta)} e^{jn\eta} d\eta = 2\pi j^n J_n(2\pi R_i \rho), \tag{27}$$

so Eqn. (25) becomes

$$V_i(\rho,\phi) = R_i \Delta R \sum C_{n,i} e^{jn\phi} j^n J_n(2\pi R_i \rho). \tag{28}$$

Equation (28) is the angular spectrum of the $i^{th}$ ring at the plane of that ring. By multiplying the angular spectrum of each ring by the spectral propagator from its plane to the intermediate plane, summing the propagated angular spectra of all rings, then using the inverse Fourier transform (IFFT), the overall pressure pattern at the intermediate plane can be obtained. To propagate each ring's spectrum, the spectral propagator that converts from velocity to pressure given by

$$H(\rho, z_i) = \frac{\rho c e^{2\pi j z_i \sqrt{\frac{1}{\lambda^2} - \rho^2}}}{j2\pi \sqrt{\frac{1}{\lambda^2} - \rho^2}}, \tag{29}$$

is used, where $\rho c$ represents the acoustic impedance of the medium into which the waves are propagating.

## 5.3. Implementation details

This section states some guidelines for efficient implementation in MATLAB 7.7 of the Ring-Bessel technique that we have determined empirically.

### 5.3.1. Sampling the source surface in space

Figure 11 illustrates the two stages of sampling performed on the source surface. First, the source is divided into $N$ rings of equal arc widths by incrementing the angle subtended from the center of the sphere to the center of each successive ring. The angle increment is a constant $\delta q$, so the sampling interval along the arc is equal to $\Delta R = R_c \delta q$.

Second, each ring is discretized into $p_i$ number of points to account for the velocity variations with angle within each ring. In practice, a circumferential sampling distance $S_m$ is specified and $p_i$ is calculated using

$$p_i = \frac{2\pi R_i}{S_m}, \tag{30}$$

where $R_i$ is the radius of the ring. Since the technique uses the Fourier series to find coefficients for the frequency-domain representation [see Eqns. (23) and (28)], the number of sample points on each ring should be odd. Thus, the calculated $p_i$ is rounded to the nearest odd integer. Hence each ring may have a slightly different circumferential sampling interval, but this is accounted for with a normalizing step in the calculation algorithm.

In our practice we have found that the arc and the circumferential sampling intervals should be kept approximately equal to each other (set according to the Nyquist criterion) and should be no larger than the sample spacing on the intermediate plane for accurate results.

### 5.3.2. Size and sampling of the intermediate plane

The user establishes the size ($L_h$, $L_v$) and the number of samples ($N_h$, $N_v$) in the space domain for the intermediate plane in Cartesian coordinates to suit the particular problem being analyzed. Because the intermediate plane pressure in the space domain is calculated using the IFFT of the combined propagated angular spectra, the size and sampling intervals for the intermediate plane spatial-frequency content are in turn set by the size and intervals of the space variables. Therefore the intervals between spatial-frequency values are $\Delta F_x = 1/L_h$ and $\Delta F_y = 1/L_v$ and the total widths of the spectrum at the intermediate plane are $F_x = N_h/L_h$ and $F_y = N_v/L_v$.

5.3.3. Size and sampling of the frequency-domain spectra

Since the source in space is sampled into rings using polar coordinates, the combined Fourier series of all rings results in the spatial-frequency content also being described in polar coordinates. After propagation to the intermediate plane, the angular spectrum must be converted from polar coordinates to Cartesian coordinates to match the Cartesian coordinate system chosen for the intermediate plane. The equations $F'_x = \rho\cos(\varphi)$ and $F'_y = \rho\sin(\varphi)$ are used for this conversion. Interpolation is then used to find the angular spectrum on the regularly spaced Cartesian grid ($F_x$, $F_y$) set by the user (see previous section) from the nonuniform Cartesian grid ($F'_x$, $F'_y$). For higher accuracy of interpolation, the sampling interval of the spatial-frequency polar coordinate grid is kept approximately equal to that set by the user in the regularly spaced Cartesian coordinate grid.

The maximum overall useful radius of the spatial-frequency polar coordinate grid is given by $\lambda_{max}$. In order to avoid the singularity in the spectral propagator, $\lambda_{max} \neq$

$1/\lambda$. When $\lambda_{max}>1/\lambda$, the waves are evanescent and essentially do not propagate. We have found that for our application in calculating pressure patterns away from the near-field of the transducer, $\lambda_{max}$ is preferably set at a value very close to $1/\lambda$, e.g., $0.999(1/\lambda)$ and all higher spatial frequency components are set to zero. In applications where accuracy of the near-field pressure is required, either the pressure-to-pressure spectral propagator [58] can be implemented or the higher spatial frequencies can be modeled using a notch filter around the $\lambda_{max}=1/\lambda$ location.

For faster calculation times using MATLAB, we avoid explicit for loops (except for one incrementing through the rings), and arrange the matrix for calculating $J_n(2\pi R_i\rho)$ in Eqn. (28) such that the Bessel function order $n$ increases along each row while the argument $\rho$ increases along each column. We also use a custom nearest-neighbor interpolation function that takes advantage of the monotonic nature and regular spacing of the spatial-frequency polar coordinate grid.

### 5.3.4. Implementation of the Rayleigh-Sommerfeld and Field II techniques

The Rayleigh-Sommerfeld and the Field II techniques were both implemented in MATLAB 7.7. Since both techniques require repeated calculations at each point on the intermediate plane nested *for* loops were avoided whenever possible. Our implementation of the Rayleigh-Sommerfeld technique had only one explicit *for* loop (as did the Ring-Bessel technique for the solid transducer; in case of the phased-array transducer Ring-Bessel had two *for* loops). In the case of a solid transducer the Rayleigh-Sommerfeld technique sampled the source using the spherical coordinate system with angular increments for each point in the Cartesian grid. Since Field II requires a function call for

each field point, its implementation used two *for* loops; the source was defined as a rigid baffle and sampled into rectangles with sampling frequency set at 100 MHz. The numbers of sampling points on the source surface were equal for all three techniques (about ¼ of the wavelength).

## 5.4. Results

In order to validate the accuracy of the Ring-Bessel (R-B) technique, simulation results calculated by R-B were compared to those determined using the Rayleigh-Sommerfeld (R-S) integral and the Field II technique. The programs for all techniques were written in MATLAB 7.7 and implemented on a laptop computer with an Intel dual core 4-GHz processor. The times taken for each calculation to the intermediate plane and the normalized pressure distributions produced by all techniques were compared. Simulations in both a solid transducer and a steered phased-array transducer were used as examples. When beam simulations are used to support MRgFUS applications, it is important to obtain pressure distributions over the complete 3D volume in the region being treated. Therefore in the following examples, we calculated the 2D pressure pattern by each technique on a 7 cm x 7 cm intermediate plane located 8-cm away from the transducer surface, and then propagated the resulting waves through the volume containing the focus by the conventional AS method.

### 5.4.1. Solid transducer

A solid spherically curved 1-MHz transducer with an aperture size of 14.5 cm and its geometric focus at 13 cm was modeled using the three techniques. The sampling

distance at the aperture surface was at 0.04 cm (about ¼ of the wavelength), the same for all three implementations. After propagation from the intermediate plane, the 3D pressure distributions were found around the focal region with 0.5-cm spatial resolution in the transverse direction and 0.1-cm resolution in the axial direction. Figure 12a shows a comparison of the absolute value of the pressure along a line perpendicular to the direction of propagation through the geometric focus for each of the three techniques. Similarly, Figure 12b compares the absolute values along a line through the geometric focus in the direction of propagation. The calculation times for each of the three methods to produce the initial pressure patterns on the intermediate plane are given in Table 4. The time required for the AS propagation was the same for all methods, 3.5 s, and is not included.

### 5.4.2. Electronically steered phased-array transducer

To represent a class of transducers often used in MRgFUS applications, a 128-element spherically curved 1-MHz phased-array transducer was also modeled. The transducer has an outer diameter of 10 cm and a radius of curvature of 13 cm. Each element was circular and curved with a diameter of 0.22 cm; they were arranged in a random fashion (to reduce grating lobe sharpness) as shown in Figure 13. For the R-B calculations the transducer surface was sampled into 251 rings. The sampling spacing of source points within each ring was approximately 0.04 cm. In order to directly compare the two approaches, the same source points, arranged in concentric circles as used in the R-B simulation, were used for the R-S calculation, except that all points outside the

active elements were excluded from the R-S calculation since they did not contribute to the radiated pressure.

The elements of the phased array were phased such that the beam was focused 1-cm away from the geometric focal point in both the vertical and horizontal directions in the transverse plane (but not electronically steered in depth). Figure 14a shows a graphical image of the absolute pressure in an axial slice through the focus using the R-S method to obtain the pressure pattern on the intermediate plane. Figure 14b shows the same image using the R-B technique.

Table 4 gives the calculation times for each approach (again not including the AS propagation times).

## 5.5. Discussion

To compare the results obtained by the R-B method to those from the traditional methods, a mean difference value was calculated as follows:

$$\Delta mean = \frac{\sum_{i=1}^{n} \left| p_{RB}(i) - p_{ref}(i) \right|}{n}$$

where $p_{RB}(i)$ and $p_{Ref}(i)$ are the absolute pressures calculated by R-B method and by the method used for comparison, respectively, at each point $i$ in any given 2D plane. Each beam pattern is normalized to the highest pressure found in the 3D volume, which occurs at the respective focal locations.

The comparisons given in Figures 12a and 12b for the solid transducer show that the R-B approach produces a pressure distribution very similar to those from the R-S and Field II simulations; all three techniques predict essentially the same focal zone

location, width and length. Away from main focus, some differences in the plots can be seen, but the amplitude of the discrepancies is small. As listed in Table 4, the mean difference across the transverse plane through the focal point is 0.7 % for both the comparisons, while the mean difference in the longitudinal plane through the focus is 1.2% or less. There was a significant difference in calculation times, however, with the R-B method producing results a factor of 24 times faster than the R-S and 29 times faster than Field II. In an application where speed is a high priority and small errors are tolerable compared to other acoustic uncertainties, such as in MRgFUS planning and control, we believe the R-B method will prove very useful.

The comparisons for the electronically steered phased-array transducer shown in Figures 14a-d, exhibit slightly larger rms differences than for the solid transducer, likely due to the presence of grating lobe clutter around the focal zone. We have seen that the magnitude of the grating lobe clutter increases as the steered angle increases for a given phased array, and that the peak intensity at the focus decreases (not shown). The nature of the grating lobe features is sensitive the exact source and spatial-frequency sampling pattern, and this is probably why the mean differences are larger for the steered phased array, between 1.67 % and 1.50 %, as given in Table 4. The location and dimensions of the mean focus are very similar for the two simulations (Figures 14c and 14d) while some variation is seen in the regions away from the focus. It should be emphasized that the two techniques follow completely different strategies: the R-S method is a purely space-domain approach employing an integral over the source points using spatial coordinates, while the R-B technique is a purely frequency-domain technique that transforms the source points into the frequency domain for propagation using a transfer function before

an inverse Fourier transform produces the final space pattern. The use of the FFT and multiplicative transfer function results in quicker calculation times, about 11 times faster, as seen in Table 4.

Our implementation of the R-B method used the velocity-to-pressure spectral propagator (transfer function) given in Eqn. (29) since both R-S and Field II techniques assume a velocity source. However, a pressure-to-pressure propagator is easily implemented if it is more appropriate for a given application.

## 5.6. Conclusions

Although the examples of this paper used spherically curved transducers to demonstrate the R-B technique, it is not restricted to the calculation of pressure fields from spherical surfaces; it can be applied to any surface of rotation around the axis of propagation. However, there are some limitations to the technique. It assumes independent propagation of the angular spectrum from each ring to the intermediate plane; it does not account for any interference or secondary diffraction due to the presence of the other rings, hence can be used only for transducers with strictly increasing ring radius in the direction of propagation (similar to the R-S approach). It also is applicable only to linear wave propagation in the steady state. For transient analysis, an impulse response method such as Field II or the Fast Near Field method should be used.

For applications where rapid simulations of the 3D patterns from curved transducers are needed, such as in the planning and control of MRgFUS treatments, the Ring-Bessel method may prove to be an attractive alternative to the Rayleigh-Sommerfeld or Field II methods.

Table 4. Comparison of calculation times and mean differences

| Simulation method | Calculation time | Mean normalized difference from Ring-Bessel | |
|---|---|---|---|
| | | transverse plane through focus | longitudinal plane through focus |
| Solid transducer | | | |
| Ring-Bessel | 38 s | - | - |
| Rayleigh-Sommerfeld | 924 s | 1.07 % | 0.70 % |
| Field II | 1091 s | 1.19 % | 0.74 % |
| Phased-array transducer (steered) | | | |
| Ring-Bessel | 45 s | - | - |
| Rayleigh-Sommerfeld | 493 s | 1.67 % | 1.50 % |

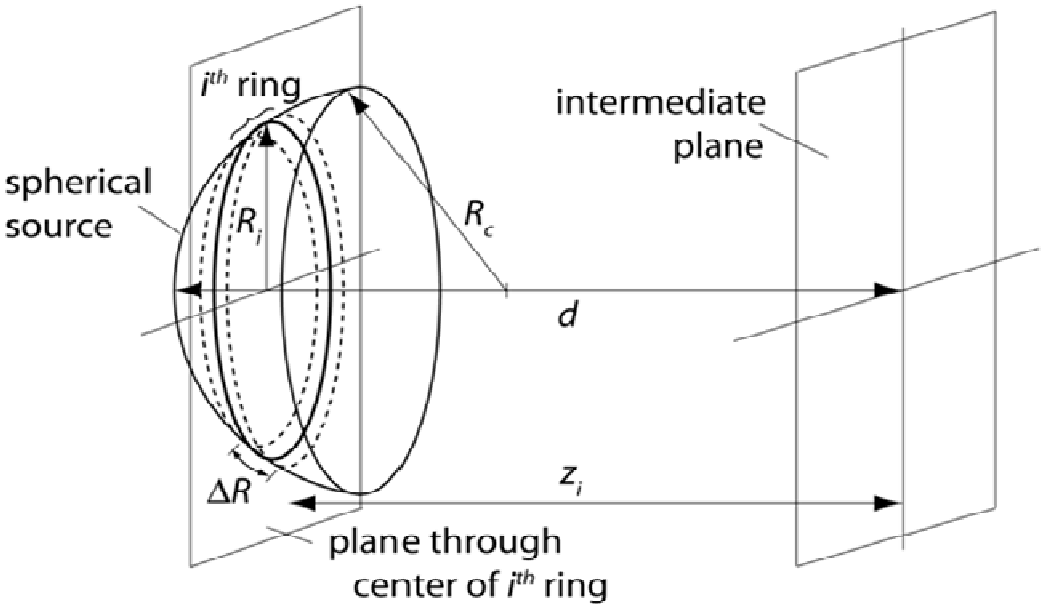


Figure 9. A set of planes parallel to the intermediate plane divides the source into a set of consecutive rings, with the center of each ring located on the dividing plane at a distance zi from the intermediate plane. The furthest point on the transducer is a distance d from the intermediate plane.

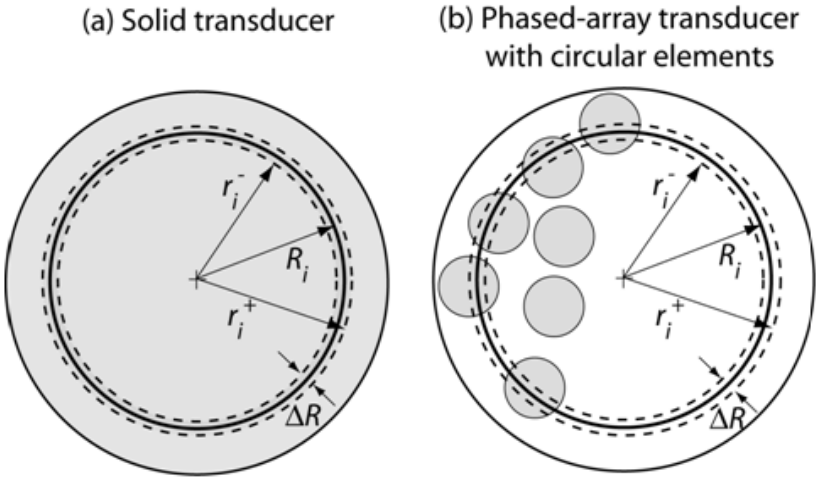


Figure 10. Ring-Bessel method dividing (a) solid or (b) phased-array transducer into rings of arc width ΔR. Shown between the dashed circles is the surface of the $i^{th}$ ring rotated onto a plane parallel to the intermediate plane. The center of the ring has radius $R_i$. All rings are circular and fill the entire transducer surface.

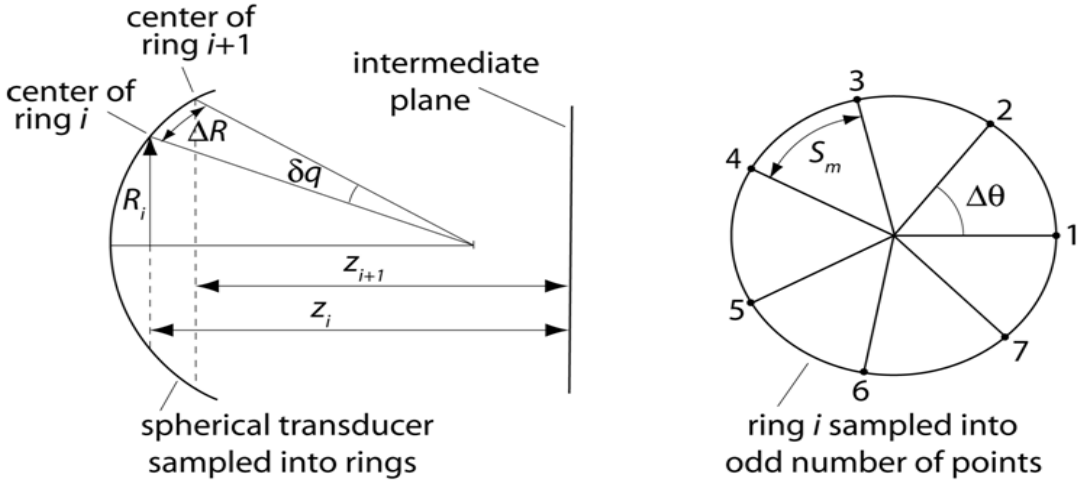


Figure 11. Sampling of the transducer surface into rings (left), and points (right). When the ring intersects an element of a phased array, those points on the ring are given the velocity amplitude and phase of the element. Points outside an element are given values of zero.

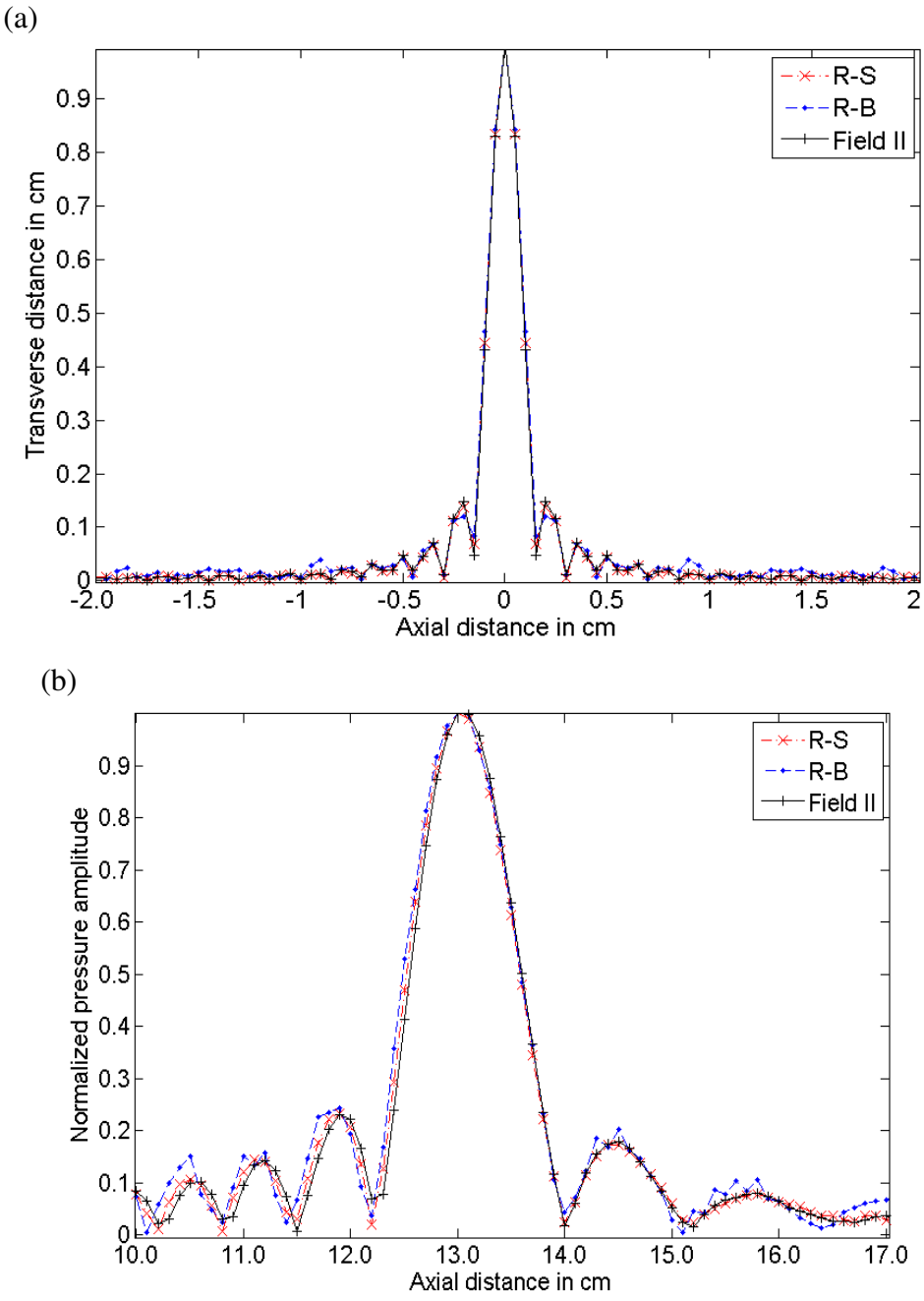


Figure 12. Normalized pressure amplitude predicted by the R-B, R-S and Field II techniques along a center line through the focal zone in the (a) transverse plane and (b) axial plane for a spherical curved solid transducer.

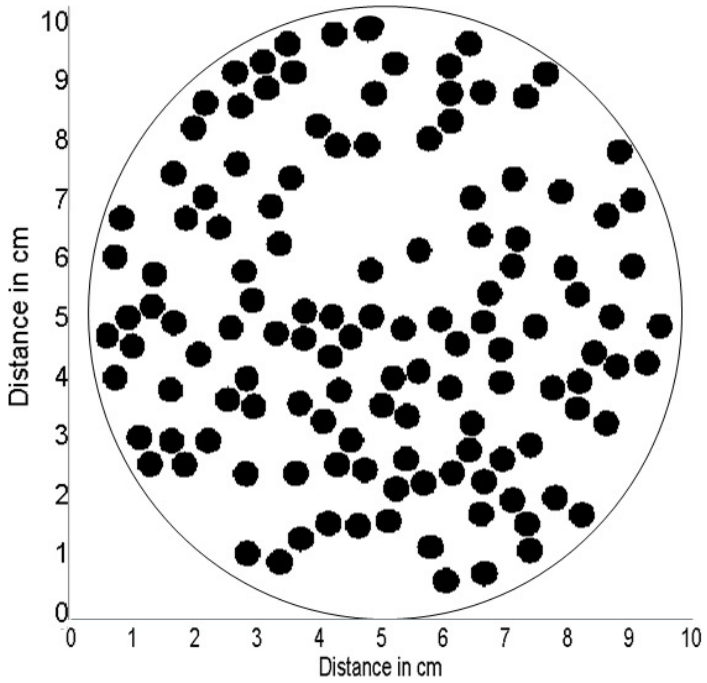


Figure 13. Face view of the 128-element phased-array transducer with randomly placed circular elements.

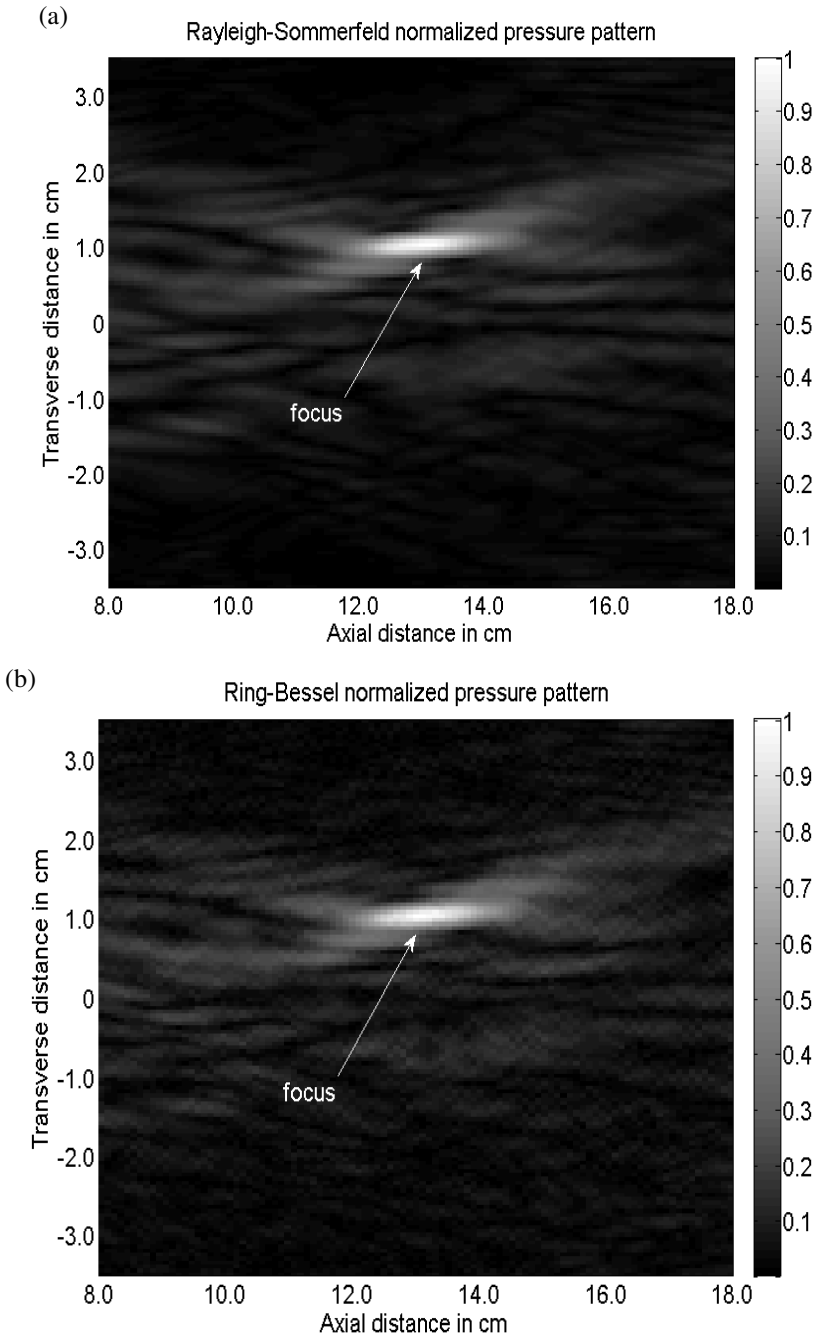


Figure 14. Axial slices of the magnitude of the pressure through the center of focus produced by steering a 128-element phased-array transducer using (a) R-S and (b) R-B simulation from the source to the intermediate plane (at 8 cm), followed by an AS calculation.

# CHAPTER 6

# THE EFFECT OF ELECTRONICALLY STEERING A PHASED ARRAY ON NEAR-FIELD TISSUE HEATING

## 6.1. Introduction

The manipulation of an ultrasound beam's shape and location possible with phased-array transducers offers significant advantages in Magnetic resonance-guided high-intensity focused ultrasound (MRgHIFU) treatments, allowing spatial and temporal switching between beam patterns, correcting for phase aberrations due to heterogeneous media, and reducing artifacts (such as fluid motion and susceptibility effects) in the MRI images that are often associated with mechanical transducer translation. Indeed, previous studies have indicated that MRgHIFU treatment times can be reduced through the use of phased-array transducers [76-78].

For effective, accurate and fast thermal treatments, the design objectives for a phased-array transducer include a small focal size, eliminating grating lobes, suppressing side lobes, maximizing the range of electronic steering in 3D and achieving maximum pressure at the focal zone [79]. These objectives are achieved by manipulating the frequency of operation, radius of curvature, number of elements, interelement spacing,

and element size and aperture diameter of the transducer. Tradeoffs between these parameters, the cost of manufacturing and control electronics, and difficulty of fabrication constrain the HIFU phased-array transducer design. Current HIFU transducer configurations vary in the number of elements (256-element [65], [80], 512-element [81], [82], and 1000 element systems [64]), frequency of operation (670 kHz to 4 MHz [83]) and the interelement spacing (random, semirandom and fully sampled); each configuration represents a tradeoff between transducer complexity and the desired beam characteristics for a specific clinical application.

This study concentrates on the analysis of near-field thermal buildup when using a phased-array transducer. Several investigators have noted that such thermal buildup occurs in the proximal tissues when executing a treatment with a phased array [78], [84], [85]. This paper extends those studies in two ways. First, it quantifies the extent of increase in the near-field tissue temperatures when electronically steering a phased-array transducer compared to mechanical motion using both simulated and experimental studies. Second, it compares the effect of manipulating transducer design parameters on near-field power deposition by simulating several different transducer configurations.

## 6.2. Methods

### 6.2.1. Simulation

All acoustic beam simulations were performed using the Hybrid Angular Spectrum method [60]. The homogeneous tissue model was 10x10x10 cm with isotropic spatial resolution of 1 mm; the assumed tissue acoustic and thermal properties are listed in Table 5. The radius of curvature was fixed at 13 cm for all transducers analyzed, and

the furthest point on each transducer was located 8-cm away from the beginning of the tissue model. More detailed transducer parameters are given in Table 6.

Thermal responses were calculated using a finite-difference approximation of the Pennes' bio-heat transfer equation [86],

$$\rho c_t \frac{\partial T}{\partial t} = k\nabla^2 T - wc_b(T - T_b) + Q_{ap} \tag{31}$$

where $\rho$ is the tissue density, $c_t$ and $c_b$ are the specific heats of tissue and blood, respectively, $k$ is the thermal conductivity, $T_b$ is the arterial blood temperature, $w$ is the Pennes' perfusion, and $Q_{ap}$ is the applied power density. Spatial and temporal resolutions were 1 mm and 0.05 s for all thermal simulations. Thermal dose was calculated based on the formulation given in [86].

### 6.2.2. Experiments

Experiments were conducted using an MR-compatible 256-element phased-array (Transducer #1 in Table 6) HIFU system (Image Guided Therapy, Bordeaux, France) in a 3T Siemens Trio MRI. The experimental setup is shown in Figure 15. Temperature measurements were acquired using the proton resonance frequency method [87]. A 3D segmented echo planar imaging (EPI) sequence (2x2x2 mm, 6.2-s resolution, TR/TE (ms): 20/9.5, FA: 20°, matrix: 64x128x32) was used to acquire the temperature data. Images were reconstructed using a referenceless technique [88] to reduce any susceptibility effects caused by transducer movement during mechanical translation. All images were postprocessed using zero-filled interpolation, resulting in an isotropic spatial resolution of 1 mm [89].

Two path trajectories were evaluated, as detailed in Figure 15. Both linear raster [90] and circular path patterns [84], [91] are commonly used in focused ultrasound treatments. Here we used a single-plane, nine-position raster pattern with 1-cm spacing and a 1.6-cm diameter circular pattern composed of 12 discrete points. In the raster pattern trajectory, the ultrasound beam was steered either mechanically or electronically. During mechanical steering, the transducer was translated in the *x*-*y* plane through the nine points with a continuously applied power of 35 acoustic watts. During electronic steering, the transducer was centered directly beneath position 5 (Figure 15) and the ultrasound beam was steered electronically to treat the remaining eight points; the applied power was varied between 35 and 50 acoustic watts when steering away from the center position to compensate for known steering losses [84], depending upon location, that were determined during system calibration tests. Each point was sonicated for 30 s with no cooling period between points.

For the circular path, only electronic steering was used in the experiment. Since fast temporal switching between points in the circle (faster than 200 ms), is not possible for the mechanically steered case, simulated results were substituted by translating the calculated beam pattern transversely corresponding to the respective raster points. For the experiment, the transducer was centered at the center of the circle and each point was sonicated by electronically steering the ultrasound beam at 235 acoustic watts. Within each circular cycle, each of the 12 points was sonicated for 200 ms. The trajectory was continuously repeated 25 times for a total sonication time of 60 s, meaning each point received cumulative sonication for a total of 5 s.

## 6.3. Results

The accumulated thermal dose from executing the nine-point raster pattern through either mechanical or electronic steering is displayed in Figure 16 for planes at various locations between the transducer and the focal plane. An increased amount of thermal dose is deposited in the proximal tissues at all locations when electronically steered. However, there is more than 50 times less thermal dose delivered in the focal zone for the electronically steered trajectory despite the increase of applied power when steering to off-axis points to compensate for calibrated steering losses. This effect is clearly seen in Figure 17. The mean of the 25 voxels containing the highest thermal dose in each *x-y* plane is plotted as a function of distance from the transducer's distal face.

Increased temperature rise in the near-field and therefore increased thermal dose accumulation, can also be seen when executing the 16-mm diameter circle trajectory. The thermal dose accumulated in several x-y planes along the ultrasound beam's axis for both electronic and mechanical steering is shown in Figure 18. Experimental and simulated electronically steered results are compared to the simulated mechanically steered case. For the electronically steered case, the experimental results agree reasonably well with the simulation results, both resulting in a noticeable accumulation of thermal dose at a location approximately 1.5 cm proximal to the focal zone (at z=11.5 cm). The mean of the 25 voxels containing the highest thermal dose in various x-y planes perpendicular to the transducer's axis is plotted for the electronically and mechanically steered cases in Figure 19. All above experiments and simulations were performed in a zero-perfusion environment using the same tissue-mimicking phantom [92]. Figure 20 displays

simulation results showing the effect of perfusion on the dose accumulated in various planes throughout phantom.

Table 6 lists the different transducer configurations (changing aperture size, frequency of operation or number of elements) that were analyzed in order to decrease the effect of near-field heating, and compares the performance of these transducers to the transducer employed in the above tests (#1). The transducer beam characteristics used for comparison are near-field clutter, maximum specific absorption rate (SAR) deposited in the focal zone and focal zone size. The near-field clutter is quantified using a near-field deposition ratio $\gamma$ defined as

$$\gamma = SAR_{max,NF} \Big/ SAR_{max,FZ}, \tag{32}$$

where $SAR_{max,FZ}$ is the maximum SAR deposited in the focal zone and $SAR_{max,NF}$ is the maximum SAR deposited in the near field with the near field defined as the region between the transducer face and the x-y plane 2.5 cm proximal to the focal zone in the axial direction. This ratio was calculated both for the case of a transducer focused at its geometric focus and electronically steered 1 cm in the vertical, horizontal and axial directions. Figure 21 displays the mean SAR deposited in the five voxels with the highest SAR value in various transverse planes for simulations of the four transducers. Two conditions are shown: (1) the beam focused at its geometric focus, and (2) the focal spot steered 1 cm in all three directions. The SAR for each transducer is normalized to the maximum SAR deposited at the geometric focus by the transducer #1 in Figures 21a and b, or normalized to each individual case in Figures 21c and d.

## 6.4. Discussion

The electronic steering capability of a phased array offers many advantages in MRgHIFU. It is well suited to the MRI environment where fluid motion and susceptibility artifacts should be minimized. It allows the user to vary the size and shape of the ultrasound spot and allows for very fast temporal switching between sonication points, offering more flexibility during a treatment. However, this study has shown that electronically steering a 256-randomized element phased array can significantly increase the thermal dose deposited in the near-field region.

In order to compare mechanical and electronic steering scenarios, two trajectories were evaluated. Both studied trajectories show a local accumulation of thermal dose occurring approximately 1 to 2-cm proximal to the geometric focus (seen in Figure 17 and, more noticeably, in Figure 19). During mechanical steering, the thermal build-up in the near field is due to beam overlap and prefocus absorption of the incident beam. Indeed this effect has been seen with a single-element focused transducer that was mechanically scanned through a defined trajectory [93]. However, the near-field thermal build-up is more pronounced for the electronically steered case both because beam overlap is greater when coming from a fixed, non-translating transducer center, and because of grating lobe clutter that is added to the main lobe overlaps. Grating lobe clutter also generally becomes worse as the steering angle is increased.

When comparing mechanical and electronic steering trajectories, differences in the effective acoustic exposure window size will affect the thermal dose accumulation in the proximal tissues. The larger acoustic window concomitant with mechanical scanning provides more volume to dilute the effects of near-field thermal build-up. However, in

this study, the mechanical movement of the transducer was small compared to the diameter of the transducer (< 13%). This increase of acoustic window area does not fully account for the four-fold higher thermal dose in the near-field region when comparing mechanical to electronic steering as seen in Figures 17 and 19.

Both trajectories were fairly simple, meaning they were not designed to ablate a defined volume of tissue. In other studies [84], [90], [91], both trajectory types have been extended to ablate defined volumes by adding additional points and planes. This extension would result in an increased total sonication time, exacerbating the effect of increased near-field build-up.

The average interelement spacing in the transducer #1 is approximately 6λ. In order to decrease grating lobe clutter, this element spacing should be as close to λ as possible; the alternative transducer configurations investigate different techniques to reduce this spacing. Transducer #2 in Table 6 reduces the interelement spacing by reducing the aperture size of the transducer (hence packing the elements closer, reducing average interelement spacing to ~3λ). The tighter packing limits the radius of each element to 0.2 cm. Figures 21a and b show that transducer #2 deposits less power in the focal zone compared to transducer #1 because of the smaller element size and larger focal zone size (Table 6). Figures 21c and d show that, as expected from the tighter packing of elements, the percentage loss in SAR due to electronic steering for transducer #2 is lower than that seen in transducer #1; however transducer #1 still deposits more SAR during electronic steering in the focal zone (and the near-field) due to its larger element size. The reduction in aperture size decreases the interelement spacing and should in theory reduce the grating lobe clutter; however the effects of a larger focal zone, smaller area in the

exposure window and less total power output of the transducer lead to the near-field deposition ratio γ for transducer #2 being larger for transducer #1.

Transducer #3 in Table 6 reduces the frequency of operation, thereby increasing the wavelength. Keeping the same absolute random element spacing as transducer #1, an increase in the wavelength reduces the average interelement spacing to 3λ at 0.5 MHz. This configuration retains the same element size (keeping total power output equal) and aperture size (keeping the exposure window equal) as transducer #1. Figures 21a and b show that transducer #3 deposits more SAR in the focal zone compared to transducer #2 even with a lower frequency and with a larger focal size. Reducing the interelement wavelength spacing (decreasing the percentage power lost when steering) while maintaining a large aperture size (spreading the prefocal beam over a larger area) improves the near-field deposition ratio γ of transducer #3 compared to transducer #1 for the steered case, from 0.067 to 0.044. However, the lower frequency of transducer #3 reduces the SAR deposited at the focal zone compared to the transducer #1 due to the dependence of absorption on frequency, and hence it has a worse near-field deposition ratio of 0.04 for an unsteered beam.

Transducer #4 is fully sampled (with the interelement spacing equivalent to λ) with 2025 elements while keeping the operating frequency equal to 1.0 MHz. With an interelement spacing of 1.5 mm, the element radius is restricted to 0.07 cm. Figure 21 shows that, as expected, this transducer loses substantially less power due to steering compared to transducer #1, and grating lobes are eliminated by an interelement spacing of λ. A larger focal size (due to a smaller aperture diameter) results in reduced SAR deposited in the focal zone. This effect is seen in the worse near-field deposition ratio for

transducer #4 compared to transducer #1. For a fully sampled transducer to have an equal size of focus as the transducer #1 (at 1.0 MHz), 10,205 elements are needed. While transducers have been constructed on this scale, it drastically increases the cost of fabrication, a tradeoff that needs to be considered during the design process.

## 6.5. Conclusions

Phased-array transducers offer many advantages to MRgHIFU treatments. However, the simulation and experimental results in this study show that because of more pronounced near-field heating, there are some disadvantages to using electronic steering. These effects should be taken into account during the design and characterization of a HIFU transducer, as well as in the treatment planning and monitoring process.

Table 5. Tissue properties used in simulations

| | |
|---|---|
| Density ρ ($kg/m^3$) | 1000 |
| Specific heats $c_t$, $c_b$ (kJ/kg-K) | 4186 |
| Thermal conductivity k (W/m-K) | 0.45 |
| Perfusion w ($kg/m^3$-s) | 0, 1, 5 |
| Attenuation (Np/cm-MHz) | 0.05 |
| Speed of sound (m/s) | 1538 |

Table 6. Transducers analyzed and summary of results

| | | | Transducer Configuration | | | |
|---|---|---|---|---|---|---|
| | | | # 1 | # 2 | # 3 | # 4 |
| Physical Configuration | radiating surface intensity ($W/cm^2$) | | 2.0 | 2.0 | 2.0 | 2.0 |
| | radius of curvature (cm) | | 13 | 13 | 13 | 13 |
| | aperture diameter (cm) | | 15.4 | 10.3 | 15.4 | 6.8 |
| | frequency (MHz) | | 1.0 | 1.0 | 0.5 | 1.0 |
| | number of elements | | 256 | 256 | 256 | 2025 |
| | element radius (cm) | | 0.33 | 0.2 | 0.33 | 0.07 |
| | element location | | random | random | random | fully sampled |
| | average interelement spacing | | 6λ | 3λ | 3λ | 1λ |
| Beam Characteristics | near-field deposition ratio γ | unsteered | 0.03 | 0.07 | 0.04 | 0.08 |
| | | steered | 0.07 | 0.07 | 0.04 | 0.08 |
| | maximum SAR at focus (x $10^8$ $W/m^3$) | unsteered | 1.0 | 0.14 | 0.16 | 0.14 |
| | | steered | 0.4 | 0.09 | 0.11 | 0.11 |
| | focal size (transverse x axial) (mm) | | 1.6 x 7.2 | 2.4 x 15.3 | 3.3 x 14.5 | 3.4 x 32 |

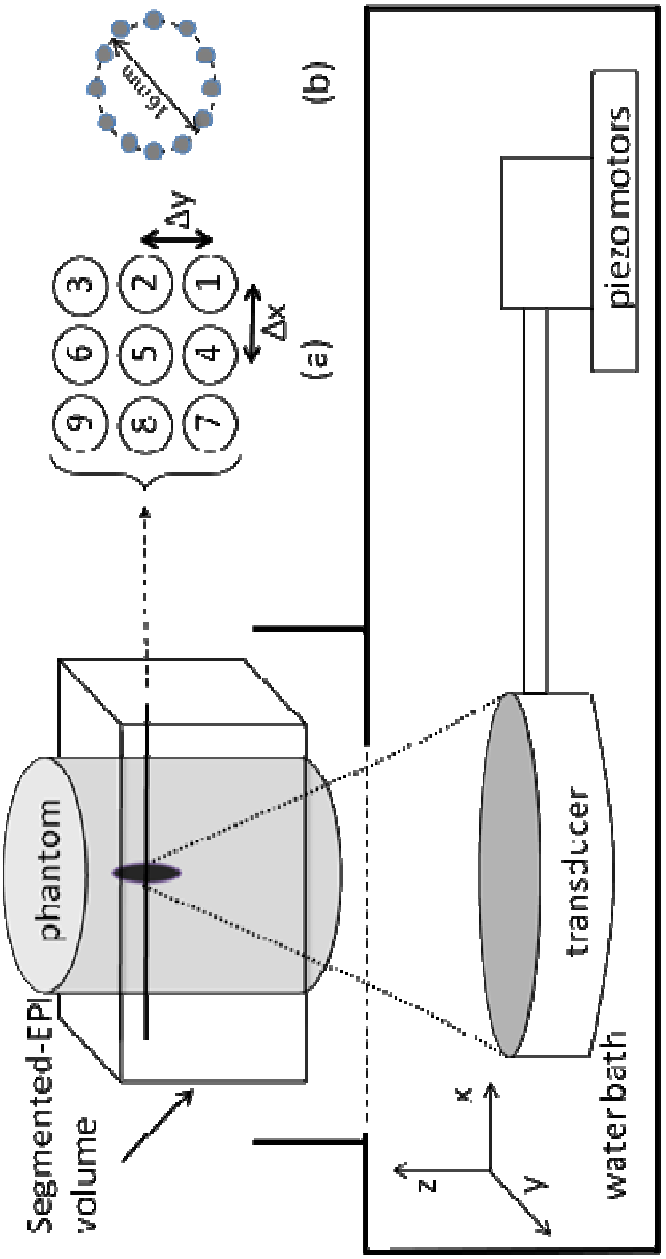


Figure 15. Schematic of the experimental setup. The phased-array transducer, tissue-mimicking phantom, 3D segmented EPI volume location, and scan path patterns in an x-y plane projection are all shown. (a) Nine-point scanning pattern, $\Delta x=\Delta y=1$ cm. (b) Twelve-point, 16-mm diameter circular scanning pattern.

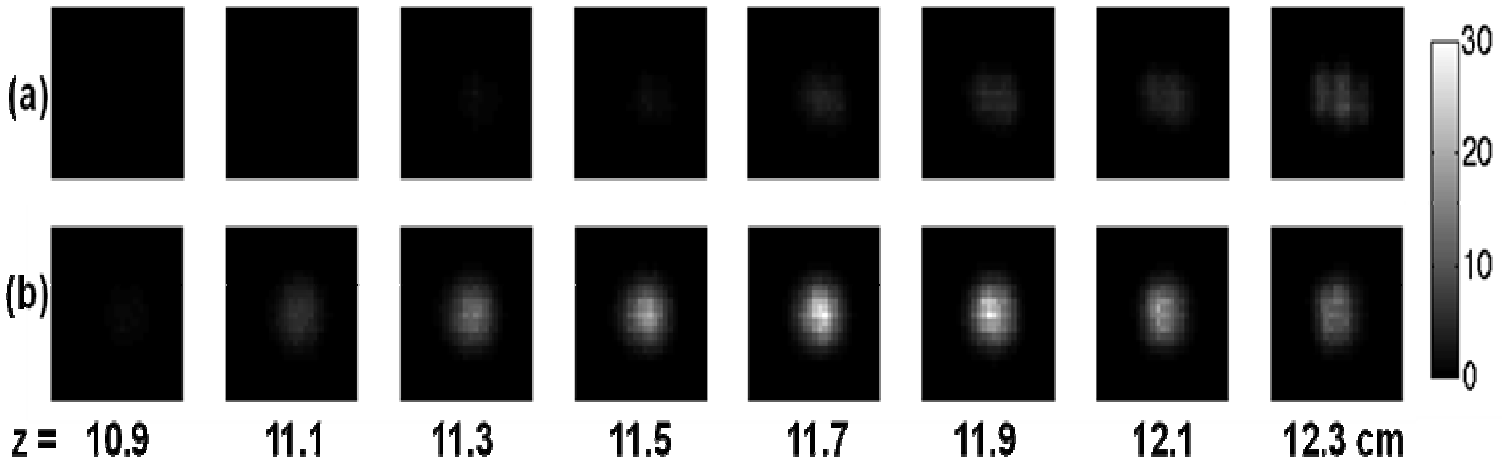


Figure 16. Experimentally determined thermal dose accumulated in the proximal regions of a tissue-mimicking phantom for the nine-point raster scan with the focal plane of the trajectory located at z = 13 cm. The (a) mechanically and (b) electronically steered trajectories are shown at distances measured from the transducer's distal face. Each position was sonicated for 30 s at 35 acoustic watts for the center point and up to 35-50 acoustic watts for the most off-axis points to compensate for known steering losses.

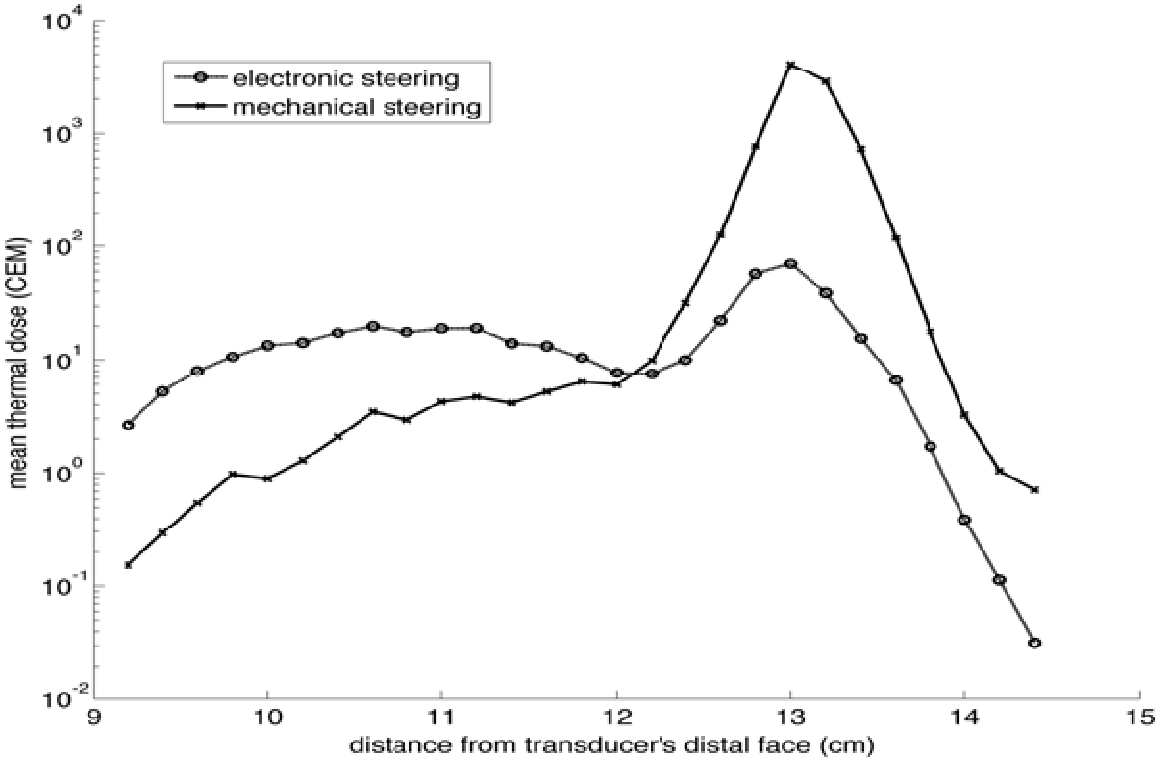


Figure 17. Log plot of the mean of the 25 voxels with the highest thermal dose accumulated in planes perpendicular to the ultrasound beam's axis during the nine-position raster trajectory at various distances from the transducer. The thermal dose accumulation for mechanical steering (solid curve) and electronic steering (dashed curve) are both shown.

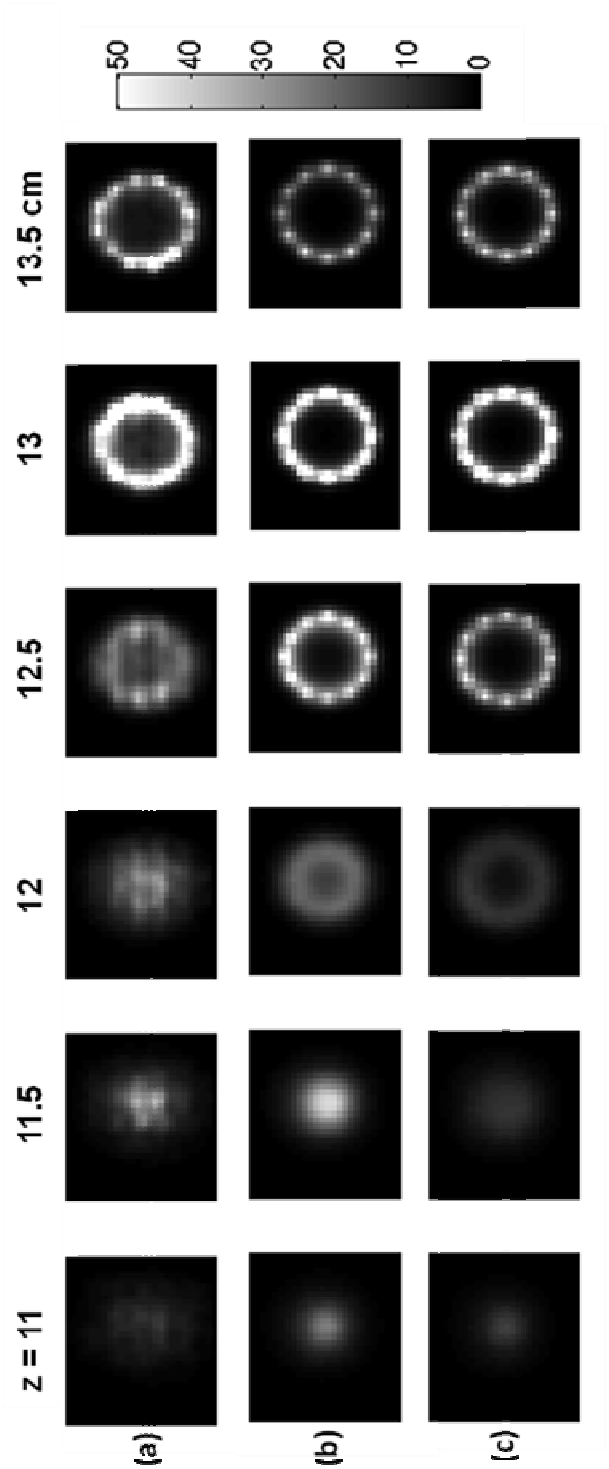


Figure 18. Thermal dose accumulated during the 16-mm circle trajectory in various x-y planes along the transducer's axis for both electronically and mechanically steered trajectories. Electronically steered (a) experimental and (b) simulated data, and (c) simulated mechanically steered data. The focal plane for the ultrasound beam is located at z = 13 cm. Total sonication time was 60 s at an acoustical power of 235 W.

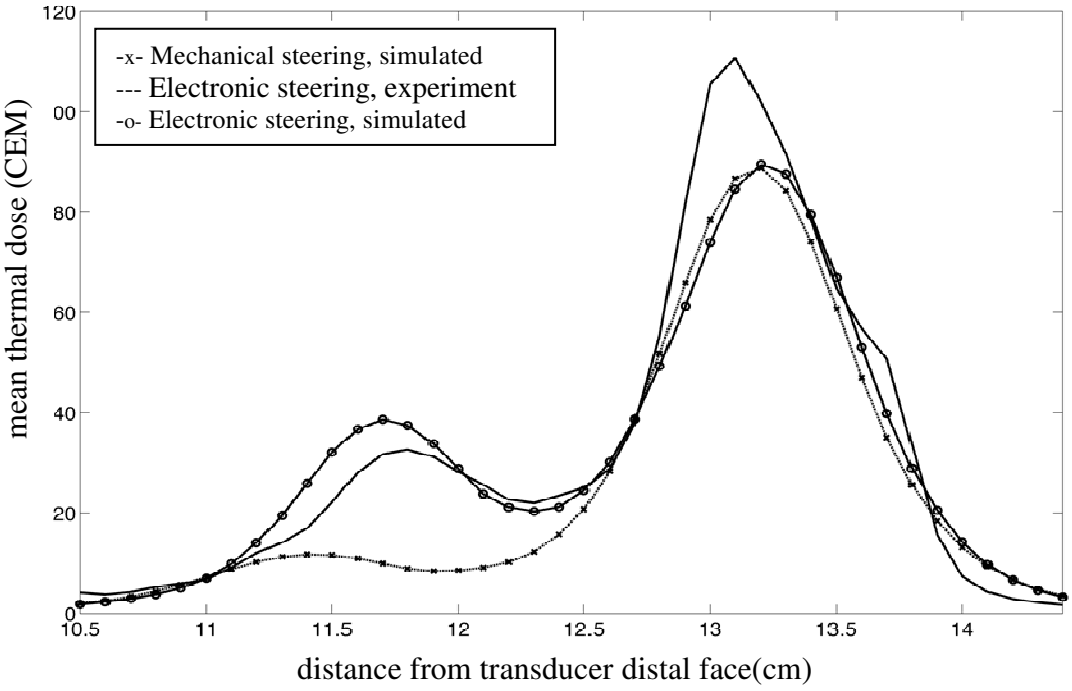


Figure 19. Mean of the 25 voxels with the highest thermal dose accumulated in planes perpendicular to the transducer's axis for the 16-mm circle trajectory. The focal plane is at 13 cm. Both experimental and simulated results are displayed for electronic steering, and simulated data for mechanical steering.

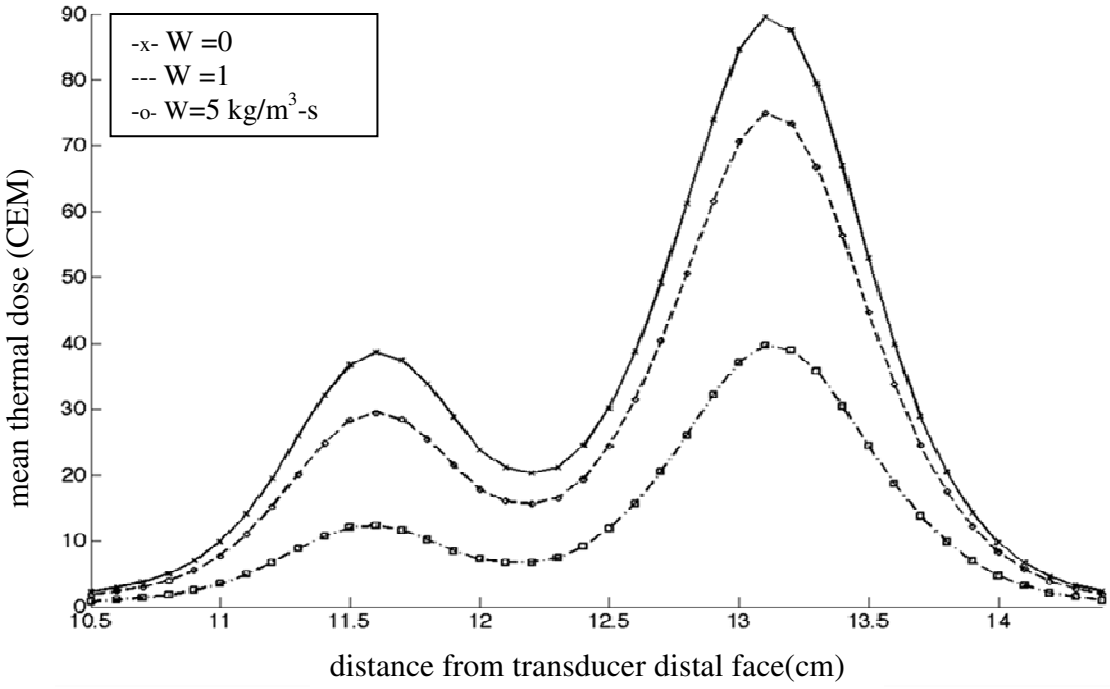


Figure 20. Effect of perfusion on the mean of the 25 voxels with the highest thermal dose accumulated in planes perpendicular to the transducer's axis for the 16-mm circle trajectory. Pennes' perfusion values of 0, 1 and 5 kg/m$^3$-s are shown.

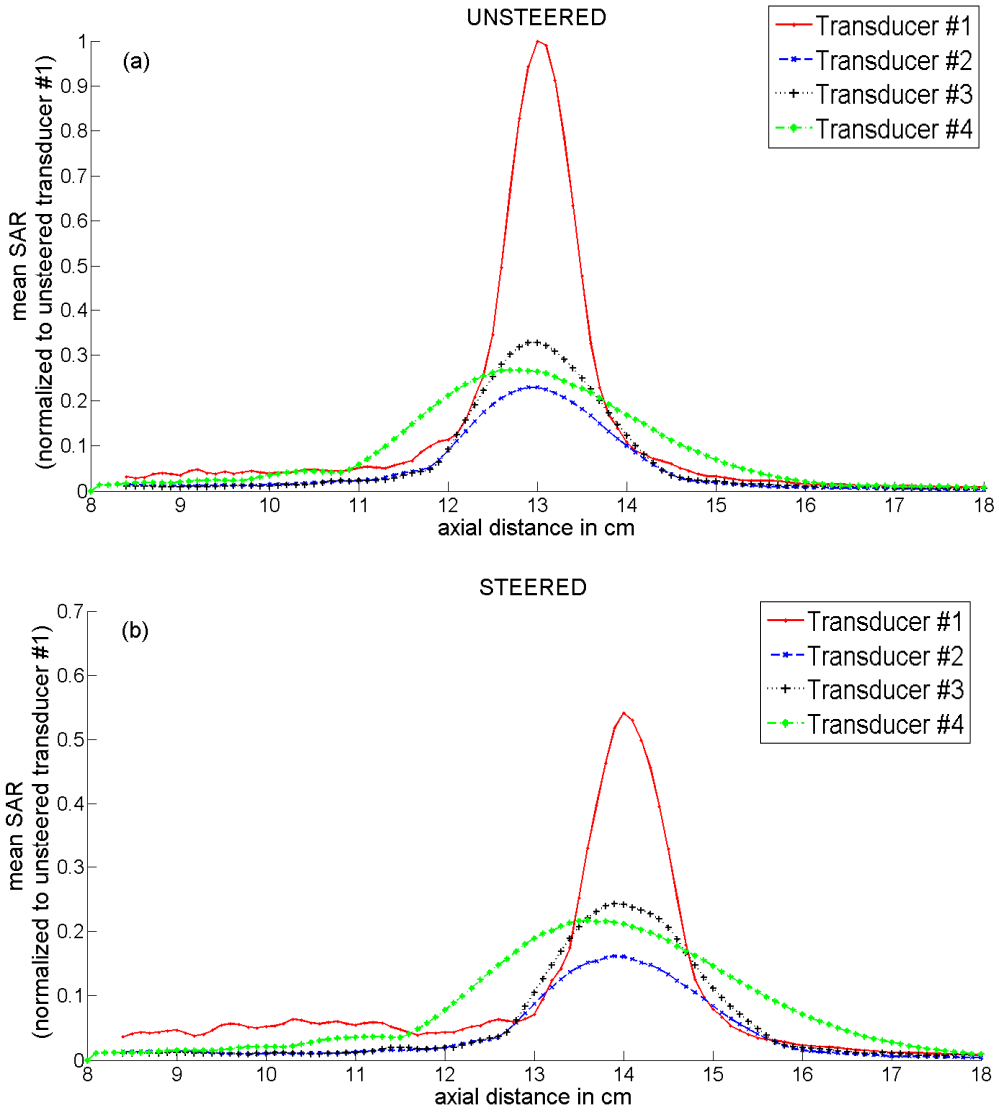


Figure 21. Plots of mean SAR deposited at five maximum voxels in planes perpendicular to the transducer's axis for four transducer configurations. Two cases are shown: (a) an unsteered beam; (b), a beam steered 1 cm in all directions. The SAR for each transducer is normalized to the SAR deposited at the geometric focus of transducer #1.

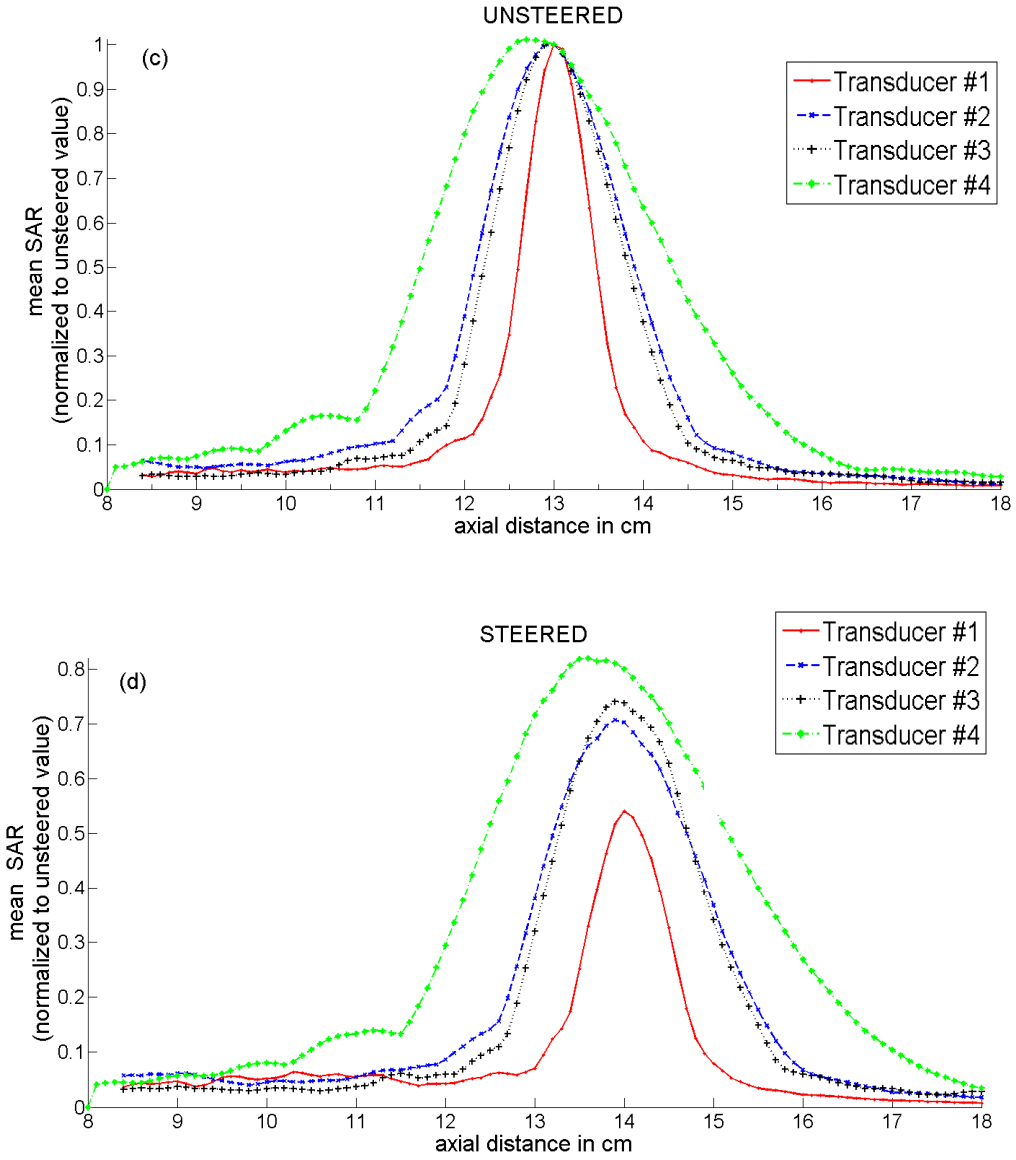


Figure 21. Plots of mean SAR deposited at five maximum voxels in planes perpendicular to the transducer's axis for four transducer configurations. Two cases are shown: (a) an unsteered beam; (b), a beam steered 1 cm in all directions. The SAR for each transducer is normalized to the SAR deposited at its the geometric focus.

# CHAPTER 7

# NONINVASIVE PATIENT-SPECIFIC ACOUSTIC PROPERTY ESTIMATION FOR TREATMENT PLANNING IN MRI-GUIDED FOCUSED ULTRASOUND SURGERY

## 7.1. Introduction

Magnetic resonance-guided focused ultrasound surgery (MRgFUS) is a means of causing noninvasive selective tissue necrosis using a high-intensity ultrasound beam and MR temperature monitoring. The location, shape and amplitude of the beam's focus is affected by the reflection, refraction and attenuation of the ultrasound beam due to variation of acoustic properties (speed of sound and attenuation coefficient) in the medium of propagation. Correction and control of these focal aberrations is accomplished using predictions from beam propagation techniques. The accuracy of these predictions depends primarily on the values of acoustic parameters used in the tissue model. Published tissue speed of sound and attenuation coefficient values vary significantly [14] with a three-fold variation in reported values of absorption coefficient of liver at 1 MHz [39]. The latest compilation of tissue acoustic properties [14] cautions readers about the large variations in data reported due to different measurement techniques, tissue types,

and tissue preparations used by different investigators, and also diversity in tissue due to age, abnormality, and normal biological variation from subject-to-subject. Only 11% of the experiments reported in review [39] were *in-vivo* and some values for tissue properties were reported using only one sample. Animal formalin fixed tissue samples with significantly different acoustic properties than fresh tissues [15], [61] and with invasive thermocouples that cause errors due to viscous heating at the interface of the medium and the thermocouple were frequently used [40-42].

Several published studies [17], [43], [47], [44] have shown that tissue attenuation coefficient values increase significantly (two-fold or more) and irreversibly at the high temperatures, that are common in MRgFUS treatments. These irreversible changes in attenuation coefficient values are dependent on a complex set of treatment parameters: tissue type, heating time, rate of heating, and maximum temperature achieved. There has been much interest in quantifying these relationships, with different investigators treating tissues to different temperatures or for different times and measuring the resulting changes in attenuation [16], [17], [46], [48], [44]. The through-transmission technique used in these studies calculates an average attenuation coefficient over the tissue thickness. Additionally, the presence of a transmitting and receiving transducer on either side of the tissue sample is required and measurements cannot be made noninvasively during treatment.

Recently, a method has been suggested that uses MRI calorimetry to measure absolute values of the tissue absorption coefficient [15]. A calorimeter constructed with the tissue sample (of a size smaller than the ultrasound beam) embedded inside a non-absorbing gel is insonated using an ultrasound transducer. By measuring the energy

absorbed in the calorimeter using MR temperature imaging (MRTI), the absolute absorption of the tissue sample can be obtained. The technique requires construction of a gel block with the sample embedded inside the gel (with good acoustic coupling between the gel and sample) and assumes the beam profile in the gel block to be equal to the beam profile measured in water.

Techniques that cause a small temperature rise in a tissue and use the heating or cooling segment of the temperature curve (measured using a thermocouple) have been used previously to measure the tissue absorption coefficient [17], [42], [94], [95]. In this paper we use the rate-of-temperature-increase technique [95] with an optimization routine, MRTI, and a fast beam propagation technique to noninvasively estimate subject-specific tissue acoustic properties.

## 7.2. Methods

The technique described in this paper minimizes the squared difference between an experimentally obtained power deposition pattern ($SAR_{exp}$ obtained using MRTI of low-power interrogation pulses) and a simulated power deposition pattern ($SAR_{sim}$ predicted using a fast beam simulation technique) to estimate tissue acoustic properties (speed of sound and attenuation coefficient). An optimization routine adjusts the acoustic properties used by the beam simulation technique for each prediction of $SAR_{sim}$: the acoustic properties in the beam simulation technique that result in the minimization of a cost function $J$ are considered an estimate of the acoustic properties of the media, where

$$J = \sum_{i=1}^{N} (SAR_{\exp,i} - K_i \times SAR_{sim,i})^2. \tag{33}$$

A scaling factor $K_i$ is multiplied to the $SAR_{sim}$ pattern to take into account the efficiency of the transducer, the acoustic coupling in the experimental setup, and a thermal correction factor to correct for errors in the $SAR_{exp}$ due to the restricted MRTI time step; $i$ denotes a voxel in a region around the focus with $N$ total voxels.

It has been shown theoretically and experimentally that specific absorption rate (SAR) information can be obtained from the rate of temperature increase (before thermal conduction or perfusion effects become significant) immediately following a step change in applied power [95]. In order to obtain $SAR_{exp}$, a short, low-power interrogation pulse is applied to the sample and MRTI is used to measure the resulting temperature change. The first few points in the heating curve are used to calculate the $SAR_{exp}$ in the sample as follows:

$$SAR_{exp,i} = c_{p,i} dT_i \Big/ dt, \tag{34}$$

where $c_{p,i}$ is the specific heat of the voxel $i$.

$SAR_{sim}$ patterns are obtained using our previously developed hybrid angular spectrum (HAS) beam propagation technique [60] that accounts for the effects of reflection, refraction and attenuation of the ultrasound beam in complex inhomogeneous media:

$$SAR_{sim,i} = \frac{2\alpha_i I_i}{\rho_i}, \tag{35}$$

where $\alpha_i$, $I_i$ and $\rho_i$ denote the attenuation coefficient, intensity (power density), and density at voxel $i$ respectively. The cost function $J$ in Eqn. (33) is reduced to

$$J = \sum_{i=1}^{N} (c_{p,i} \frac{dT_i}{dt} - K_i \times \frac{2\alpha_i I_i}{\rho_i})^2$$
$$= \sum_{i=1}^{N} (c_{p,i} \frac{dT_i}{dt} - \frac{efficiency}{thermal\ correction_i} \times \frac{2\alpha_i I_i}{\rho_i})^2, \quad (36)$$

where *efficiency* denotes the efficiency of the transducer. Using anatomical MR scans, each sample is segmented into subdomains by tissue similarity, each subdomain having unique acoustic properties. Initial estimate of the speed of sound and attenuation coefficient value of each subdomain is set using average values given in literature [39], and a $SAR_{sim}$ pattern is predicted using the HAS technique. In the subsequent iterations $SAR_{sim}$ is modified by adjusting values of the attenuation coefficient and speed of sound of each subdomain (using a simplex-based optimization routine) until the cost function $J$ is minimized. The input pressure pattern for the HAS technique (the pressure pattern from the curved transducer surface to the beginning of the segmented tissue model) is calculated using the element response function array technique [60] to reduce the run-time calculation times.

The $SAR_{exp}$ calculated using Eqn. (34) assumes that thermal conduction and perfusion effects are insignificant during the initial slope of the temperature curve. Using MRTI with a finite time-step of around 4 s (as in this study) results in errors in the determined $SAR_{exp}$ pattern, with the $SAR_{exp}$ underestimated at the voxels in the focal zone and the over-estimated in the voxels neighboring the focal zone; this thermal effect is modeled by simulating a dispersed beam pattern in the HAS beam prediction. The $SAR_{sim}$ pattern is calculated for a lower frequency (resulting in a larger $\lambda$ and a larger beam); the frequency dependent attenuation coefficient value is increased to compensate for the

lower frequency in the simulation. In subsequent implementation, this correction factor should be determined using thermal simulations based on the Pennes' Bioheat equation, for the experimentally used MRTI time-step and thermal conduction and perfusion values (using table value estimates) of the sample.

## 7.3. Implementation details

The implementation of the inverse parameter estimation technique involves the following steps:

a) Employing a calibration pulse in a homogeneous phantom

b) Segmenting the sample into subdomains

c) Employing an interrogation pulse the sample

d) Creating of region-of-interest and noise masks for optimization

e) Optimizing using the HAS technique and the $SAR_{exp}$ pattern

### 7.3.1. Calibration pulse in homogeneous phantom

The rate-of-temperature-increase technique can be used to estimate a combined variable, given by the right hand side of the following equation:

$$\frac{dT}{dt} \propto \frac{efficiency \times \alpha}{\rho \times c_p}.$$

In order to separate the attenuation $\alpha$ of the media from the combined variable, the transducer *efficiency*, $\rho$ and $c_p$ values must be estimated. Further, the beam propagation technique requires a value for the distance of the transducer from the sample in order to accurately predict the speed of sound in the sample. In our implementation, $\rho$ and $c_p$ of

the sample are set using table-value estimates, the efficiency of the transducer, the coupling in the experimental setup, and the distance of the transducer from the setup are estimated using a calibration pulse, as follows: Before the start of each experiment, a calibration pulse is applied to a homogeneous tissue-mimicking phantom placed in the MRgFUS setup. A step input of power is applied to the phantom and MRTI is used to obtain the $SAR_{exp.}$ The acoustic properties (speed of sound and attenuation coefficient) of the calibration phantom are identified before the experiment using the though-transmission substitution technique. $SAR_{exp}$ and the known acoustic properties of the phantom are then used to calculate the efficiency and the location of the transducer in the MR temperature image (to determine the distance of the transducer from the sample). These values will remain constant for the duration of the experiment. When the same tissue-type is used for the calibration pulse as for the property measurements, the calibration pulse also scales *efficiency* (and hence $K$) to take into account the disparity between the assumed and true values of the tissue density and specific heat.

### 7.3.2. Segmentation of sample into subdomains

The calibration phantom is replaced by the sample in the MRgFUS setup and anatomical images from MR sequences are used to segment the tissue sample into different subdomains, each segmented subdomain assumed to posses unique acoustic properties (speed of sound and attenuation coefficient). The number of subdomains is based on tissue similarity (using k-means clustering [96]) and on user input as determined by the particular application.

### 7.3.3. Interrogation pulse

A low-power interrogation pulse is applied to a tissue subdomain in the sample using the ultrasound transducer. $SAR_{exp}$ (found using Eqn. (34)) is determined in all regions that achieved a measurable temperature rise due to the interrogation pulse. A separate interrogation pulse is required for estimating the tissue properties in each segmented subdomain. The acoustic power and duration of the interrogation pulse are selected such that the temperature rise at the focal zone in the sample does not deliver any appreciable thermal dose (less than 10 equivalent minutes at 43℃) while maintaining sufficient temperature rise to overcome the background noise in the MRTI.

### 7.3.4. Region-of-interest and noise masks

A region-of-interest mask is created for the calculated $SAR_{exp}$ pattern that includes the focal zone and any prefocal heating seen in the sample. The cost function is minimized over this region. This eliminates $SAR_{exp}$ information from voxels where the expected ratio of ultrasound absorption-dependent temperature rise vs. temperature noise is low (occurring father from the main beam). Inside this region-of-interest another mask is used to disregard temperature information from noise-dominated voxels or voxels that were segmented as fat voxels. This is necessary since the PRF shift technique for measuring temperature does not provide reliable measurement in fat [97]. In this implementation, all voxels with a temperature fluctuation of more than 1.5 °C during the interval when the ultrasound transducer power is turned off (before heating and during cooling) are included in the noise mask and not included in the cost function calculation. The density values of all subdomains are assumed constant and set using table value

estimates [39]. The acoustic properties of water are considered constant (speed of sound 1500 m/s, density 1000 kg/m$^3$ and attenuation coefficient 0 Np/cm/MHz) and are not optimized.

### 7.3.5. Optimization routine

The $SAR_{exp}$ and $SAR_{sim}$ are both multiplied by the noise mask, and the squared difference between the two patterns (cost function) is calculated over the region-of-interest. An optimization routine is used to iteratively minimize this cost function by changing the speed of sound and attenuation coefficient values for all the tissue subdomains in the path of the ultrasound beam. The density values of all subdomains are assumed constant and set using table value estimates [39]. The acoustic properties of water are considered constant and are not optimized. In this study the optimization routine was run using the optimization toolbox in MATLAB 7.7. A simplex technique that minimized the cost function given in Eqn. (36) was used (function- *fminsearch* in MATLAB). The initial parameters (speed of sound and attenuation coefficient) for all tissue types are selected from table values estimates given in literature [39], facilitating faster convergence of the optimization routine.

## 7.4. Results

All experiments were performed in an MRgFUS system consisting of a Siemens TIM Trio 3T MR-scanner, a 256-element phased-array transducer (Imasonics, Bordeaux, France), and hardware and software for beam steering and data visualization (Image Guided Therapy, Bordeaux, France). The PRF technique [87] was used to measure

temperatures using transverse slices centered at the focal zone with a 2D gradient echo sequence with the parameters shown in Tables 7 and 8. Acoustic property measurements were made on the following samples: (a) homogenous tissue-mimicking phantoms, (b) *ex-vivo* porcine muscle, and (c) *in-vivo* rabbit thigh. The inverse parameter estimation technique was run on a 4-GB Windows laptop using MATLAB version 7.8 (with the optimization toolbox) and took about two minutes to converge for the homogeneous phantom and *ex-vivo* tissue studies, and one hour for the *in-vivo* study. Anatomical information for each sample was obtained using the 3-point Dixon sequences, which provide a ratio of adipose and non-adipose soft tissue within each voxel of the sample. For the validation study using the homogeneous tissue mimicking phantoms the segmented model had two subdomains: water and phantom. Tissue-mimicking homogeneous phantoms were made using original recipe given in [92], and a modified recipe that changed the attenuation coefficient by increasing the quantity of condensed milk added in the recipe (more condensed milk gives higher attenuation). The *ex-vivo* pork sample and the *in-vivo* rabbit model were segmented into three tissue types - water, fat and muscle. The *ex-vivo* porcine muscle samples were immersed in degassed water at room temperature for an hour before the experiment to remove any air absorbed in the sample. Fiduciary markers (nylon threads) were placed in the meat sample to assist in registration of the tissue between the MRTI and the TechniScan images (as described in later section). The *ex-vivo* tissue preparation was scanned in the TechniScan Whole Breast Ultrasound (WBU) Unit unit approximately one hour before interrogation pulses were applied in the MRgFUS setup. The Institutional Animal Care and Use Committee approved the animal experiment. One female white New Zealand rabbit was used for this

study. The thighs were shaved and depilatory cream was applied. The specific heat value for homogeneous phantoms (4186 $kJK^{-1}Kg^{-1}$), *ex-vivo* porcine muscle (3770 $WK^{-1}m^{-1}$), and *in-vivo* rabbit thigh (3770 $WK^{-1}m^{-1}$) were set using table value estimates [98]. The same initial parameters for the optimization routine were used for all the samples in the study (speed of sound 1500 m/s and attenuation coefficient 0.04 Np/cm/MHz).

In order to validate the accuracy of the presented inverse parameter estimation technique, two validation methods were employed.

### 7.4.1. Validation using the through-transmission substitution technique

The acoustic properties determined using the iterative parameter estimation technique were compared to those measured using an independent through-transmission substitution technique in homogeneous phantoms. The setup for the through-transmission technique is shown in Figure 22a. Two phantom recipes with different attenuation values were prepared and poured into separate molds. The acoustic properties of the phantoms measured using both techniques are given in Table 7. The ultrasound pulse power was 25 W and time was 30 seconds for each interrogation using the inverse technique.

### 7.4.2. Validation using the TechniScan ultrasound tomography system

Tissue acoustic properties of *ex-vivo* porcine muscle obtained using the iterative parameter estimation technique were compared to independent measurements from the TechniScan WBU tomography system [54], [99] (setup shown in Figure 22b). The TechniScan instrument uses inverse scattering tomography to calculate the acoustic properties in a given sample using a set of time-gated transmission and receiving

transducer arrays positioned on opposite sides of the sample. As the beams travel through the sample from the transmitting array to the receiving array, they are attenuated and reflected by the tissue inhomogeneities, providing data to enable a tomographic reconstruction of the tissue acoustic properties in each coronal plane of the scan. The TechniScan transducer arrays, operating at a center frequency of 1.25 MHz, rotate around the sample and also move along the axis of the sample, yielding a 3D map of the attenuation coefficient of the sample. The tomography unit results in a 3D property distribution with a spatial resolution of 0.4x0.4x2 mm. Interrogation pulses were applied to two locations in the sample in the MRgFUS setup and two values of attenuation coefficients were determined using the inverse parameter estimation technique. The average attenuation coefficient in a region (6x6x8 $mm^3$) around the same locations was calculated from the 3D TechniScan images for comparison with the inverse parameter estimation technique.

Previous authors have shown in *in-vitro* studies that the tissue's attenuation coefficient changes irreversibly with thermal dose due to treatment [17] (linearly with $\log_{10}$ of thermal dose). In this study we measured the changes in attenuation coefficient with $\log_{10}$ of thermal dose delivered during treatment in *in-vivo* rabbit thigh. The results are described below.

### 7.4.3. Attenuation changes in-vivo after MRgFUS treatment

A schematic of the experimental setup for the *in-vivo* study is shown in Figure 23. After the initial segmentation of the rabbit thigh into three tissue types (fat, muscle and water), a region in the rabbit muscle around the geometric focus of the beam (twenty-one

voxels in the slice centered at the focal zone, composed of three transverse voxels and seven axial voxels) was segmented into twenty-one different tissue types, to take into account the local inhomogeneities in the muscle. HIFU heating was monitored with a 2D gradient echo sequence with the following parameters: TR/TE = 45/10 ms, 2x2x3-mm spatial resolution (3-mm slice thickness) and 4.7-s temporal resolution. The following sequence of acoustic power was applied to each thigh: a low-power pretreatment interrogation pulse to estimate the initial attenuation coefficient (12 W acoustic for 30 s), a 10-minute cooling period, a high-power treatment pulse (31 W acoustic for 35 s) to cause change in attenuation due to thermal dose delivered [100], a 15-minute cooling period, and a posttreatment low-power interrogation pulse (12 W acoustic for 30 s) to measure the changed attenuation coefficient due to treatment. These experiments produced a total of 42 heated voxels (21 for each thigh). Due to the low Signal to Noise Ratio (SNR) during the animal experiment, the noise mask eliminated eighteen voxels. Pretreatment and posttreatment attenuation values at a total of twenty-four voxels were estimated using the optimization routine; the attenuation change ratio (posttreatment attenuation/pretreatment attenuation) was calculated for each voxel. Since the treatment pulse resulted in a heterogeneous distribution of thermal dose around the focal zone, each voxel had a unique value of thermal dose (with variation in $\log_{10}$ of thermal dose between neighboring voxels on the order of 0.01). In order to calculate the average change in attenuation with thermal dose, the data were divided into eight groups, each group with a range of $\log_{10}$ of thermal dose ± 0.2. Each group included three voxels; the average attenuation change ratio and the average $\log_{10}$ of thermal dose for each group were calculated and are plotted in Figure 24.

## 7.5. Discussion

A technique for noninvasive parameter estimation for MRgFUS is expected to be useful for developing treatment plans using subject-specific acoustic properties and also provide a means for making real-time treatment path decisions that can estimate and account for changes in attenuation coefficients with treatment. To validate the noninvasive inverse parameter estimation technique, the acoustic properties measured using this technique were compared to two independent techniques, the through-transmission technique for homogeneous phantoms and the TechniScan Whole Breast Ultrasound unit for inhomogeneous *ex-vivo* porcine muscle. Values of acoustic properties for the noninvasive technique were within 5% of those measured using the independent techniques as shown in Tables 7 and 8. The inverse parameter estimation technique was also used to measure changes in attenuation coefficient due to MRgFUS treatment in *in-vivo* rabbit thigh. A plot of the change in attenuation vs. $\log_{10}$ of thermal dose is shown in Figure 24. As shown by other researchers *in vitro* [17], the attenuation coefficient increases linearly with $\log_{10}$ of thermal dose and the slope (0.21) of the curve found using the noninvasive technique in *in-vivo* rabbit thigh (0.20) corresponds very well with the slope found by previous studies in *in-vitro* dog muscle [17].

### 7.5.1. MR temperature measurements

It has been shown that MRTI accuracy is a function of both spatial and temporal resolution [89]. Consequently, the voxel size and time step of the MR temperature measurements affect the accuracy of the experimentally determined SAR patterns and the estimated tissue acoustic properties. The rate of temperature increase technique assumes

that the initial slope of the temperature rise is calculated before the effects of thermal conduction and perfusion become dominant and hence the time-step of the MRTI should be as small as possible within the SNR constraints. While in the present implementation, this correction is modeled by predicting a broader beam using the HAS beam simulation, this thermal correction factor could be more accurately determined using thermal simulations to estimate the error caused by the restricted step size of the MRTI. Further, the thermal correction factor assumes perfusion does not change in the location (when doing experiments of attenuation changes in *in-vivo*, the perfusion before and after attenuation may be different.) Different thermal correction factors could be used by assuming different perfusion before and after ablation. Due to high SNR in phantom and *ex-vivo* porcine muscle experiments, the noise mask did not remove any voxels close to the focal zone from the cost function calculation. In the *in-vivo* rabbit thigh studies, the SNR was lower and the noise mask removed a higher number of voxels around the focal zone from the cost function calculation in the optimization routine. Improved RF coil design will increase SNR, allowing improvements in speed and voxel resolution of MR temperature measurements and improving the performance of the inverse parameter estimation technique.

### 7.5.2. Segmentation and convergence

The number of subdomains that the tissue is segmented into depends on the sensitivity of the sequence used for the MR anatomical scan. The 3-point Dixon technique used in this study provides a ratio of adipose and nonadipose soft tissue within each voxel of the sample, resulting in a small number of tissue subdomains. This results

in faster convergence of the optimization routine, but interrogation shots at different locations of the same subdomain may result in different estimates of the acoustic properties. For treatment path optimization studies where acoustic properties are required over a larger region, an MRI sequence that has higher sensitivity to tissue inhomogeneity than the 3-point Dixon technique should be used for segmentation. Alternatively, the entire tissue region around the ultrasound beam may be segmented into different tissue types (as in the *in-vivo* study) and the attenuation values for each voxel estimated independently of the surrounding tissue. This will increase the computation time for the convergence of the optimization routine. Care must be taken to only estimate tissue properties in locations where the intensity of the beam is high enough to dominate the temperature rise seen due to noise. A tradeoff between the speed of the convergence and the accuracy of estimates should be considered for different applications.

### 7.5.3. Calibration pulse

A calibration pulse is used to determine the *efficiency* value used in Eqn. (36) to estimate the effect of the experimental coupling and transducer efficiency. When using the same tissue-type for the calibration pulse as for the noninvasive parameter estimation technique, *efficiency* also scales the simulation SAR to take into account the disparity between the specific heat and density values assumed in the calculations, and those of the actual tissue sample. So in cases where an absolute value of attenuation coefficient is required, an extra calibration pulse is needed before the interrogation pulse. Alternatively, when using this technique to estimate changes in attenuation coefficient due to treatment

(as in the *in-vivo* study), using pre and posttreatment identification pulses at the same location, the calibration pulse is not needed.

### 7.5.4. Interrogation Pulse

A disadvantage of the inverse parameter estimation technique is the temperature rise that is required before acoustic properties can be estimated in a region. Although we have shown that the technique can be used *in-vivo* with very low-power interrogation pulses (giving a 6 to 8℃ temperature rise), a technique that can estimate subject-specific acoustic properties noninvasively without a temperature rise would be preferred. Despite this drawback, the authors feel that the significant advantage provided by the parameter estimation technique is its ability to noninvasively estimate changes in attenuation coefficient due to treatment. For the *in-vivo* study presented herein, a 10 minute cooling period was added before the posttreatment identification pulse was applied (for the tissue to reach normal temperature); alternatively an interrogation pulse could also be applied immediately after the treatment pulse to measure the time-course of the change in attenuation coefficient of the tissue. Further, repeated application of interrogation pulses after the treatment can also be used to measure if the tissue properties change irreversibly after the application of thermal dose.

### 7.5.5. Attenuation coefficient and absorption coefficient

The temperature rise seen in the tissue sample due to a step input in power is a result of the ultrasound absorption coefficient, while the beam simulation technique models the beam profile based on the attenuation coefficient. Although the attenuation

coefficient can be assumed to be very close to the absorption coefficient in tissues with low scatter, further studies to differentiate the attenuation coefficient from the absorption coefficient of tissue will be valuable.

## 7.6. Conclusions

A new technique to noninvasively estimate tissue acoustic properties *in-vivo* was presented and validated by comparing to two independent techniques in homogeneous and inhomogeneous phantoms. Subsequently, the technique was used to measure changes in tissue attenuation with $\log_{10}$ of thermal in *in-vivo* rabbit thigh. Future studies include applying this technique to different tissue types.

Table 7. Validation of optimization technique in homogeneous phantoms using through-transmission technique.

| Sample | Experimental Parameters for Optimization Technique | | | | | | Through-transmission |
|---|---|---|---|---|---|---|---|
| | Temperature parameters | | | | Estimated Tissue Property Values | | |
| | TE ms | TR ms | Time Step sec | Voxel Size mm | | | |
| Original Recipe[1] | 9 | 65 | 4.2 | 1x1x3 | Speed of Sound (m/s) | 1540 | 1510 |
| | | | | | Attenuation Coefficient (dB/m/MHz) | 5.5 | 5.6 |
| Modified Recipe | 9 | 65 | 4.2 | 1x1x3 | Speed of Sound (m/s) | 1540 | 1530 |
| | | | | | Attenuation Coefficient (dB/m/MHz) | 6.3 | 6.3 |

Table 8.Validation of optimization technique in inhomogeneous porcine muscle using TechniScan WBU unit

| Sample | Experimental Parameters for Optimization Technique | | | | | | | |
|---|---|---|---|---|---|---|---|---|
| Location | Temperature parameters | | | Interrogation Pulse | | Estimated Tissue Property Values | | WBU Unit |
| | TE ms | TR ms | Time Step sec | Power Watts | Time sec | | | |
| One | 8 | 50 | 4.3 | 22 | 30 | Attenuation Coefficient (dB/m/MHz) | 5.5 | 5.2 |
| Two | 8 | 50 | 4.3 | 25 | 30 | Attenuation Coefficient (dB/m/MHz) | 6.3 | 6.1 |

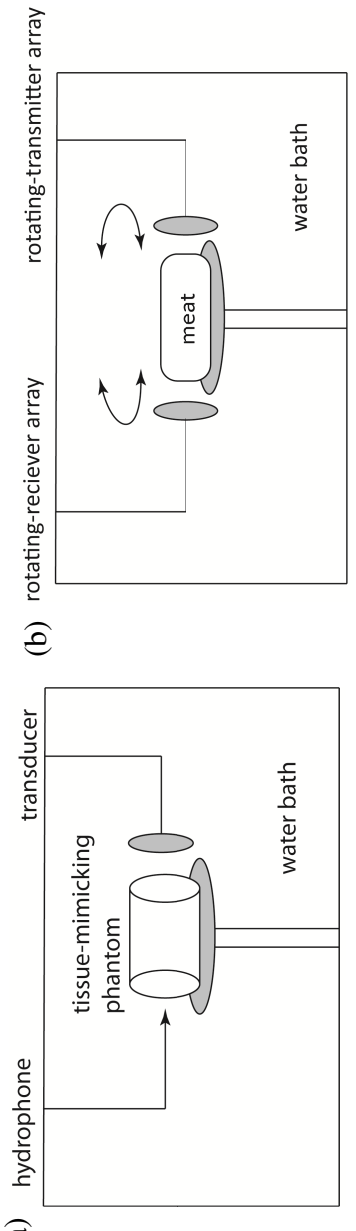


Figure 22. Schematic showing the experimental setup for the validation study in a) homogeneous phantom using the through-transmission technique, b) ex-vivo porcine muscle using the TechniScan WBU unit.

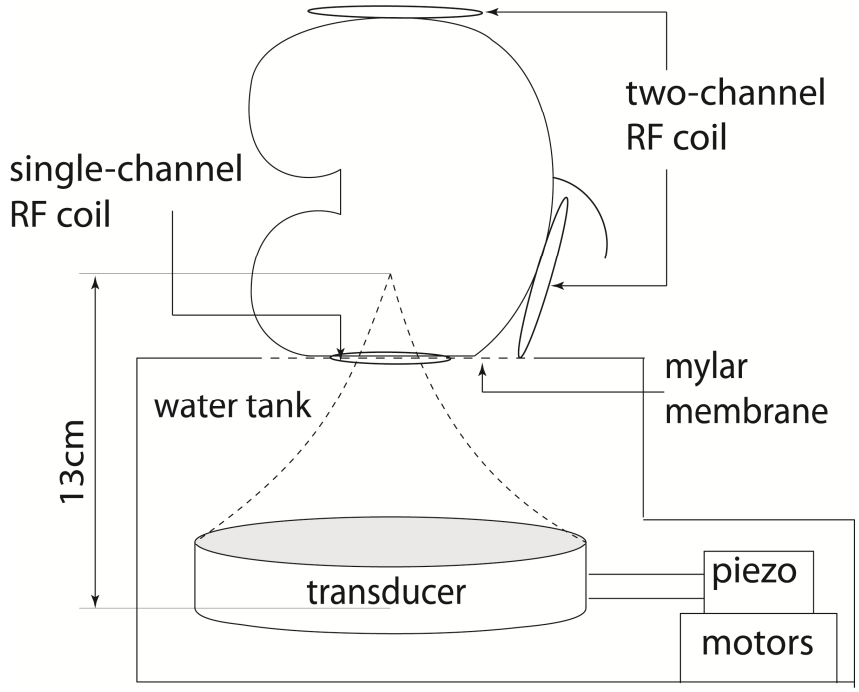


Figure 23. A schematic of the experimental setup for the inverse parameter estimation technique in *in-vivo* rabbit thigh. Three receiver coils are used, a single-channel shoot-though RF coil and two two-channel RF coils.

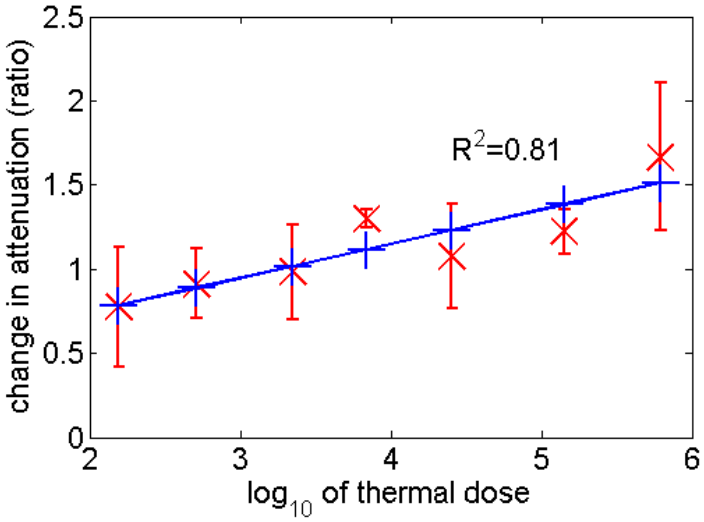


Figure 24. *In-vivo* estimates of the change in the attenuation coefficient with $\log_{10}$ of thermal dose using the inverse parameter estimation technique. Each data point is an average of the attenuation coefficient of three voxels within ±0.2 $\log_{10}$ of thermal dose.

# CHAPTER 8

# CONCLUSIONS AND FUTURE WORK

Use of numerical beam simulation techniques for treatment protocol planning in MRgFUS has particular trade-offs and challenges. A large number of simulations are required to optimize the beam's path, power, and time-per-position while accounting for tumor geometry and location, normal tissue constraints, and changes in tissue parameters due to treatment; consequently numerical techniques that can accurately and rapidly model ultrasound beam propagation are required. Simplifying assumptions (like use of homogeneous models and acoustic parameters from table-value estimates in simulations) are frequently used to speed up calculation times but affect the accuracy of predictions, while techniques using realistic models have been traditionally considerably slower. The numerical beam propagation techniques developed in this work (ERFA, Ring-Bessel and HAS) allow for rapid (~5 s) and accurate prediction of ultrasound power deposition patterns inside complex inhomogeneous tissue models (1-mm isotropic resolution) inside the tissue volume of interest (10x10x10 $cm^3$) for MRgFUS treatments.

## 8.1. Beam simulation techniques for MRgFUS

The HAS technique is an extension of the traditional angular spectrum method and models linear beam propagation in complex inhomogeneous models by taking into account the effect of reflection, refraction and attenuation of the beam. In validation studies the technique was shown to be rapid and accurate, with a decrease in calculation time of more than two orders of magnitude compared to the FDTD technique, while giving essentially the same pressure pattern (normalized root mean square difference of 1.3% over the entire 3D volume). The technique's ability to rapidly model beam propagation in realistic models was demonstrated by using a segmented breast model from a patient; the total calculation time for prediction of the pressure and SAR pattern was 5 s. The HAS technique assumes steady state and linear propagation conditions and only models first order reflections. When modeling beam propagation through highly reflecting interfaces (for e.g. with bone) multiple reflections should be calculated. Since the HAS technique requires the pressure pattern to be specified on a plane, two techniques, the ERFA technique and the Ring-Bessel technique, were developed. These techniques calculate beam propagation in homogeneous medium, such as water, from a curved transducer surface to an intermediate plane; subsequent propagation of the ultrasound beam in complex inhomogeneous geometries use the HAS technique. In cases where the element response array can be precalculated, using the ERFA technique speeds up run-time calculation times by as much as 135 times compared to the commonly used R-S technique. In cases where the fixed ERFA parameters (transducer specifications, spatial sampling-frequency of the source and distance of the transducer from the intermediate plane) need to be changed frequently and hence precalculation of the EFRA

is not appropriate, the R-B technique results in reducing calculation times by 30 times compared to the R-S technique.

The speed of the numerical beam propagation techniques developed here allows for complex treatment planning decisions to be made in patient-specific models. Using segmented tissue models of tumor shape, size and location, these techniques have been combined with thermal simulations to optimize the treatment path. Further, these techniques have been used conjunction with thermal simulations to optimize transducer design parameters for particular clinical applications and to explore the trade-offs of transducer design parameters on near-filed heating in MRgFUS.

## 8.2. Subject-specific acoustic tissue parameters in MRgFUS

A technique that uses the fast beam propagation techniques developed previously in an optimization routine with the traditional rate-of-temperature-increase technique and MR-temperature imaging (MRTI) was presented to noninvasively estimate subject-specific tissue acoustic properties. The tissue properties estimated using the iterative parameter estimation technique were validated by comparing to two independent techniques: the through-transmission technique for homogeneous phantoms and an inverse-scattering tomography technique for inhomogeneous *ex-vivo* porcine muscle. The parameter estimation technique resulted in attenuation coefficient values within 5% of those determined using the independent techniques. The inverse parameter estimation technique was used in *in-vivo* rabbit thigh to measure change in attenuation coefficient of tissue with MRgFUS treatment and a linear dependence of attenuation change with $\log_{10}$ of thermal dose was found; the slope of the attenuation change found using the

noninvasive technique *in-vivo* corresponded well with the slope determined using invasive thermocouples in *in-vitro* results presented in previous studies.

## 8.3. Future work

### 8.3.1. Modeling non-linear beam propagation

All techniques for beam simulation in this work assume linear propagation conditions. At high intensity levels, non-linear effects of the beam propagation cause waveform distortion resulting in production of higher harmonics. These higher harmonics are rapidly absorbed, resulting in higher power deposition in the region. In order to model this effect, the HAS technique can be modified to propagate higher spatial frequencies at each sub-step.

### 8.3.2. Modeling multiple reflections

The HAS technique calculates the effect of reflection by calculating the energy reflected at each interface and back propagating this reflected wave. Multiple reflections are not presently implemented. In cases where beam propagation is modeled in tissues containing interfaces with a high acoustic mismatch (e.g., bone-tissue interface) multiple reflections should be considered.

### 8.3.3. Modeling absorption and scattering in the media

The loss of power as the ultrasound beam travels deeper in the tissue is due to attenuation of the beam; this term combines two effects of the beam propagation:

absorption of the beam resulting in SAR deposition, and scattering of the beam due to inhomogeneities in the medium of propagation. Separation of these two effects in the HAS technique will be valuable when using tissue samples with high scatter.

### 8.3.4. Measuring time-course of attenuation change

Applying repeated interrogation pulses immediately after the treatment and obtaining the $SAR_{exp}$ information from these pulses would allow for information on the time course of the change in attenuation with treatment. Further, repeated interrogation pulses can be applied with interspersed cooling to measure whether the changes in tissue attenuation values are irreversible.

### 8.3.5. Changes in attenuation with treatment of different tissue types

The noninvasive technique can be applied to different *in-vivo* tissue types to examine the change in attenuation coefficient with treatment in different tissue types.

The noninvasive technique can be used to measure the efficiency of the transducer by using interrogation pulses in a sample with known attenuation coefficient, speed of sound and specific heat.

# APPENDIX

This section contains the MATLAB code used to derive the results described in this dissertation. Each program begins with the function call specification, followed by comments and the code itself.

```
function pp=RSfieldsB1FF(fMHz,Pr,Dv,Dh,imax,kmax,R,d,c0,rho0,Lv,Lh,Cv,Ch,h,v,z,…
lmax,mmax, activearea,relem, ElemLoc,FF)
%RSfieldsB1FF Code for implementation of the Rayleigh-Sommerfeld equation for
%phased array transducer with fudge factor. 3D program to calculate the Rayleigh-
%Sommerfeld integral for a SPHERICALLY curved transducer of radius of curvature R
%and overall dimensions of Dv (vertical) x Dh (horizontal) as measured along an arc. The
%input pt(i,k) is the pressure pattern on the source transducer as function of angles theta
%(i=elevation  index) and phi (k=azimuth index). Output pp(l,m) is the pressure on a
%secondary plane as a function of Cartesian coordinates (l=vert index, m=horiz index), as
%calculated on this plane, a distance d away from the furthest point of the transducer
%curved face.  The secondary plane has size Lv (vertical) x Lh (horizontal), which is
%almost always the same size and matched with the face of the Modl into which the
%pressure propagates. The center of the transducer axis is located distances Cv (vert) and
%Ch (horiz) from origin of the secondary plane. Thus the center of this plane is offset from
%the center of the transducer axis by amounts Ov and Oh. The medium between the
%transducer and secondary plane has speed of sound c0.  pp(l,m) then becomes the source
%for the Hybrid Angular Spectrum method for finding the subsequent pressure in an
%inhomogeneous region defined by the Modl, and is stored as a binary .mat file with a
%name such as PP_test.mat. The desired focal point of the spherical transducer is
%determined by the phasing of the pressure pattern on the transducer (via electronic
%focusing and steering), as given by the function 'SteeringPhases1'. The focal point is
%located a distance v, h, z away from the geometrical focus of the transducer (at R), and
%therefore at a distance Fv,Fh,Fz (vert, horiz, depth) away from the origin of the
%secondary plane (aligned with Modl). Note: In this program, x is in the vertical direction
%and y is in the horizontal direction, which often is backwards from other programs that
%generate models and view results.  But this orientation of x and y is transparent to other
```

```
%programs since the input and output are put in terms of 'vertical' and 'horizontal'. Calls
%function 'SteeringPhases1' and uses parameter file such as 'paramRS_test'. This version
B %is modified to use a 'for' loop for yp increments, thus avoiding all 4D arrays (which do
%implicit integration--see RSfieldsA program). Avoiding 4D arrays allows larger values
%for imax, kmax, lmax and mmax in the available memory, but is slower.


f=(fMHz/FF)*1e6; % convert to Hz.
Ov=(Lv/2)-Cv; % convert location of center of transducer axis wrt origin of secondary
        % plane (Modl) to offsets wrt center of secondary plane.
Oh=(Lh/2)-Ch;
 i=1:imax; k=1:kmax; l=1:lmax; m=1:mmax; % set up indices.
dth=Dv/(R*imax); dphi=Dh/(R*kmax); % incremental size of source angle (in radians).
dxp=Lv/lmax ;
dyp=Lh/mmax; % incremental size of steps in secondary plane (in m)
  th=dth*(i-round(imax/2)); % angle row vector, centered; imax and kmax should be
        % odd for symmetry
phi=dphi*(k-round(kmax/2)); % angle row vector, centered
thmesh=repmat(th',1,kmax);  % imax x kmax matrix of theta values, 'meshgrid' style
phimesh=repmat(phi,imax,1); % imax x kmax matrix of phi values, 'meshgrid' style
  Zm=rho0*c0; Arc=min(Dv,Dh);% impedance of medium; diameter along arc of a
  circular
        % transducer
XducerArea=2*pi*R*R*(1-cos(Arc/(2*R))); % area of spherical segment
ptunif=sqrt(Zm*Pr/XducerArea);  % pressure consistent with radiated power, if uniform
 pabs=(ptunif/sqrt(activearea))*ones(imax,kmax); % increase pressure to account for
        % active area
pt=zeros(imax,kmax); % start with blank final pressure field
thvect=ElemLoc(:,1); phivect=ElemLoc(:,2); %column vectors of theta and phi
ang=SteeringPhases1(v,h,z,R,thvect,phivect,f,c0); % column vector of phases
numelem=size(thvect,1);
for g=1:numelem % cycle through elements
   pelem=pabs.*cos(ang(g))+j*pabs.*sin(ang(g)); % element g has uniform pressure &
        % phase
   distfromelem=R*acos((cos(thvect(g))*cos(thmesh)).*cos(phivect(g)-phimesh)...
```

```
      +sin(thvect(g))*sin(thmesh));   % great circle distance from center of element g.
   indelem=find(distfromelem > relem);
   xelem=find(distfromelem<=relem);
   pelem(indelem) = 0; % set pressure to zero in areas outside of element
   pt=pt+pelem; % add element pressure to overall pressure field
   end
ss5=R*(cos(thmesh).*sin(phimesh)); % 2D matrix: imax x kmax
s=repmat(ss5,[1,1,lmax]);% now 3D array
yp=dyp*(m-round(mmax/2))+Oh;% vector (offset by Oh)
aa5=R*(cos(thmesh).*cos(phimesh));
a=repmat(aa5,[1,1,lmax]);% 3D array: imax x kmax x lmax
b=R-a;
tt= R*sin(thmesh);
t=repmat(tt,[1,1,lmax]); % 3D array
xxp(1,1,:)=dxp*(l-round(lmax/2))+Ov;    % turn into 'page' vector, lmax pages long
(xp=repmat(xxp,[imax,kmax,1]);% 3D array
term1=(t-xp).^2;
term3=(d-b).^2;
cth=cos(thmesh);% cos theta matrix for spherical integration
ppc=pt.*cth;  % pt is transducer source matrix (must be imax x kmax)
pc=repmat(ppc,[1,1,lmax]);% product of pressure and cos theta now 3D array
kk=2*pi*f/c0;
ppi=zeros(kmax,lmax,mmax); % pre-allocate storage for ppi
for mi=1:mmax
   r=sqrt(term1 + term3 + (s-yp(mi)).^2);  % r is 3D array for each value of yp
   ppi(:,:,mi)=(f*R*R*dth*dphi/c0)*sum(pc.*exp(j*(-kk*r + (pi/2)))./r); % Rayleigh-
     % Sommerfeld integral over  xp only here, for one value of yp
end
pp=shiftdim(sum(ppi)); % pp is secondary plane pressure, an lmax x mmax matrix
```

```
function Q = HASfields(pp,fMHz,Lv,Lh,Lz,Modl,rho0,c0,FF,Ax,Cx)

 %HASfields: This is a modified version of the HASfielfs1 program. This is a function that
%will be called by the program MainLoop. The input of this function is pp( which is
%previously calculated by the function RSfieldsBf). The outputs of this function are pout
%and Q. The function uses a parameter file called paramHAS_loop1.The function loads a
%Modl called Modl_loop1.Function using Hybrid Angular Spectrum approach for
%calculating propagation of an ultrasound beam through an inhomogeneous medium.
%Input pp(l,m) is the pressure on the input plane as function of Cartesian coords   (l = vert
%index, m = horiz index). Output pout(l,m,n) is the 3D pressure pattern throughout the
%lmax, mmax, nmax extent of the model 'Modl' (lmax = vert extent, mmax = horiz extent,
%nmax = extent in propagation direction). dv, dh, and dz are vertical, horizontal and axial
%increments of model space.

c(1)=1.5e3;a(1)=0;rho(1)=1e3; % 1 is water

[lmax,mmax,nmax] = size(Modl);  % The size of the model (lmax,mmax,nmax) sets the
% size of  the simulation space.  lmax is vertical; mmax is horizontal.  lmax and mmax are
% therefore also the size of the secondary plane input matrix pp.  Note: lmax and mmax
% should be ODD numbers to keep fftshift symmetrical with the dc term at exact center of
% spectrum.

dv=Lv/lmax; % dv,dh,dz = vert, horiz, longitudinal element size in [m]

dh=Lh/mmax;

dz=Lz/nmax;

f=(fMHz/FF)*1e6;   % convert to Hz

 A=zeros(size(Modl));  % initialize 3D angular spectrum array

b=zeros(size(Modl));  % initialize 3D propagation constant array

pout=zeros(size(Modl));  % initialize 3D resultant pressure array

Q=zeros(size(Modl));  % initialize 3D Q array

 pp=conj(pp);    % needed because exponent sign is opposite in R-S and Ang
            % Spectrum assumptions.

sizepp=size(pp);   % pp is the source pressure in the secondary source plane

if (lmax~=sizepp(1)) | (mmax~=sizepp(2))
   error ('Initial pressure field dimensions do not match model dimensions. Correct and try
again.')

end

pout(:,:,1)=pp;

 bprime(1)=2*pi*f/c0; % assume layer 1 is water, so average bprime = omega/c0

A(:,:,1)=fftshift(fft2(pout(:,:,1))); % wraparound fft
```

```
  % Since dfx=1/xmax=1/(lmax*dv), then transverse increments of A--in units of alpha and
        % beta--are  dalphadl=2*pi/(lmax*dv*bprime(1)), and
        % dbetadm=2*pi/(mmax*dh*bprime(1))
        % Note that x is vertical (lmax, dv direction) in this program,
        % and y is horizontal (mmax, dh)
dalphadl=2*pi/(lmax*dv*bprime(1));
dbetadm=2*pi/(mmax*dh*bprime(1));
alphaindex=(1:lmax)';  % note transpose to put in column vector form
alpha=(alphaindex-ceil(lmax/2))*dalphadl;
alphasq=alpha.*alpha;
alphasqmat=repmat(alphasq,1,mmax);
betaindex=(1:mmax);
beta=(betaindex-ceil(mmax/2))*dbetadm;
betasq=beta.*beta;
betasqmat=repmat(betasq,lmax,1);
Amag=abs(A(:,:,1));
Denom=sum(sum(Amag))*dalphadl*dbetadm; % discrete integration
Numer=sum(sum((alphasqmat+betasqmat).*Amag))*dalphadl*dbetadm; % discrete integration
M2(1)=Numer/Denom;  % 2nd moment
%------------ Start of increment in n (z propagation direction) -------------
for n=2:nmax
    cmat=zeros(size(Modl(:,:,n)));
   attmat=zeros(size(Modl(:,:,n)));
   rhomat=zeros(size(Modl(:,:,n)));
for g=1:max(max(Modl(:,:,n))) % fill in speed of sound and attenuation matrices with
        % actual values
      ind=find(Modl(:,:,n)==g);
      cmat(ind)=c(g);
      attmat(ind)=a(g);
      rhomat(ind)=rho(g);
   end
   if min(min(cmat))==0; error ('Some speed of sound values are zero.'); end
    attmat=attmat*1e-4*f; % convert units of a from [1/cm*MHz] to [1/m]
```

```
b(:,:,n)=2*pi*f./cmat;
bprime(n)=mean(mean(b(:,:,n)));% propagation constant averaged over entire n plane
dkplus=b(:,:,n)-bprime(n) + j*attmat;% variation of prop. constant from average
        % plus attenuation
dkminus=b(:,:,n)-bprime(n) - j*attmat;% variation of prop. constant from average
        % minus attenuation
pprime=pout(:,:,n-1).*(exp(j*dkplus*dz).*(1-(j*dkminus*dz*M2(n-1)/2))); % Eq (6)
Aprime=fftshift(fft2(pprime)); % complex Eq (8)
dalphadl=2*pi/(lmax*dv*bprime(n));
dbetadm=2*pi/(mmax*dh*bprime(n));
alphaindex=(1:lmax)'; % note transpose to put in column vector form
alpha=(alphaindex-ceil(lmax/2))*dalphadl;
alphasq=alpha.*alpha;
alphasqmat=repmat(alphasq,1,mmax);
betaindex=(1:mmax);
beta=(betaindex-ceil(mmax/2))*dbetadm;
betasq=beta.*beta;
betasqmat=repmat(betasq,lmax,1);
 A(:,:,n)=Aprime.*exp(j*bprime(n)*dz*sqrt(1-alphasqmat-betasqmat));  % Eq (9)
Amag=abs(A(:,:,n));
Denom=sum(sum(Amag))*dalphadl*dbetadm;  % discrete integration.
Numer=sum(sum((alphasqmat+betasqmat).*Amag))*dalphadl*dbetadm;  % discrete
        % integration
M2(n)=Numer/Denom;  % 2nd moment
 pmat=ifft2(ifftshift(A(:,:,n))); % Eq (10)
pout(:,:,n)=pmat;
Q(:,:,n)=abs(attmat.*pmat.*conj(pmat)./(cmat.*rhomat)); % some extremely small imag
        % values not valid, so abs
end
```

```
function diffQ= AttenSpeedParam(v)

%AttenuationSpeedParam:  Function that calculates the speed of sound and attenuation
%values minimizing the error in one row of Q using a predefined value of power and FF in
%a slice. This code assumes that the number of tissue types (different from water) in the
%model is one (tissue type 2, since 1 is water), when dealing with changing tissue
%properties, the code will have to be extended to optimize over the attenuation of all tissue
%types. Efficiency, d and Fudge Factor are inputs, one way of determining these terms is
%using a phantom with known properties and optimizing over these values. Different error
%measurement terms can be used, mean squared diff, sum squared difference. The region
%where the mean difference is calculated over is user and application dependent, eg, in
%phantoms we have good SNR and can normalize over the entire focal zone, but in-vitro
%we might want to only minimize over the central slice. This code is shown without using
%a Mask when using the mask (which makes sure the difference is calculated over only
%the noise free voxels) the difference term shown in line 50-51 can be used. Also the
%Mask should be truncated the same way the Q_rel was truncated as in line-43.


load Q_60W; % loading the experimental SAR pattern

speed1=v(2);

atten1=v(1);

d=.084;  % distance of the transducer from the model (m)

FF=1;     % factor to be multiplied to the beam to broaden the beam, eg 1

power=60; % acoustic power input into the beam simulation

Modl=ones(31,19,45); % size of Model

ParamRSf; % load parameter file for RS calculation

ParamHASf; % load parameter file for HAS calculation

ElementDAnglesSiemens; % element location file for Transducer

pp=RSfieldsB1FFUrvif(fMHz,Pr,Dv,Dh,imax,kmax,R,d,c0,rho0,Lv,Lh,Cv,Ch,h,v,z,lmax,
mmax,activearea,relem,ElemLoc,FF);

[Q]=HASfieldsReflectionF(pp,fMHz,Lv,Lh,Lz,Modl,rho0,c0,FF,atten1,speed1);

Q_Urvi=Convert_Q(Q); % convert simulation Q to exp coordinates

Q_rel1=Q_rel(12:56,20:50,:); % truncate experimental Q pattern when using Mask

        %truncate the Mask in the same way.

clear Q_rel; % clear to save memory

Q_rel=Q_rel1; % check units, it should be W/m3

Q_sim=Q_sim*efficiency; % multiplied by transducer efficiency

Q_simN=Q_sim/max(max(max(abs(Q_sim)))); % normalised error calculation
```

```
Q_relN=Q_rel/max(max(max(abs(Q_rel))));
diffQ1=Q_rel(:,:,3)-Q_sim(:,:,3); % calculating difference
% diffQ1=Q_relN(:,:,3)-Q_simN(:,:,3); % normalized error
 sqdiffQ=diffQ1.^2; % Squared difference
ssqdiffQ=squeeze(sum(sum(sum(sqdiffQ)))); % Sum squared difference
```

```
clear all;clc;
ParamRingCases1;
%RingBesselSolid:Code to calculate the pressure pattern on an intermediate plane using
%ring theory for a SOLID spherical transducer. The program  calls a steering function
%(SteeringPhasesRing3), so the beam can be steered. It generates the complex pressure
%pattern pp on an intermediate plane a distance d  from the back of the transducer, which
%is the first plane of the HAS Modl (and which is a distance (d-Rc) from the geometrical
%focal plane). This version 5 reads in an arbitrary number of rings in the transducer and
%keeps the spacing around the circumference close to the spacing dE between rings.  In
%the frequency domain, the rho spacing drho matches dfx or dfy, which in turn are set by
%the overall size of the final pp pattern (including offsets).  The pp space pattern is carved
%out of the larger pp2 pattern to match the first plane of the Modl. This version uses the
%much faster interpolation routine ringNNinterp to interpolate from polar to Cartesian
%coordinates.
Lambda=c0/f;
rhomax=min([0.995*(1/Lambda), 1/(2*dh), 1/(2*dv)]); % closeness to 1/Lambda
        % determined empirically
xoffs=ceil(abs(offsetx)/dh)*dh; % these values are a little larger than offsetx, but they
        % make sure that dv and dh in g space pattern are exact after ifft of G
yoffs=ceil(abs(offsety)/dv)*dv;
        %xoffs=0;yoffs=0;
dfx=1/(Lx+2*xoffs); dfy=1/(Ly+2*yoffs); % set by overall size of pp pattern in space.
Nfx=round((1/dh)/dfx); % should always be an odd integer if Nx is odd integer and dfx correct
Nfy=round((1/dv)/dfy);
        % if 2*round(Nfx/2)==Nfx || 2*round(Nfy/2)==Nfy;
drhomatch=min(dfx,dfy); dphimatch=drhomatch/rhomax; %  approx match to dfx or dfy,
        % whichever is smaller
Nrho=round(rhomax/drhomatch); % drho will be close to drhomatch.
Nphi=round(2*pi/dphimatch); % note that since Nphi is constant, freq samples get close
% together near origin, but this allows a matrix into bessel function argument for speed
Nrho=201;Nphi=501;
        %rho=linspace(rhomax/Nrho,rhomax,Nrho);
        %  legacy rho with no dc since slows down griddata
rho=linspace(0,rhomax,Nrho); % radius values in radial spatial frequency, with dc
phi=linspace(0,2*pi*(1-1/Nphi),Nphi); % angle values in spatial frequency
        % don't repeat 0,2pi
```

```
Sum=zeros(Nphi,Nrho);  % initialize Sum
dq=asin(Rimax/Rc)/Nrings; % increment in angle to rings
dE=Rc*dq;   % arc width of each ring

hwb=waitbar(0,'Evaluating RING calculations...');
for i=1:Nrings
   qm=(i+0.5)*dq;  % angle from axis to ring center (infinitesimally thin ring)
   Rm=Rc*sin(qm);  % radius of ring i.
   zc=Rc*cos(qm);  % distance of ring from the geometrical focal point
   zi=d1-Rc+zc; % distance from ring to the intermediate plane
         % (d is dist from xducer to model)
   p=2*round((2*pi*Rm/dE+1)*.5)-1; % odd number of circ. samples in ring
         %spacing close to dE
   dth=2*pi/p; % increment in theta angle in ring plane
   q=ceil(-p/2):floor(p/2);    % index symmetrical around zero
   th=linspace(0,2*pi-dth,p);  % angle to circ. samples
   ang=SteeringPhasesRing3(h,v,z,Rc,Rm,zc,f,c0,th);
         % get phases for steering from solid xducer
   h1=Rc*(cos(qm-dq/2)-cos(qm+dq/2));  % 'height' of spherical segment
   dSm=(2*pi*Rc*h1)/p;
         % surface area around each point, to equalize contribution from each point
   Vc=(dSm*Vabs).*(cos(ang)+j*sin(ang)); % complex velocity of transducer points
   Cni=(1/p)*fft(Vc);  % Fourier transform in theta
   Cni=fftshift(Cni);
   E1=Rm*(j.^q).*Cni;  % see ring theory for coefficient definitions
   E1f=repmat(E1',1,size(phi,2));
   expon=q'*phi;   % shortcut meshgrid of exponent
   E2=cos(expon) + j*sin(expon);   % same as exp(j*q*phi), % but quicker
   q1=q(find(q==0):end);   % non-negative q's
   q2=q1(2:end);          % positive q's
   [q1m,rhom]=meshgrid(q1,rho);    % row, column order to give fastest bessel calc.
   rhom1=2*pi*Rm*rhom;
   J=besselj(q1m,rhom1);   % bessel functions of non-negative order
```

```
    JJ=J(:,2:end);
    aa=(-1).^q2;
    aaf=repmat(aa,size(rho,2),1);
    JJa=JJ.*aaf;
    JJb=fliplr(JJa);    % calculate negative bessel functions for negative orders.
    Jc=[JJb,J];     % combine.
    V=Jc*(E1f.*E2);
    Vi=V';
    s=j*2*pi.*sqrt(((1/Lambda)*(1/Lambda))-(rho.*rho));
    SP1=exp(s*zi)./s;   % spectral propagator to zi, velocity -> pressure.
    SP=repmat(SP1,size(phi,2),1);
    Vout=Vi.*SP;    % propagate to intermediate plane at zi.
    Sum=Sum+Vout;   % add up angular spectrum of all rings.
    waitbar(i/Nrings)
end
close(hwb); pause(.1);
fx=cos(phi')*rho;   % convert to array in rectangular coordinates
fy=sin(phi')*rho;
fxmax=Nx/(2*Lx);
fymax=Ny/(2*Ly);
p1=linspace(-fxmax,fxmax,Nx);   % maximum rect. spatial freqs. can be larger
q1=linspace(-fymax,fymax,Ny);   %  than rhomax
w=griddata(fx,fy,Sum,p1,q1');
w(find(isnan(w)))=0;    %  zero out all freqs. outside circular rhomax
[fxm,fym,w]=griddata(fx,fy,Sum,p1,q1','nearest'); % alternate griddata, faster?
rads=sqrt(fxm.*fxm + fym.*fym);
w(find(rads>rhomax))=0;   %   zero out all freqs. outside circular rhomax
pp2=fftshift(ifft2(ifftshift(w)));
```

```
function [Q_rel, Mask]=PolyFit2D(temps,TimeStep,Baselines,NosPts)

%PolyFit2dD: Function to find the SAR when given 4D temps. Right now finds SAR only
%in a plane, should be extended to find the SAR in all voxels. A Mask removes noise
%voxels and does not calculate SAR over these points. Temps should be smaller than the
%exp temps because we do not want to calculate over the transducer for example.
%INPUT VARIABLES
%temps: experimental temps
%TimeStep: MRI temperature slice time step in seconds.
%Baseline: The number of baseline measurements taken, this will be used to create a mask
%of the noisy voxels.
%TempFluc: The temperature fluctuation that is acceptable for the case, eg smaller for
%phantoms and bigger for in-vivo studies.
%NosPts: The number of points you want to use to calculate the initial slope, eg if you
%want to use 3 pts to fir the line set NosPts to 2.
%OUTPUT VARIABLES
%Q_rel: The SAR pattern calculated in the region of interest.
%Mask: A Mask is created with noisy voxels =0 and other =1. This mask will be used in
%the optimization to make sure the noisy voxels are not used to calculate the summed
%difference. NOTE: To make sure the data is not affected by human bias, the Mask should
%be calculated separately before Q_rel is calculated.

sizet=size(temps); slice=2;

TempFluc=2; %temp fuctuation on the basis of which noisy voxels are set

D=((abs(double(squeeze(temps(:,:,slice,1:Baselines)))))>TempFluc);

D1=squeeze(sum(D,3));

Ay=(D1==0);

Mask(:,:)=Ay;

% Mask(80:128,:)=0;

Q_rel1=zeros(sizet(1),sizet(2));

time=0:TimeStep:(TimeStep*NosPts);

for hh=1:sizet(1)
   for vv=1:sizet(2)
      temp=polyfit(time,(squeeze(temps(hh,vv,slice,Baselines:(Baselines+NosPts)))'),1);
      Q_rel1(hh,vv)=temp(1);
   end
end

Q_rel=Mask.*Q_rel1*4186*1e3;
```

## REFERENCES


[1] K. Hynynen, N. McDannold, G. Clement, F.A. Jolesz, E. Zadicario, R. Killiany, T. Moore, and D. Rosen, "Pre-clinical testing of a phased array ultrasound system for MRI-guided noninvasive surgery of the brain--a primate study," Eur J Radiol, vol. 59, 2006, pp. 149-56.

[2] J. Hindley, W.M. Gedroyc, L. Regan, E. Stewart, C. Tempany, K. Hynnen, N. Macdanold, Y. Inbar, Y. Itzchak, and J. Rabinovici, "MRI guidance of focused ultrasound therapy of uterine fibroids: early results," American Journal of Roentgenology, vol. 183, 2004, p. 1713.

[3] K. Hynynen, O. Pomeroy, D.N. Smith, P.E. Huber, N.J. McDannold, J. Kettenbach, J. Baum, S. Singer, and F.A. Jolesz, "MR imaging-guided focused ultrasound surgery of fibroadenomas in the breast: a feasibility study," Radiology, vol. 219, 2001, p. 176.

[4] P.E. Huber, J.W. Jenne, R. Rastert, I. Simiantonakis, H.P. Sinn, H.J. Strittmatter, D. von Fournier, M.F. Wannenmacher, and J. Debus, "A new noninvasive approach in breast cancer therapy using magnetic resonance imaging-guided focused ultrasound surgery," Cancer research, vol. 61, 2001, p. 8441.

[5] F.A. Jolesz and N. McDannold, "Current status and future potential of MRI-guided focused ultrasound surgery," Journal of Magnetic Resonance Imaging, vol. 27, 2008, pp. 391-399.

[6] C.J. Diederich, R.J. Stafford, W.H. Nau, E.C. Burdette, R.E. Price, and J.D. Hazle, "Transurethral ultrasound applicators with directional heating patterns for prostate thermal therapy: in vivo evaluation using magnetic resonance thermometry," Medical Physics, vol. 31, 2004, p. 405.

[7] M.E. Anderson, M.S. McKeag, and G.E. Trahey, "The impact of sound speed errors on medical ultrasound imaging," The Journal of the Acoustical Society of America, vol. 107, 2000, pp. 3540-3548.

[8] V. Amin, R. Roberts, T. Long, R.B. Thompson, and T. Ryken, "A study of effects of tissue inhomogeneity on hifu beam," AIP Conference Proceedings, vol. 829, 2006, pp. 201-205.

[9] X. Fan and K. Hynynen, "The effect of wave reflection and refraction at soft tissue interfaces during ultrasound hyperthermia treatments," The Journal of the Acoustical Society of America, vol. 91, 1992, pp. 1727-1736.

[10] L.M. Hinkelman, T.D. Mast, L.A. Metlay, and R.C. Waag, "The effect of abdominal wall morphology on ultrasonic pulse distortion. Part I. Measurements," The Journal of the Acoustical Society of America, vol. 104, 1998, pp. 3635-3649.

[11] T.D. Mast, L.M. Hinkelman, M.J. Orr, V.W. Sparrow, and R.C. Waag, "Simulation of ultrasonic pulse propagation through the abdominal wall," The Journal of the Acoustical Society of America, vol. 102, 1997, pp. 1177-1190.

[12] R.J. McGough, M.L. Kessler, E.S. Ebbini, and C.A. Cain, "Treatment planning for hyperthermia with ultrasound phased arrays," Ultrasonics, Ferroelectrics and Frequency Control, IEEE Transactions on, vol. 43, 1996, pp. 1074-1084.

[13] M.R. Bailey, V.A. Khokhlova, O.A. Sapozhnikov, S.G. Kargl, and L.A. Crum, "Physical mechanisms of the therapeutic effect of ultrasound (a review)," Acoustical Physics, vol. 49, 2003, pp. 369-388.

[14] C.F. Andrew, "ICRU Report 61: Providing reference data for tissue properties," The Journal of the Acoustical Society of America, vol. 105, 1999, p. 1324.

[15] W. Yao, W. Yao, J.W. Hunt, F.S. Foster, and D.B. Plewes, "Tissue ultrasound absorption measurement with MRI calorimetry," Ultrasonics, Ferroelectrics and Frequency Control, IEEE Transactions on, vol. 46, 1999, pp. 1192-1200.

[16] P.D. Tyreus and C. Diederich, "Two-dimensional acoustic attenuation mapping of high-temperature interstitial ultrasound lesions," Physics in medicine and biology, vol. 49, 2004, pp. 533-546.

[17] C.A. Damianou, N.T. Sanghvi, F.J. Fry, and R. Maass-Moreno, "Dependence of ultrasonic attenuation and absorption in dog soft tissues on temperature and thermal dose," The Journal of the Acoustical Society of America, vol. 102, 1997, pp. 628-634.

[18] M.R. Gertner, B.C. Wilson, and M.D. Sherar, "Ultrasound properties of liver tissue during heating," Ultrasound in medicine & biology, vol. 23, 1997, pp. 1395-403.

[19] J. Rayleigh, The theory of sound, 1945.

[20] R.J. Zemp, J. Tavakkoli, and R.S.C. Cobbold, "Modeling of nonlinear ultrasound propagation in tissue from array transducers," The Journal of the Acoustical Society of America, vol. 113, 2003, pp. 139-152.

[21] K.B. Ocheltree and L.A. Frizzel, “Sound field calculation for rectangular sources,” IEEE Trans. Ultrason. Ferroelect. Freq. Contr., vol. 36, 1989, pp. 242-248.

[22] C. Lee and P.J. Benkeser, “Computationally efficient sound field calculations for a circular array transducer,” IEEE Transactions on Ultrasonics, Ferroelectrics and Frequency Control,, vol. 39, 1992, pp. 43-47.

[23] J.A. Jensen and N.B. Svendsen, “Calculation of pressure fields from arbitrarily shaped, apodized, and excited ultrasound transducers,” IEEE Transactions on Ultrasonics, Ferroelectrics and Frequency Control, vol. 39, 1992, pp. 262-267.

[24] G.R. Harris, “Review of transient field theory for a baffled planar piston,” The Journal of the Acoustical Society of America, vol. 70, 1981, pp. 10-20.

[25] P. Stepanishen, M. Forbes, and S. Letcher, “The relationship between the impulse response and angular spectrum methods to evaluate acoustic transient fields,” The Journal of the Acoustical Society of America, vol. 90, 1991, pp. 2794-2798.

[26] P.T. Christopher and K.J. Parker, “New approaches to the linear propagation of acoustic fields,” The Journal of the Acoustical Society of America, vol. 90, 1991, pp. 507-521.

[27] J.A. Ratcliffe, “Some aspects of diffraction theory and their application to the ionosphere,” Reports on Progress in Physics, vol. 19, 1956, pp. 188-267.

[28] J. Goodman, Introduction to Fourier Optics, Englewood, CO: Roberts & Company, 2005.

[29] P. Wu, R. Kazys, and T. Stepinski, “Optimal selection of parameters for the angular spectrum approach to numerically evaluate acoustic fields,” The Journal of the Acoustical Society of America, vol. 101, 1997, pp. 125-134.

[30] W. Ping, K. Rymantas, and S. Tadeusz, “Analysis of the numerically implemented angular spectrum approach based on the evaluation of two-dimensional acoustic fields. Part I. Errors due to the discrete Fourier transform and discretization,” The Journal of the Acoustical Society of America, vol. 99, 1996, pp. 1339-1348.

[31] X. Zeng and R. McGough, “Multiplanar angular spectrum approach for fast simulations of ultrasound therapy arrays,” The Journal of the Acoustical Society of America, vol. 118, 2005, pp. 1911-1911.

[32] C. Vecchio, M. Schafer, and P. Lewin, “Prediction of ultrasonic field propagation through layered media using the extended angular spectrum method,” Ultrasound Med Biol, vol. 20, 1994, pp. 611-622.

[33] M.E. Schafer, P.A. Lewin, and J.M. Reid, “Propagation through inhomogeneous media using the angular spectrum method,” IEEE Ultrasonics Symposium, 1987, pp. 943-946.

[34] D. Belgroune, J.F. de Belleval, and H. Djelouah, "Modeling of the ultrasonic field by the angular spectrum method in presence of interface," Ultrasonics, vol. 40, 2002, pp. 297-302.

[35] F.P. Curra, P.D. Mourad, V.A. Khokhlova, R.O. Cleveland, and L.A. Crum, "Numerical simulations of heating patterns and tissue temperature response due to high-intensity focused ultrasound," Ultrasonics, Ferroelectrics and Frequency Control, IEEE Transactions on, vol. 47, 2000, pp. 1077-1089.

[36] W.F. Ames, Numerical methods for partial differential equations, New York: Academic Press, 1989.

[37] M. Cizek and J. Rozman, "Acoustic wave equation simulation using FDTD," Radioelektronika, 2007. 17th International Conference, 2007, pp. 1-4.

[38] M. Cizek and J. Rozman, "Acoustic wave equation simulation using FDTD," 17th International Conference Radioelektronika., 2007, pp. 1-4.

[39] S.A. Goss, R.L. Johnston, and F. Dunn, "Comprehensive compilation of empirical ultrasonic properties of mammalian tissues," The Journal of the Acoustical Society of America, vol. 64, 1978, pp. 423-457.

[40] S.A. Goss, J.W. Cobb, and L.A. Frizzell, "Effect of beam width and thermocouple size on the measurement of ultrasonic absorption using the thermoelectric technique," Ultrasonics Symposium, 1977, pp. 206-211.

[41] Y. Hui, Y. Hui, R. Griffin, and E.S. Ebbini, Noninvasive localized ultrasonic measurement of tissue properties, 2004.

[42] W. Fry and F. Dunn, "Ultrasound: analysis and experimental methods in biological research," Physical Techniques in Biological Research, 1962.

[43] N. Bush, I.H. Rivens, G. Ter Haar, and J. Bamber, "Acoustic properties of lesions generated with an ultrasound therapy system," Ultrasound Med Biol, vol. 19, 1993, pp. 789-801.

[44] V. Zderic, A. Keshavarzi, M.A. Andrew, S. Vaezy, and R.W. Martin, "Attenuation of porcine tissues in vivo after high-intensity ultrasound treatment," Ultrasound in medicine & biology, vol. 30, 2004, pp. 61-66.

[45] A.D. Christakis, T.S. Narendra, J.F. Francis, and M. Roberto, "Dependence of ultrasonic attenuation and absorption in dog soft tissues on temperature and thermal dose," The Journal of the Acoustical Society of America, vol. 102, 1997, pp. 628-634.

[46] A.E. Worthington and M.D. Sherar, "Changes in ultrasound properties of porcine kidney tissue during heating," Ultrasound in medicine & biology, vol. 27, 2001, pp. 673-82.

[47] A.E. Worthington and M.D. Sherar, "Changes in ultrasound properties of porcine kidney tissue during heating," Ultrasound in medicine & biology, vol. 27, 2001, pp. 673-682.

[48] A.E. Worthington, J. Trachtenberg, and M.D. Sherar, "Ultrasound properties of human prostate tissue during heating," Ultrasound in medicine & biology, vol. 28, 2002, pp. 1311-1318.

[49] S. Ginter, M. Liebler, E. Steiger, T. Dreyer, and R.E. Riedlinger, "Full-wave modeling of therapeutic ultrasound: Nonlinear ultrasound propagation in ideal fluids," The Journal of the Acoustical Society of America, vol. 111, 2002, pp. 2049-2059.

[50] J. Tavakkoli, D. Cathignol, R. Souchon, and O.A. Sapozhnikov, "Modeling of pulsed finite-amplitude focused sound beams in time domain," The Journal of the Acoustical Society of America, vol. 104, 1998, pp. 2061-2072.

[51] J.N. Tjotta, S. Tjotta, and E.H. Vefring, "Effects of focusing on the nonlinear interaction between two collinear finite amplitude sound beams," The Journal of the Acoustical Society of America, vol. 89, 1991, pp. 1017-1027.

[52] R.O. Cleveland, M.F. Hamilton, and D.T. Blackstock, "Time-domain modeling of finite-amplitude sound in relaxing fluids," The Journal of the Acoustical Society of America, vol. 98, 1995, pp. 2865-2865.

[53] R.O. Cleveland, J.P. Chambers, H.E. Bass, R. Raspet, D.T. Blackstock, and M.F. Hamilton, "Comparison of computer codes for the propagation of sonic boom waveforms through isothermal atmospheres," The Journal of the Acoustical Society of America, vol. 100, 1996, pp. 3017-3027.

[54] S.A. Johnson, J.W. Wiskin, D.T. Borup, D.A. Christensen, and F. Stenger, "Apparatus and method for imaging with wavefields using inverse scattering techniques."

[55] P.L. Stoffa, J.T. Fokkema, R.M. Freire, and W.P. Kessinger, "Split-step Fourier migration," Geophysics, vol. 55, 1990, pp. 410-421.

[56] L. Huang and M.C. Fehler, "Accuracy analysis of the split-step Fourier propagator: Implications for seismic modeling and migration," Bulletin of the Seismological Society of America, vol. 88, 1998, pp. 18-29.

[57] F. Shen and A. Wang, "Fast-Fourier-transform based numerical integration method for the Rayleigh-Sommerfeld diffraction formula," Applied Optics, vol. 45, pp. 1102-1110.

[58] X. Zeng and R. McGough, "Optimal simulations of ultrasonic fields produced by large thermal therapy arrays using the angular spectrum approach," The Journal of the Acoustical Society of America, vol. 125, 2009, pp. 2967-2977.

[59] P. Wu and T. Stepinski, “Extension of the angular spectrum approach to curved radiators,” The Journal of the Acoustical Society of America, vol. 105, 1999, pp. 2618-2627.

[60] U. Vyas and D. Christensen, “Ultrasound beam propagation using the hybrid angular spectrum method,” Proceedings of the 30th Annual International Conference of the IEEE Engineering in Medicine and Biology Society, 2008, pp. 2526-2529.

[61] D. Christensen, Ultrasonic Bioinstrumentation, John Wiley & Sons, 1988.

[62] D.P. Orofino and P.C. Pedersen, “Efficient angular spectrum decomposition of acoustic sources. I. Theory,” IEEE Transactions on Ultrasonics, Ferroelectrics and Frequency Control, vol. 40, 1993, pp. 238-249.

[63] D.P. Orofino and P.C. Pedersen, “Efficient angular spectrum decomposition of acoustic sources. II. Results,” Ultrasonics, Ferroelectrics and Frequency Control, IEEE Transactions on, vol. 40, 1993, pp. 250-257.

[64] F.A. Jolesz, “MRI-guided focused ultrasound surgery,” Annual review of medicine, vol. 60, 2009, pp. 417-430.

[65] D.R. Daum and K. Hynynen, “A 256-element ultrasonic phased array system for the treatment of large volumes of deep seated tissue,” Ultrasonics, Ferroelectrics and Frequency Control, IEEE Transactions on, vol. 46, 1999, pp. 1254-1268.

[66] R.B. Roemer, W. Swindell, S.T. Clegg, and R. Kress, “Simulation of focused, scanned ultrasonic heating of deep-seated tumors: The effect of blood perfusion,” IEEE Transactions on Sonics and Ultrasonics., vol. 31, 1984, pp. 457-466.

[67] K.B. Ocheltree and L.A. Frizzel, “Sound field calculation for rectangular sources,” IEEE Transactions on Ultrasonics, Ferroelectrics, and Frequency Control, vol. 36, 1989, pp. 242-248.

[68] A.V. Oppenheim, A.S. Willsky, and W.S. Hamid, Signals and Systems, Prentice Hall, 1996.

[69] J. Tervo and J. Turunen, “Angular spectrum representation of partially coherent electromagnetic fields,” Optics Communications, vol. 209, 2002, pp. 7-16.

[70] W. Ping and T. Stepinski, “Spatial impulse response method for predicting pulse-echo fields from a linear array with cylindrically concave surface,” Ultrasonics, Ferroelectrics and Frequency Control, IEEE Transactions on, vol. 46, 1999, pp. 1283-1297.

[71] P.R. Stepanishen, “Transient radiation from pistons in an infinite planar baffle,” The Journal of the Acoustical Society of America, vol. 49, 1971, p. 1629.

[72] J.A. Jensen, “Field: A program for simulating ultrasound systems,” Citeseer, 1996, pp. 351–353.

[73] R.J. McGough, “Rapid calculations of time-harmonic nearfield pressures produced by rectangular pistons,” The Journal of the Acoustical Society of America, vol. 115, 2004, p. 1934.

[74] D. Guyomar and J. Powers, “Transient fields radiated by curved surfaces---Application to focusing,” The Journal of the Acoustical Society of America, vol. 76, 1984, pp. 1564-1572.

[75] M. Abramowitz and I. Stegun, Handbook of Mathematical Functions, New York: Dover Publications, 1970.

[76] X. Wu and M. Sherar, “Theoretical evaluation of moderately focused spherical transducers and multi-focus acoustic lens/transducer systems for ultrasound thermal therapy,” Phys Med Biol, vol. 47, 2002, pp. 1603-21.

[77] D.R. Daum and K. Hynynen, “Thermal dose optimization via temporal switching in ultrasound surgery,” IEEE Transactions on Ultrasonics Ferroelectrics and Frequency Control, vol. 45, 1998, pp. 208-215.

[78] X. Fan and K. Hynynen, “Ultrasound surgery using multiple sonications--treatment time considerations,” Ultrasound in Med. & Biol, vol. 22, 1996, pp. 471-482.

[79] A.C. Clay, S. Wooh, L. Azar, and J. Wang, “Experimental study of phased array beam steering characteristics,” Journal of Nondestructive Evaluation, vol. 18, 1999, pp. 59-71.

[80] B.D. de Senneville, C. Mougenot, and C.T. Moonen, “Real-time adaptive methods for treatment of mobile organs by MRI-controlled high-intensity focused ultrasound,” Magnetic Resonance in Medicine, vol. 57, 2007, pp. 319-330.

[81] K. Hynynen, G.T. Clement, N. McDannold, N. Vykhodtseva, R. King, P.J. White, S. Vitek, and F.A. Jolesz, “500-element ultrasound phased array system for noninvasive focal surgery of the brain: a preliminary rabbit study with ex vivo human skulls,” Magnetic Resonance in Medicine, vol. 52, 2004, pp. 100-107.

[82] K.R. Gorny, N.J. Hangiandreou, G.K. Hesley, B.S. Gostout, K.P. McGee, and J.P. Felmlee, “MR guided focused ultrasound: technical acceptance measures for a clinical system,” Phys Med Biol, vol. 51, 2006, pp. 3155-73.

[83] K. Hynynen, “MRI-guided focused ultrasound treatments,” Ultrasonics, vol. 50, 2010, pp. 221-229.

[84] M.O. Kohler, C. Mougenot, B. Quesson, J. Enholm, B. Le Bail, C. Laurent, C.T. Moonen, and G.J. Ehnholm, “Volumetric HIFU ablation under 3D guidance of rapid MRI thermometry,” Med Phys, vol. 36, 2009, pp. 3521-35.

[85] H. Wan, J. Aarsvold, M. O'Donnell, and C.A. Cain, "Ultrasound surgery: Comparison of strategies using phased array systems," IEEE Trans. on Ultrason, vol. 43, 1996, pp. 1085-1097.

[86] H. Pennes, "Analysis of tissue and arterial blood temperatures in the resting human forearm.," Appl. Physiol., vol. 1, 1948, pp. 93-122.

[87] J. De Poorter, C. De Wagter, Y. De Deene, and C. Thomsen, "The proton resonance frequency shift method compared with molecular diffusion for quantitative measurement of two-dimensional time-dependent temperature distribution in a phantom," J. Magn. Reson., Series B, vol. 103, 1994, pp. 234-241.

[88] V. Rieke, K.K. Vigen, F.G. Sommer, B.L. Daniel, J. Pauly, and K. Butts, "Referenceless PRF shift thermometry," Magn Reson Med, vol. 51, 2004, pp. 1223-31.

[89] N. Todd, U. Vyas, J. de Bever, A. Payne, and D.L. Parker, "The effects of spatial sampling choices on MR temperature measurements," Magnetic Resonance in Medicine, Sep. 2010.

[90] F. Wu, Z.B. Wang, H. Zhu, W.Z. Chen, J.Z. Zou, J. Bai, K.Q. Li, C.B. Jin, F.L. Xie, and H.B. Su, "Extracorporeal high intensity focused ultrasound treatment for patients with breast cancer," Breast Cancer Res Treat, vol. 92, 2005, pp. 51-60.

[91] R. Salomir, J. Palussiere, F.C. Vimeux, J.A. de Zwart, B. Quesson, M. Gauchet, P. Lelong, J. Pergrale, N. Grenier, and C.T. Moonen, "Local hyperthermia with MR-guided focused ultrasound: spiral trajectory of the focal point optimized for temperature uniformity in the target region," J Magn Reson Imaging, vol. 12, 2000, pp. 571-83.

[92] E.L. Madsen, G.R. Frank, and F. Dong, "Liquid or Solid Ultrasonically Tissue-Mimicking Materials with Very Low Scatter," Ultrasound in Medicine & Biology, vol. 24, 1998, pp. 535-542.

[93] E.G. Moros, R.B. Roemer, and K. Hynynen, "Pre-focal plane high-temperature regions induced by scanning focused ultrasound beams," Int J Hyperthermia, vol. 6, 1990, pp. 351-66.

[96] M.E. Lyons and K.J. Parker, "Absorption and attenuation in soft tissues. II. Experimental results," Ultrasonics, Ferroelectrics and Frequency Control, IEEE Transactions on, vol. 35, 1988, pp. 511-521.

[95] R.B. Roemer, A.M. Fletcher, and T.C. Cetas, "Obtaining local SAR and blood perfusion data from temperature measurements: steady state and transient techniques compared," International journal of radiation oncology, biology, physics, vol. 11, 1985, pp. 1539-50.

[96] G. Frahling and C. Sohler, “A fast k-means implementation using coresets,” Proceedings of the twenty-second annual symposium on Computational geometry - SCG '06, Sedona, Arizona, USA: 2006, p. 135.

[97] V. Rieke and K.B. Pauly, “MR thermometry,” Journal of magnetic resonance imaging : JMRI, vol. 27, Feb. 2008, pp. 376-390.

[98] H.F. Bowman, “Heat transfer mechanisms and thermal dosimetry,” National Cancer Institute Monograph, vol. 61, Jun. 1982, pp. 437-445.

[99] D.T. Borup, S.A. Johnson, W.W. Kim, and M.J. Berggren, “Nonperturbative diffraction tomography via Gauss-Newton iteration applied to the scattering integral equation,” Ultrasonic Imaging, vol. 14, 1992, pp. 69-85.

[100] S.A. Sapareto and W.C. Dewey, “Thermal dose determination in cancer therapy,” Int J Radiation Oncology Biol Phys, vol. 10, 1984, pp. 787-800.